DEVELOPMENT OF HIGH-β, WEAKLY MAGNETIZED PLASMA COUETTE FLOW DRIVE IN PURSUIT OF ELECTROMAGNETIC INSTABILITIES IN THE HALL REGIME

by

Ken Flanagan

A dissertation submitted in partial fulfillment of
the requirements for the degree of

Doctor of Philosophy

(Physics)

at the

UNIVERSITY OF WISCONSIN–MADISON

2020

Date of final oral examination: August 3, 2020

The dissertation is approved by the following members of the Final Oral Committee:

Cary Forest, Professor, Physics

Jan Egedal, Professor, Physics

Ellen Zweibel, Professor, Astronomy and Physics

Carl Sovinec, Professor, Engineering Physics

to Emily, Binx and Pim

Of Bronze – and Blaze –
The North – tonight –
So adequate – it forms –
So preconcerted with itself –
So distant – to alarms –
An Unconcern so sovreign
To Universe, or me–
With taints of Majesty –
Till I take vaster attitudes –
And strut opon my stem –
Disdaining Men, and Oxygen,
For Arrogance of them –

My Splendors are Menagerie –
But their Competeless Show
Will entertain the Centuries
When I, am long ago,
An Island in dishonored Grass –
Whom none but Daisies – know.

— Emily Dickinson

Abstract

A new flow drive has been implemented at the Wisconsin Plasma Physics Laboratory (WiPPL) on both the Big Red Ball (BRB) and the Plasma Couette Experiment (PCX). In volumetric flow drive (VFD), a strong radial current (50-300 A) is driven across a weak applied magnetic field (0.5-10 G) throughout the plasma volume. The resulting electromagnetic body force is centrally peaked due to the natural profile of radial current in a cylindrical geometry. This drive offers an alternative to edge-driven plasma flows which struggle to efficiently couple momentum to the bulk plasma due to neutral collisions and low viscosities required for studying instabilities.

The VFD experiments on BRB reveal strong magnetic field amplification (factor of $20+$) near the rotation axis accompanied by a hollow density profile. These unanticipated equilibrium features are also observed in NIMROD simulations when the Hall term is included. A simple model describes how the Hall term acts to deflect radial injected current into the toroidal direction. In cases where the radial current is outward, the toroidal current will induce a magnetic field that reinforces the initial applied field. Conversely, an inward radial current will act to remove the magnetic field from the volume.

Using a single central cathode, VFD experiments on PCX explore the inward radial current configuration. Weak solid-body flow (peak flow < 200 m/s) is observed in this system by the high precision Fabry-Pérot spectrometer. The magnetic field is entirely removed at injected currents of 80-100 A. At higher applied field strengths, strong fluctuations between the ion and electron cyclotron frequencies are observed on all diagnostics, including the axial magnetic field measurements. These fluctuations are observed to be a flute-like mode rotating about the central axis. A high-β electromagnetic extension of the gradient drift instability is derived and well-matched to the onset of the observed fluctuations.

ACKNOWLEDGMENTS

No one can finish a PhD on their own. I am happily not an exception to this rule. Throughout my eight years at UW, I have been incredibly lucky to be surrounded by a group of mentors, colleagues, and friends that have supported and encouraged me to reach this conclusion. It has been an arduous and difficult process at times, but I can't imagine my life without the experiences and connections I have made here. I hope that I can give at least a fraction back of what I have received in support and friendship.

I will start by thanking my advisor Cary Forest, without whom I could never have reached this point. Your boundless energy and enthusiasm for an honestly staggering number of projects and ideas has kept me busy and moving. You have shown incredible patience during slow periods and fueled our group with intense focus when experiments are running smoothly. It has been an expansive experience to work for you.

I have also been fortunate to benefit from the knowledge and experience of other mentors. I'd like to thank in particular Jan Egedal, Ellen Zweibel, and Carl Sovinec, my committee members who all have advised and contributed significantly to my work and development as a scientist. I'd also like to thank my undergraduate advisor, Mike (Doc) Brown, for his continued friendship and support–it has always been a highlight of the yearly APS meeting to catch up with you. Also, I would like to thank Nicolas Plihon, who welcomed me to his lab in Lyon to test out the Fabry-Pérot spectrometer–your willingness and enthusiasm for collaboration has been such a boon for this work.

It's inconceivable how I could have accomplished anything in the lab without the help of Mike Clark and John Wallace, two incredible engineers and even better people. You both have saved the lab and my sanity so many times I couldn't even count. Mike, I don't know how to thank you enough for the literal *days* you have spent sealing water leaks on PCX. John, I can't express how thankful I am for all the times that I showed up at your door with a pesky problem that you proceeded to solve.

I am lucky to have met and worked alongside many experts who have graciously given me time and attention, especially for the seemingly impossible tasks I would bring. Alex Squitieri, I am incredibly thankful that you could help me out of so many computing problems–I'd still be stuck with a stubborn glitch right now if it weren't for you. Bill Zimmerman, your mechanical tips and tricks (and some good jokes) were always welcome. I'd like to also thank the team in the Physics Instrument Shop, especially Doug Dummer and Bill Foster. You not only solved nearly impossible machining problems with the PCX upgrade, but you also welcomed me into that process so that I could learn and benefit from your experience. You have been the best Chamberlin basement neighbors!

When it comes to overall morale and camaraderie, I can't believe how wonderful it has been to share this time with such an amazing set of peers. I'd like to thank Cami, Matt, and Dave for the patience you showed me as I was learning the ropes and for all of your work that I built off of. Cooper, you made a mark on our group in the most positive way imaginable and I am so happy that you were around in those earlier years. Yufan, Megan and Austin, you were amazing undergrad workers and such a joy to work with. Victor, you have been such a great friend and unofficial Lyon tour guide–*merci du fond du couer, mon ami*. Jason, I can't thank you enough for arguing with me for hours about silly things in the office–I think we probably figured out some of the tougher physics and engineering problems we faced that way. I'm so happy that we found a way to finish together with our data from PCX. Joe, you always seemed to know how to do things before I did and I am so happy that you passed everything on–*salmon hands*. Ethan, working with you was a joy because you are a truly kind-hearted person and because you seem to do more than your share in any group project. Doug, I will never understand how you can do so many things at once so well, but I am eternally grateful for you and your boundless energy for both work and friendship. I am also thankful for the shorter time I have spent with some other wonderful students in our lab. Emma and Rachel, you have been amazingly supportive and kind and I hope that I found ways to give back to you as well.

Despite the reputation of physicists as isolated and aloof, I have friends outside of the lab group that I would like to acknowledge for their love and support. At times, I needed distractions, a sympathetic ear, or trusted advice and you have given me that and so much more. Thank you Todd, Danny, Ariel, Lauren, Ed and Laura. You guys all started out as "physics" friends, but have become my dearest and closest allies both inside and out of Chamberlin. Chloë and Brendan, I want to thank you specifically for giving Emily and me a place to run away to when needed.

To my family, thank you for supporting and listening and cheering and commiserating for all these years. I am so happy and proud to be the first Doctor of Philosophy in our family of M.D.s!

Finally, and most importantly, thank you Emily. I still can't believe that you agreed to come to Wisconsin with me, but I am so grateful that you did. Through the years, you have generously given me more love and support than I could ever imagine, never allowing me to feel alone. You are my partner and best friend in all things. As much as you like to say you don't understand what I do, I see this degree as ours. We did it! I love you!

Commonly used acronyms and symbols

β	Beta - the ratio between the thermal energy of a plasma and the magnetic field energy. High β means that plasma pressure dominates the magnetic field dynamics
BRB	Big Red Ball - a spherical multi-cusp confinement experiment at the Wisconsin Plasma Physics Laboratory (WiPPL)
LaB_6	Lanthanum Hexaboride - an elemental compound used in emissive cathode construction on the BRB and PCX.
MHD	Magnetohydrodyamics - a fluid model description of plasma dynamics.
MRI	Magnetorotational instability - a flow-driven magnetohydrodynamic (MHD) instability thought to be responsible for turbulence in accretion disks.
MPDX	Madison Plasma Dynamo Experiment - the original name of the BRB.
NIMROD	Non-Ideal MHD with Rotation, Open Discussion. A 3D magnetohydrodynamics code.
PCX	Plasma Couette Experiment - a cylindrical multi-cusp confinement experiment at the Wisconsin Plasmas Physics Laboratory (WiPPL).
SmCo	Samarium Cobalt - the elemental compound that comprises the permanent magnets on the BRB and PCX
TCF	Taylor-Couette Flow - the flow driven between rotating concentric cylinders.
WiPPL	Wisconsin Plasma Physics Laboratory (WiPPL)
VFD	Volumetric flow drive - a flow drive technique where an electromagnetic body force is applied to the entire plasma profile.

TABLE OF CONTENTS

Page

Page

Page

LIST OF FIGURES

Figure Page

Figure | Page

Figure Page

Figure Page

Chapter 1

Introduction

Plasma is the most common phase of matter in the universe, yet perhaps the least understood. More energetic than solids, liquids and gases commonly found on Earth, plasmas are the main component of many astrophysical bodies, such as stars, accretion disks and nebulae. Fundamentally, plasmas are clusters of ionized particles, negatively charged electrons and positively charged ions, that exhibit collective behavior. Being made of charged particles, plasmas interact via electromagnetic forces which are described by Maxwell's equations. The distinction of collective behavior, however, requires a much more detailed understanding. In the simplest models, plasmas are treated as a fluid with additional responses to electric and magnetic fields. This approach, called magnetohydrodynamics (MHD), describes certain plasma regimes and phenomena extremely well, particularly when the charged particles are well-coupled to a magnetic field that permeates the plasma. Under certain conditions, however, the various species of charged particles behave very differently and are no longer well-described as a single fluid. In the Hall regime, ions become decoupled from the magnetic field and electrons govern electromagnetic dynamics. Hall effects are present in many astrophysical plasmas, particularly where magnetic fields are weak or in the process of being generated and amplified. Therefore, it is key to the study of plasmas to explore the Hall regime and probe its implications in these astrophysical systems.

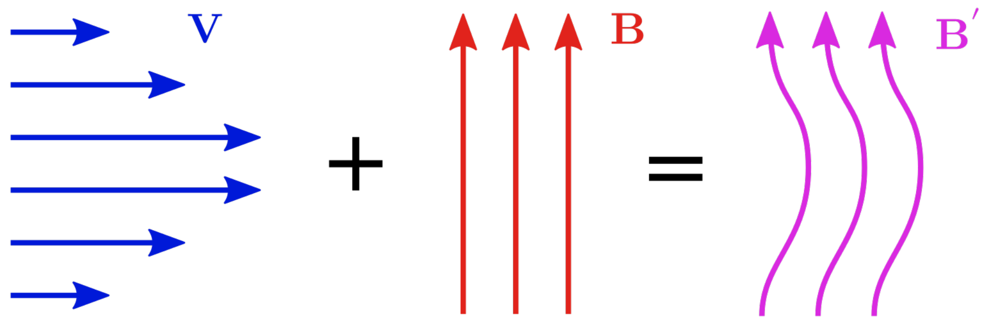

Figure 1.1: A diagram showing the need for flow shear to distort magnetic field lines. A sheared flow (blue) can distort a uniform magnetic field (red), stretching the field lines (magenta).

The work presented in this dissertation focuses on the implications of the Hall regime on plasma experiments geared toward studying flow-driven astrophysical instabilities. In this introduction, I will describe a few magnetohydrodynamic instabilities and outline previous experimental work focused on recreating them in the laboratory. Then I will describe the new and growing field of plasma hydrodynamics, where plasma flows dominate magnetic fields and resistive effects. I will also briefly describe the two-fluid Hall regime where plasma hydrodynamics experiments operate. Finally, I will outline the key results of my work and the structure of this dissertation.

1.1 Flow-driven magnetohydrodynamic instabilities

As an extension of traditional fluid dynamics, magnetohydrodynamics is necessarily concerned with the interaction between conducting fluids and magnetic fields. For a perfectly conducting (or 'ideal') plasma, the magnetic field is often said to be 'frozen-in'. More specifically, Alfvén's theorem states that the magnetic flux through a volume of plasma, $\Psi \equiv \int \mathbf{B} \cdot d\mathbf{s}$, is unchanging, necessarily moving with the plasma [1]. By applying Faraday's law of induction, another description of the frozen-in flux condition is that the electric field in the moving frame of the plasma, $\mathbf{E}'$, is zero.

$$\mathbf{E}' = \mathbf{E} + \mathbf{V} \times \mathbf{B} = 0 \tag{1.1}$$

where the $\mathbf{E}$ and $\mathbf{B}$ are the electric and magnetic fields in the fixed frame, and V is the velocity of the plasma. Equation 1.1 links the fluid dynamics of an ideal plasma to the electromagnetic fields described by Maxwell's equations.

In addition to advecting frozen-in magnetic fields, plasma flow can stretch magnetic field lines, transferring energy to and from the magnetic field. A simple uniform flow is incapable of stretching magnetic field lines; rather, shear is required. With flow shear, a magnetic field will be displaced differentially along its length, leading to stretching (see Fig. 1.1). In flow-driven instabilities, this flow shear is a source of free energy that drives the instability and creates back reactions via magnetic field stretching.

Both coupling to the magnetic field and flow shear are necessary for flow-driven MHD instabilities. A key feature of these instabilities is a dynamic feedback mechanism between the flow and a magnetic field. I will briefly describe two such flow-driven instabilities below: the magnetorotational instability and the dynamo.

1.1.1 Magnetorotational instability

First derived by Velikhov and Chandrasekhar in the context of general magneto-fluid instabilities [2, 3], the MRI is a strong, fast-growing instability that acts to transport angular momentum in sheared flows. The basic requirement of the MRI in the absence of dissipation mechanisms is to have a flowing conducting medium with a centrally peaked flow profile threaded by a weak magnetic field.

The basic mechanism is illustrated in the toy model presented in Fig 1.2. Consider two fluid parcels that are rotating about a central axis in a fluid with a flow profile that decreases with radius. A weak magnetic field threads this fluid, such that a field line tethers the two fluid parcels. If a small displacement causes one of the parcels to move slightly inwards (smaller radius), this will create tension in the field line. This magnetic

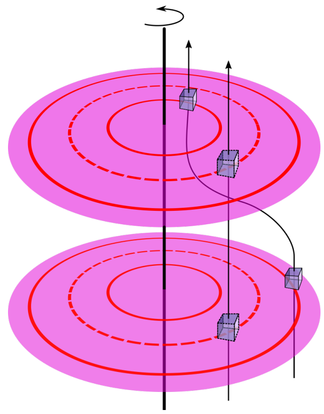

Figure 1.2: A simple diagram showing the toy model description of the MRI. A weak magnetic field threads a flowing, conducting fluid. A field line connects two fluid parcels and transfers angular momentum via its tension from the inner parcel to the outer. This causes the inner parcel to drop to a lower orbit and the outer one to increase its orbital radius. The diverging orbits of the fluid parcels increases the tension on the field line and leads to a growing instability.

tension acts to transport angular momentum from the now-inner fluid parcel to the other parcel. Since the flow is decreasing with radius, the inner fluid parcel will lose angular momentum to the other parcel and fall to a lower orbit. The other parcel will gain angular momentum and move to a larger orbit, increasing the magnetic tension. The increased magnetic tension will transfer more angular momentum, starting a runaway process that transfers the angular momentum outwards more and more.

In a seminal paper, Balbus and Hawley re-derived and applied this instability to the problem of angular momentum transfer in accretion disks [4]. If standard frictional transport of angular momentum was the dominant mechanism responsible for accretion, matter would take nearly the age of the universe to fall onto central objects in many observed accretion systems. Shakura and Sunyaev proposed the so-called α-disk model to explain the necessary enhanced angular momentum transport, wherein they show that a turbulent disk can accrete at reasonable rates given enough turbulence [5]. The turbulence they

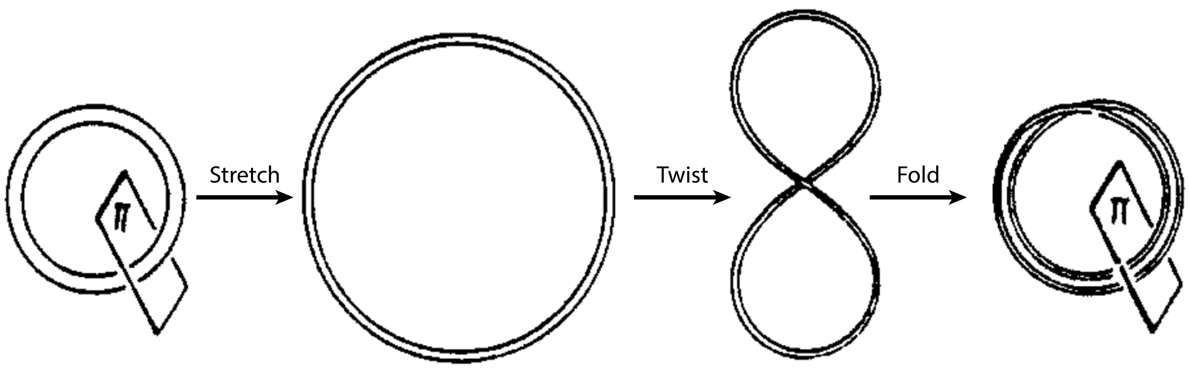

Figure 1.3: A cartoon of the stretch, twist and fold mechanism responsible for dynamo action. A flux loop is stretched to a larger area, twisted and then folded back into the original loop shape. The total magnetic flux through the surface π will be doubled at the end of this process. Figure credit: [6]

applied was ad hoc without an instability to fuel it, until Balbus and Hawley showed that a weak magnetic field could destabilize the disk via the MRI.

1.1.2 Dynamo instability

Similar to the time-scale problem that the MRI solves for accretion, the dynamo provides a mechanism by which astrophysical magnetic fields can be created and maintained against resistive diffusion. Many observed magnetic fields in the universe have resistive lifetimes much shorter than they have existed. The magnetic field of Earth has a resistive decay time of roughly 10,000 years, which is much shorter than the Earth's age of approximately 4 billion years. Dynamic behavior is also a key feature of observed fields. Fossil records indicate reversals of Earth's magnetic field polarity, and the 22 year cycle of sunspot migration has motivated many models of the sun's magnetic field.

In its simplest form, a dynamo is a system that transfers mechanical flow energy to magnetic fields. This requires a stretching of magnetic field lines via sheared flow, followed by a folding of the stretched field lines back to their original orientation which amplifies the initial field [6]. Figure 1.3 shows an example of this process. Dynamo growth rates are tied to the period of this stretch, twist and fold mechanism, which is typically characterized by the eddy turnover time. Dynamos are classified as 'slow' or 'fast' based on this time scale. 'Slow' dynamos are laminar with macroscopic stretch-twist-fold mechanisms, while 'fast' dynamos are turbulent and typically amplify the field on smaller scales.

Larmor was the first to propose that inductive processes could be responsible for the sun's magnetic field [7]. Shortly thereafter, Cowling made the observation that dynamos are not as simple as they seem, proving that an axisymmetric flow could not sustain an axisymmetric magnetic field [8]. Developments in modeling and simulations eventually allowed Bullard and Gellman to describe three-dimensional processes for dynamo action [9] and later for Dudley and James to show dynamo action in simulations of certain laminar flow configurations [10]. Parker described a mechanism by which individual turbulent eddies could collectively lead to a global dynamo and this was later formalized into mean-field theory [11]. Following these foundational contributions, a massive amount of research has gone into the dynamo problem which is well beyond the scope of this overview.

1.2 Experimental search for instabilities

Naturally, many experiments have been conducted to reproduce and study both the MRI and the dynamo in a controlled laboratory setting. Capturing these dynamical instabilities in such a setting would grant invaluable insight into many astrophysical phenomena as well as serve to validate and inform increasingly complex and expensive simulations.

In real astrophysical systems, neither the MRI nor the dynamo exist in such an ideal form as presented above. Rather, a zoo of additional physics can come into play depending on conditions of the system ranging from the fraction of ionized particles to neutral gas to the details of collisions between particles. A major contribution to this added complexity is dissipative forces that come in the form of resistivity and viscosity. Viscosity is ubiquitous in all fluids, and leads to diffusion of momentum due to internal friction. For a very viscous fluid, such as honey, it is difficult to create the strong flow shear that is necessary for instabilities. Electrical resistivity, however, is a unique feature of conducting fluids. If the conducting fluid cannot respond quickly enough to changing magnetic fields, it will not be able to support and advect them. Linking back to Eq. 1.1, resistivity allows for an electric field in the fluid frame, which will cause magnetic field lines to slip through the plasma fluid. This is described by Ohm's law which relates the electric field (in the fixed frame) to the plasma current.

$$\mathbf{E} + \mathbf{V} \times \mathbf{B} = \eta \mathbf{J} \tag{1.2}$$

where η is the resistivity of the plasma. Unlike many other conducting media, the resistivity of a plasma decreases when the temperature is increased due to the nature of Coulomb collision cross-sections. So hotter plasmas, like those created in fusion experiments, will have a vanishing resistivity and are often treated as ideal[1]. For some astrophysical plasmas or liquid metals, however, the resistivity can be higher and reduce the advection of magnetic fields by plasma flows

The degree to which viscosity and resistivity play a role in a fluid flow can be parameterized by the Reynolds number and the magnetic Reynolds number, respectively.

$$R_e = \frac{VL}{\nu} \qquad\qquad R_m = \frac{VL}{\eta} \tag{1.3}$$

where V is the characteristic flow speed, L is the characteristic size of the system in question, ν is the kinematic viscosity of the fluid and η is the resistivity of the fluid. The fluid Reynolds number compares the relative magnitude of the inertial force of the fluid to viscous dissipation, while the magnetic Reynolds number compares magnetic field advection to resistive decay. In order to avoid quenching of a flow-driven instability by either viscosity or resistivity, both of these values must be large. For magnetohydrodynamic instabilities to dominate fluid turbulence, it is particularly important for R_m to be large, while R_e is small enough to avoid fluid turbulence that would muddle any experimental observations.

[1] For example, the resistivity of a $T_e \sim 2.5$ keV plasma is roughly the same as copper

1.2.1 Liquid metal experiments

Due to the relatively easy confinement and mechanical stirring of liquid metals, they have been the dominant medium in both MRI and dynamo experiments. Several dynamos have been produced in heavily constrained liquid metal experiments, notably the Riga [12] and the Karlsruhe [13] experiments which both reported self-excited magnetic fields. However, the constrained flows used for these experiments do not match real astrophysical systems where large scale turbulence plays an important role.

For MRI experiments, there is not an analogous constrained flow method for exciting instability. As a result, the MRI has not been observed in a laboratory setting in its distinguishable form. Several experiments, like the Princeton MRI Experiment or the Maryland Spherical Couette Experiment, have produced liquid metal flows that are destabilized by a magnetic field [14]. However, the observed instabilities are not the MRI, but rather caused by fluid turbulence in boundary layers [15]. Other liquid metal experiments have studied the so-called helical MRI wave that is related to the standard MRI, but operates with a different magnetic field configuration [16, 17].

For both dynamo and MRI liquid metal experiments, a significant hurdle is the fixed resistivity and viscosity of their media. Liquid sodium, for example, has a fixed resistivity of 0.2 m^2/s (roughly the same as iron) and very low viscosity of 3×10^{-7} m^2/s (similar to water). As a result, driving flows to reach large magnetic Reynolds numbers leads to fluid turbulence, which masks or quenches the simple linear growth of possible magnetohydrodynamic instabilities that are desired. In dynamo experiments, this leads to the need for constrained flows to produce self-excited magnetic fields, while in MRI experiments, fluid instabilities appear before any magnetohydrodynamic instability.

The turbulence encountered in liquid metal flows is of great interest. Experiments at the Madison Dynamo Experiment showed that the turbulence in an unconstrained liquid sodium flow could reduce the decay rate of applied magnetic fields [18]. This result is of particular interest to the study of turbulent dynamos, despite the initial goal of producing a laminar dynamo. Observations made at the Von-Kármán Sodium experiment in France have shown that by seeding an unconstrained liquid sodium flow with iron impellers, dynamo action can be driven [19]. This particular dynamo also exhibits dynamic behavior in its saturated state in an interesting analog to real astrophysical systems. Interestingly, applying the iron impeller constraint to the Madison Dynamo Experiment did not also lead to dynamo action, indicating that more work must be done to fully understand the Von-Kármán Sodium experiment results [20].

1.2.2 Flowing plasma experiments

In order to both mitigate the fluid turbulence found in liquid metal experiments and to include more non-ideal effects, MRI and dynamo experiments in plasmas have been created. In a plasma, both the resistivity and the viscosity of the fluid are not fixed, but rather depend on the rate of collisions between particles. Resistivity is set by the collision rate between electrons and ions, which depends heavily on the electron temperature. For viscosity, the ion-ion collision rate is the key component and depends on the density and ion temperature. Using the well-accepted Braginskii transport equations for plasmas in the limit of small magnetic fields [21], the Reynolds and magnetic Reynolds numbers can be recast in terms of plasma parameters as,

$$R_e = 7.8\frac{n_{18}\sqrt{\mu}Z^4\,V_{\mathrm{km/s}}L_{\mathrm{m}}}{T_i^{5/2}} \tag{1.4}$$

$$R_m = 1.6\frac{T_e^{3/2}\,V_{\mathrm{km/s}}L_{\mathrm{m}}}{Z} \tag{1.5}$$

where n_{18} is the plasma density in units of 10^{18} m^{-3}, μ is the ion mass in amu, Z is the ion charge state, T_i is the ion temperature in eV and T_e is the electron temperature in eV. By modifying the density and temperature of a plasma, these parameters can be tuned to meet the criteria of high R_m and moderate R_e required for flow-driven magnetohydrodynamic instabilities.

In addition to overcoming dissipative forces, a plasma experiment with the goal of exciting flow-driven magnetohydrodynamic instabilities must be able to contain and heat plasmas without large magnetic fields that would otherwise dominate the kinetic energy contained in the flows and, most importantly, drive large flows. At the Wisconsin Plasma Physics Laboratory (WiPPL), both of these requirements are met by devices that use strong magnetic fields at the edge of the plasma for confinement [22]. The strong fields at the edge are arranged in a high-order multipole configuration such that the strength falls off rapidly in the interior of the plasma, leaving most of the volume unmagnetized.

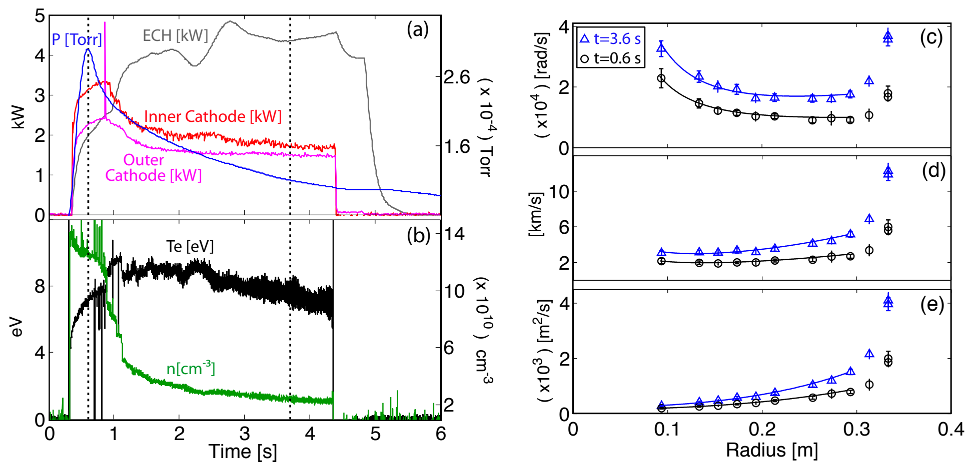

Figure 1.4: Differential flow discharge on PCX. In (a) the plasma creation and heating inputs are shown, including the inner and outer cathodes which stir from the boundaries. (b) shows the electron temperature and density over the course of the shot. (c-e) show the profile as a function of radius for the angular velocity, azimuthal velocity ($V = \Omega R$) and angular momentum. This flow profile meets the ideal MRI criteria in the region from 0.1-0.3 m with $R_m \simeq 65$ and $R_e \simeq 26$.

Plasma stirring has been pioneered at WiPPL by using electrodes arranged in the confining edge field to draw current across the field lines, leading to a torque on the plasma. This torque is then viscously coupled inward to the magnetic field-free bulk of the plasma, leading to fast, unmagnetized plasma flows. This stirring technique was developed on the Plasma Couette Experiment (PCX), with the goal of driving plasma flows with centrally peaked profiles, which would be unstable to the ideal MRI criteria [23, 24]. Figure 1.4 shows a flowing plasma discharge that meets the ideal-MRI criteria of a centrally peaked angular velocity profile. Chapter 3 will outline the additional requirements for observation of the MRI in PCX that have yet to be met in the experiment.

1.3 The two-fluid Hall regime

Just as dissipation complicates the ideal MHD model as shown above, the essential two-fluid nature of plasmas can have dramatic effects on the excitement of instabilities as well as general plasma equilibria. Much of the work presented in this dissertation is concerned with the effects of Hall physics on the flowing equilibria used in the search for flow-driven instabilities. Considering the ion and electron fluids separately, their momentum balance equations are,

$$m_i n_i \frac{d\mathbf{V}_i}{dt} = Zen_i(\mathbf{E} + \mathbf{V}_i \times \mathbf{B}) - \nabla p_i - n_i m_i \nu_{ie}(\mathbf{V}_i - \mathbf{V}_e) - \nabla \cdot \overleftrightarrow{\mathbf{\Pi}}_i \tag{1.6}$$

$$m_e n_e \frac{d\mathbf{V}_e}{dt} = -en_e(\mathbf{E} + \mathbf{V}_e \times \mathbf{B}) - \nabla p_e - n_e m_e \nu_{ei}(\mathbf{V}_e - \mathbf{V}_e) - \nabla \cdot \overleftrightarrow{\mathbf{\Pi}}_e \tag{1.7}$$

The left hand side of both equations is the convective derivative, which includes the explicit change in time of the flow $(\partial/\partial t)$ as well as the deformation due to movement $(\mathbf{V} \cdot \nabla\mathbf{V})$. On the right hand side, the first term is the Lorentz force, the second is the pressure gradient, the third is the resistive drag caused by collisions with the other fluid, and the last is the viscous stress. For this discussion and the rest of this work unless explicitly stated, the ions will be treated as singly ionized such that $Z = 1$. For singly charged ions, quasi-neutrality states that the densities of the species are the same for scales greater than the Debye length (which is quite small for plasmas of interest in this work). The collision frequencies between the species, ν_{ei} and ν_{ie}, are simply related to the Spitzer resistivity: $m_e\nu_{ei} = m_i\nu_{ie} = ne^2\mu_0\eta$. The viscous stresses can be cast in a simplified, isotropic form as,

$$\overleftrightarrow{\mathbf{\Pi}}_s = -n_s m_s \nu^s \nabla\mathbf{V}_s \tag{1.8}$$

where the kinematic viscosities, ν^s, are dependent on the temperature of the species and the density [2].

Equations 1.6 & 1.7 along with Maxwell's equations fully describe a conducting two-fluid system. However, a very useful simplification can be made by using the large separation in the masses of the fluids. Defining the following constitutive relations highlights this approximation.

$$\begin{aligned}
\rho &\equiv n(m_i + m_e) \simeq nm_i \\
\mathbf{V} &\equiv \frac{m_i \mathbf{V}_i + m_e \mathbf{V}_e}{m_i + m_e} \simeq \mathbf{V}_i \\
\mathbf{J} &\equiv ne(Z\mathbf{V}_i - \mathbf{V}_e)
\end{aligned} \tag{1.9}$$

The mass density, ρ, and flow, $\mathbf{V}$, are simplified in the limit that $m_e/m_i \ll 1$. This ratio is very small for any ion-electron plasmas, typically on the order of 10^{-4}. The current density, $\mathbf{J}$, is introduced as a new variable to replace the two fluid velocities and links the fluid dynamics to the magnetic field through Ampére's law, $\mu_0 \mathbf{J} = \nabla \times \mathbf{B}$. In the small mass ratio limit, Eqns. 1.6 & 1.7 can be combined to produce a single-fluid momentum balance equation,

$$\frac{d\mathbf{V}}{dt} = \frac{1}{\rho}\left(\mathbf{J} \times \mathbf{B} - \nabla p\right) + \nu \nabla^2 \mathbf{V} \tag{1.10}$$

where $p \equiv p_i + p_e$ is the total pressure and ν is the viscosity as defined by the ion-ion collisions (the same ν used for calculating R_e) and is taken to be uniform. The relationship between the electric field and the current density must also be defined for a complete model. In the same small mass ratio limit, Eqns. 1.6 & 1.7 can be manipulated to create the generalized Ohm's law,

$$\mathbf{E} + \mathbf{V} \times \mathbf{B} = \eta \mathbf{J} + \frac{1}{ne}\left(\mathbf{J} \times \mathbf{B} - \nabla p_e\right) \tag{1.11}$$

Like the resistive Ohm's law in Eq. 1.2, the result of the two-fluid treatment leads to an additional term in the expression that describes the frozen-in flux condition. Replacing $\mathbf{J}$

[2] The electron viscosity can be neglected for the parameters and dynamics of interest here, so the viscosity set by ion-ion collisions will simply be denoted as ν.

in this expression with its definition in Eq. 1.9, it becomes clear that the magnetic field is now coupled to the electron fluid.

$$\mathbf{E} + \mathbf{V}_e \times \mathbf{B} = \eta \mathbf{J} - \frac{1}{ne}\nabla p_e \tag{1.12}$$

Resistivity will still cause field line slipping, but this is typically small for sufficiently hot plasmas. Additionally, the electron pressure gradient does not contribute to the induction because the loop integral of a gradient must be zero. Using Faraday's law of induction, the evolution of the magnetic field in a two-fluid system can be written as,

$$\frac{\partial \mathbf{B}}{\partial t} = \nabla \times (\mathbf{V}_e \times \mathbf{B}) - \eta \nabla^2 \mathbf{B} \tag{1.13}$$

It is clear in this expression that the ion flow in a two-fluid system does not advect the magnetic field, rather the highly mobile electrons are responsible. This so-called Hall effect has major implications for any system with plasma currents and can lead to large qualitative differences in equilibria and instability growth as understood from a simple single-fluid MHD approach.

The onset of the Hall effect is set only by the density and scale of interest in the system being studied. The generalized Ohm's law (Eq. 4.12) can be non-dimensionalized to highlight this onset by dividing by a fiducial magnetic field, B_0, and velocity, V_0.

$$\mathbf{E} + \mathbf{V} \times \mathbf{B} = \frac{\mathbf{J}}{R_m} + \frac{\delta_i}{L}(\mathbf{J} \times \mathbf{B} - \beta_e \nabla p_e) \tag{1.14}$$

where

$$\begin{aligned} \delta_i &\equiv \frac{c}{\omega_{pi}} = \sqrt{\frac{m_i}{\mu_0 n e^2}} \\ \beta_e &\equiv \frac{2\mu_0 n T_e}{B_0^2} \end{aligned} \tag{1.15}$$

are the ion inertial length and electron β set by reference values of n and T_e. It is clear that a higher R_m is desired to remove the field-line slipping effects caused by resistivity. The second term on the right hand side, the Hall term, scales with the ratio of the ion inertial length to the system scale, L. When this ratio approaches or exceeds unity, the Hall term will become important, leading to a flux freezing (or, with resistivity, coupling) condition for the electron fluid. Additionally, the importance of the electron pressure gradient scales with plasma β (specifically electron β), which is simply the ratio of the plasma pressure to the magnetic pressure. For high-β plasmas, this term must also be included in Ohm's law as it will contribute to the Hall electric field (non inductively). For typical laboratory astrophysics plasmas, δ_i is on order 1 m, which is roughly equivalent to a normal system size. Clearly, in such devices the Hall term is important and must not be neglected.

1.4 Dissertation outline

Arguably the main motivation for flowing plasma experiments at WiPPL has been to reach flows and plasma parameters that are predicted to excite either the dynamo or the MRI. My work started with this same goal in mind, specifically searching for the MRI. Over the course of the refinement of both plasma conditions and flow drives, the goal of this work has evolved to a more general understanding of the flowing plasmas we create in the lab, rather than a direct search for instabilities. As I've shown above, unmagnetized laboratory astrophysical plasmas nearly always operate in the high-β Hall regime, where large electron currents can drive strong advection of weak magnetic fields. Necessarily this changes the conditions for exciting instabilities, but also it opens up a rich field of more basic study of this two-fluid effect. As such, I see the dissertation presented here as both an accounting of the specifics of exciting the MRI in WiPPL plasmas and as a first step into the interesting field of flowing high-β Hall plasmas.

The layout of this work loosely follows the progression from pure MRI study to more general Hall physics. In the following chapter, Ch. 2, I will describe two WiPPL experimental devices: the Big Red Ball (BRB) and the Plasma Couette Experiment (PCX). This chapter will detail the plasma confinement, heating and stirring schemes used, as well as the vast diagnostic suite available at WiPPL. In Chapter 3, I will focus specifically on the stability of Taylor-Couette flows driven in PCX with respect to the MRI. I will outline the effects of neutral particles and Hall physics to the MRI and show via a global stability analysis the various barriers to observation of the MRI with such a drive. Following this, Chapter 4 will present an alternative Couette flow drive mechanism that addresses many of the issues raised by the previous chapter's analysis. I will present experimental results of this new flow mechanism, volumetric flow drive, on the BRB along with matching NIMROD simulations. In both the experiment and simulations, an effect associated with strong Hall currents drastically alters the equilibrium. I will outline the basic mechanism of this effect and provide an alternative model for volumetric flow drive that takes this into account. Following these BRB experiments, Chapter 5 presents an alternative configuration of volumetric flow drive realized on PCX. Unexpectedly, the weak flowing equilibrium found on PCX is destabilized by Hall currents and extended density gradients. While this instability is not strictly flow driven, it highlights the impact of high-β Hall effects on astrophysical plasma experiments. In Chapter 6, I will end this dissertation with an overview of the major results of my work as well as suggestions for future focus, particularly for the relatively unexplored high-β Hall regime.

Chapter 2

Experimental Systems and Techniques

The experimental observations used for this thesis were preformed on two devices at the Wisconsin Plasma Physics Laboratory (WiPPL): the Plasma Couette Experiment (PCX) and the Big Red Ball (BRB). Both devices operate on the same principle of plasma confinement and heating. Rings of high-strength permanent magnets are arranged at the boundaries of the plasma in an alternating multi-cusp configuration. The high-order field from these magnets quickly falls off in radius, leaving the majority of plasma bulk free from confining magnetic fields. This allows both devices to create $\beta = \infty$ plasmas, with densities in the $10^{17} - 10^{18}$ m^{-3} range and electron temperatures from $5 - 15$ eV. Plasma creation and heating is handled by hot emissive cathodes that are biased to several hundred volts. These cathodes can also be used to electromagnetically stir the plasma, providing an excellent test-bed for plasma hydrodynamic experiments.

This chapter will serve to describe both the PCX and BRB devices as well as the extensive suite of diagnostics available to both. First I will describe PCX, which is where a majority of my work was focused. A massive upgrade to the confinement system allows PCX to create plasmas with densities and temperatures similar to the much larger BRB. I will then give a brief overview of the BRB, highlighting the several differences to PCX. Following these device descriptions, I will discuss plasma heating and stirring via hot emissive cathodes. The rest of the chapter will focus on the diagnostics used at WiPPL including the mm-wave interferometer and high-resolution Fabry-Pérot spectrometer.

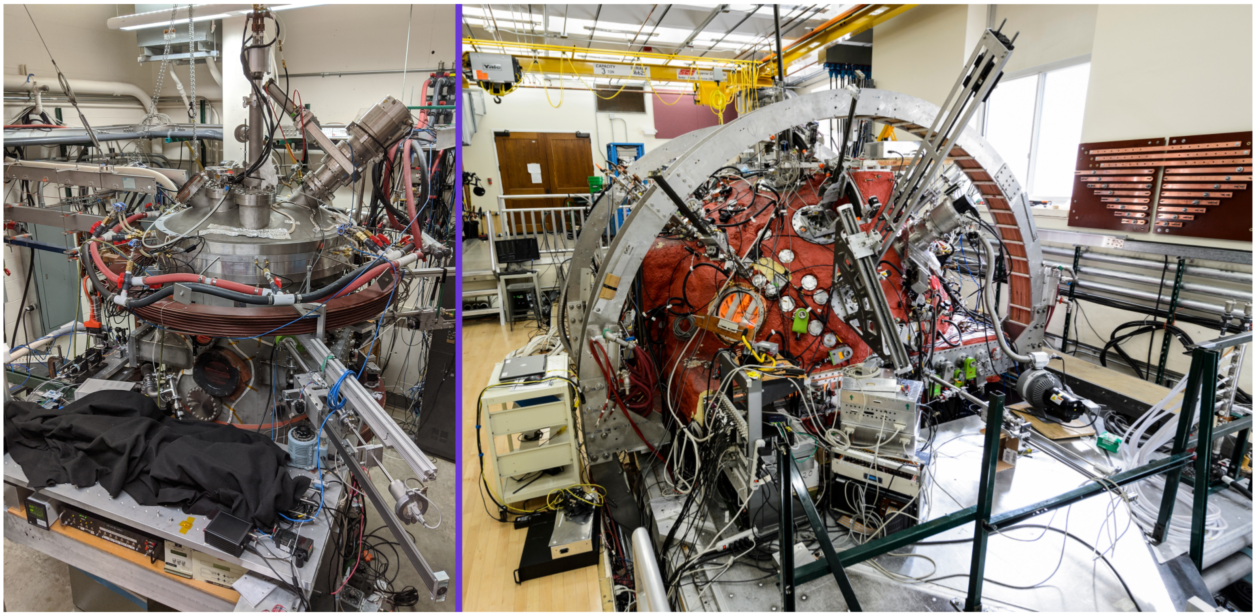

Figure 2.1: Left: image of the PCX device; the Fabry-Pérot spectrometer is covered in blackout material on the scanning optics table and a single LaB6 cathode is inserted on axis from the top of the vessel. Right: image of the BRB device from the North pole of the device; a scanning probe stage is mounted near the pole

2.1 Plasma Couette Experiment

The Plasma Couette Experiment (PCX) (Fig. 2.1 Left) is a plasma hydrodynamics experiment in a cylindrical geometry [25, 24, 26]. The roughly 1 m tall, 1 m diameter vacuum vessel is lined with an array of nearly 1900 high strength permanent magnets that confine a cylindrical plasma roughly 60 cm tall and 90 cm in diameter. In addition to the confining field (which drops to zero in the center of the chamber) a Helmholtz coil set can provide vertical fields up to ~ 30 G.

Unlike larger WiPPL experiments, PCX is operated by one or two people at a time, often jumping between several different campaigns. This degree of flexibility makes PCX a perfect test-bed for proof-of-concept of new diagnostics or plasma drive techniques. In addition to its main focus of plasma Couette flow, PCX has run ion-implantation experiments, served as a system for collaborators to benchmark a laser-induced florescence (LIF) system and provided flowing test plasmas used to develop the extremely precise Fabry-Pérot ion diagnostic.

2.1.1 Vacuum vessel

The PCX vacuum vessel is mostly cylindrical with a curved top and bottom. The walls are 1/4″ thick stainless steel and the outer radius is 50.8 cm. The bottom is welded to the cylindrical section and contains 3 ports: one central port that is used for on-axis electrodes as well as water-cooling feedthroughs for the magnet array and two symmetric angled ports that are used for vacuum pumping.

The central cylinder contains 30 ports of varying sizes spaced to fit in the gaps between magnet rings. Near the rear of the vessel, the electrode ports are split between two toroidal locations separated by 10°. By alternating anodes and cathodes between the magnet rings, the direction of edge-flow drive is the same in each gap between rings. The main probe locations are at 45° at the electrode mid-plane and at 135° between magnet rings 9 & 10 (roughly 18.5 cm above the mid-plane).

PCX is equipped with a scanning optics table mounted at the electrode mid-plane. Parallel box ports provide access for diagnostics that need to sample across the plasma, such as the Fabry-Pérot spectrometer. A large view port at the same height is set perpendicular to the box port view, ideal for LIF measurements that need to collect light perpendicular to the laser. This table can scan across nearly the entire plasma volume, allowing for multiple chord measurements that can be analyzed to produce radial profiles.

The top of PCX is removable to allow access to the center of the chamber. There are five ports on the top flange. One central port is used for electrodes that are too large to fit between magnet rings on the cylindrical section. Two symmetric angled ports, like on the bottom section, are used for a top-down window and for additional vacuum pumping. The remaining two ports are aligned with the axis of the main cylinder, allowing vertical probe access to different radii.

The vacuum pumping system on PCX is capable of holding the chamber at base pressures around 10^{-7} torr. Throughout the vessel, Viton o-rings are primarily used for creating a seal, but some copper gaskets have been installed for more permanent features. The vacuum is monitored by a residual gas analyzer (RGA) and a cold cathode gauge (CCG). The CCG is used to interlock the gate valves attached to pumps to ensure that any leaks do not lead to damage.

On the bottom of the vessel, two 1500 L/s cryogenic pumps are attached to the angled ports. These pumps are extremely robust and very capable of pumping air, water, and argon. However, they do not perform well for helium because they operate with liquid helium cooling and cannot reach cold enough temperatures to easily condense helium vapors. Due to this restriction, an additional 250 L/s turbo-molecular pump is mounted on one of the angled ports on the top of the vessel. The turbo-molecular pump is backed with a simple dry scroll pump resting under the vessel. The turbo-molecular pump must be mounted at top to ensure that any falling debris will not get caught in the rapidly rotating blades.

Routine maintenance of the vacuum consists of monitoring the base pressure to detect any small leaks, regenerating the cryogenic pumps approximately once a month and replacing the tip seals on the scroll pump after about three months of continual use.

2.1.2 Magnetic confinement system

The original magnetic confinement system on PCX consisted of relatively low-strength ceramic magnets that were epoxied to aluminum rings and wrapped with insulating teflon tape [27]. Following a massive upgrade, the multicusp confinement system on PCX is larger, more accessible and made up of stronger rare-earth magnets (more details on the upgrade process can be found in Appendix A). This upgrade took roughly a year to complete and has pushed PCX to the same parameter regimes as the BRB by leveraging the increased plasma volume and reduced cusp loss width from stronger magnets.

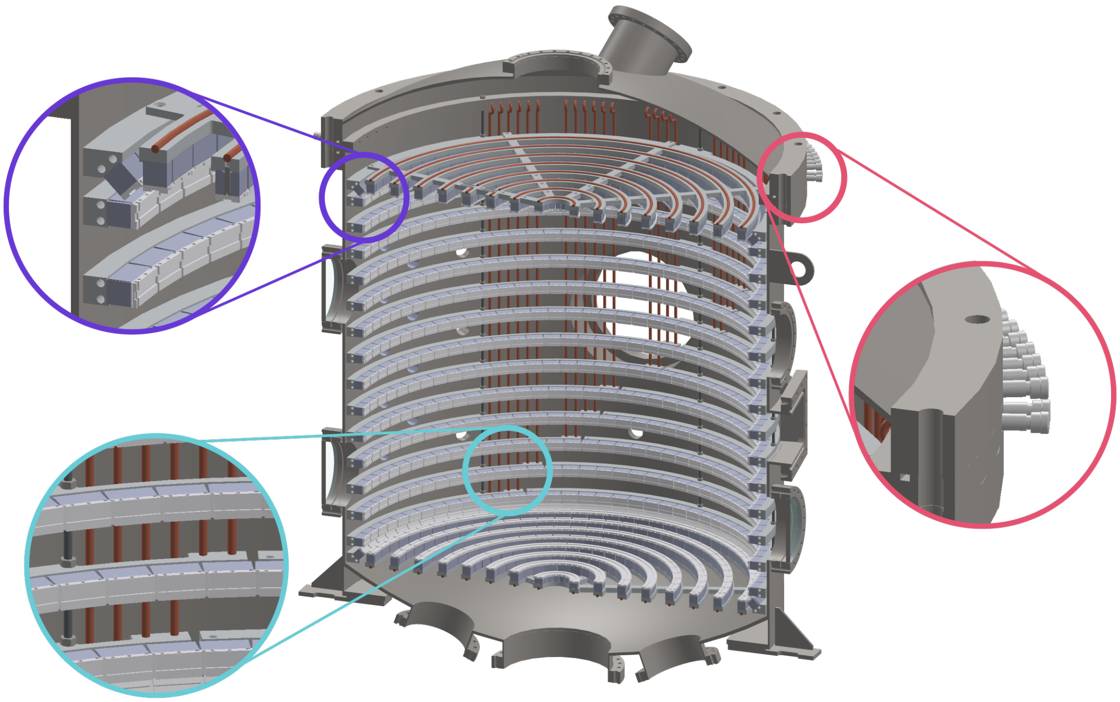

Figure 2.2: CAD image of the PCX magnetic confinement system inserted into the chamber. The purple inset highlights the angled magnet ring and internal cooling channels in the rings. The teal inset shows the water cooling pipe management as well as the alumina tiles. The pink inset is focused on the custom feedthroughs for the water cooling pipes.

Nearly 1900 samarium cobalt (SmCo) magnets line the inside of the PCX vessel. These magnets have a field strength of approximately 3 kG on their surface and an maximum operating temperature of nearly 300° C. Each magnet has a countersunk (#8-32 100° head) through hole for mounting. The magnets have a square 0.75″ cross-section and have 4 different footprints shown in Fig. 2.3. The magnets are covered with custom made alumina tile limiters that insulate the plasma from the grounded magnet assembly and vacuum chamber. The tiles are held in place by small steel dowel pins inserted in holes on the side that are attracted to the high-strength magnets.

Approximately 1000 of the magnets are bolted to 14 custom extruded aluminum rings that have internal water cooling channels. These rings are spaced approximately 1.5″

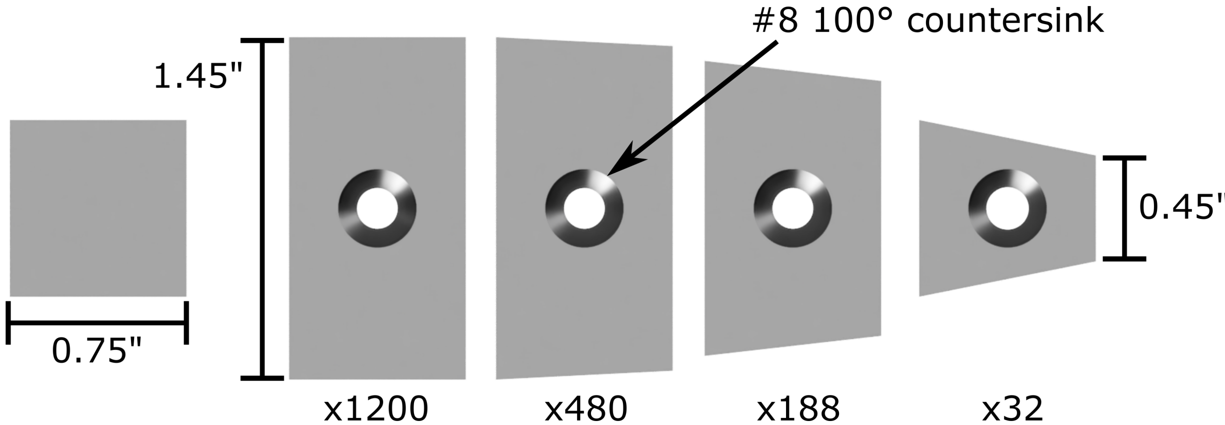

Figure 2.3: Dimensions and shapes of the SmCo magnets used on PCX; the rectangular magnets are used on the side and angled rings, while the keystone shapes are used on the bottom and top end assemblies.

apart, allowing access to the plasma volume via KF40 ports. The rings are supported by 5 threaded rods attached to a upper flange that fits between the cylindrical portion of the chamber and the removable top. Each of these rings has a send and return 1/4″ water cooling pipe that runs up to the support flange where a custom made feed-through is used to bring the pipe out of the vacuum. Rings that are higher up have cutouts to allow lower rings' water cooling tubes to run up without loosing plasma volume. As a result, the rings are carefully clocked with respect to these cutouts. More details of the ring design and construction can be found in Appendix A.

In addition to the 14 side rings, two sets of 350 magnets are mounted to 8 aluminum concentric rings that are attached to the bottom and top of the side ring assembly. These end-cap rings are water cooled as well with press-fit copper pipes. For the top cap, the copper pipes are brought out of vacuum with the same custom feed-throughs used for the side rings. The bottom cap sends its water cooling lines out through a set of feed-throughs mounted to the flange at the center bottom of the vessel.

The last two rings of the assembly are pitched at 45° are placed in the corners between the end-cap assemblies and the top and bottom side rings. These angled rings serve to

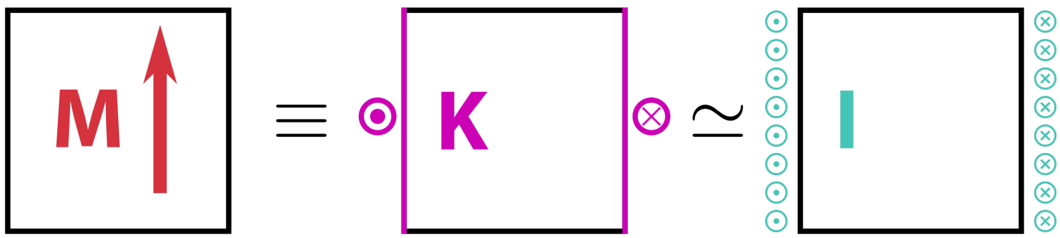

Figure 2.4: A cartoon showing the approximation of a uniform magnetization by loops of current placed on the surface. This approximation is used for calculating the field produced by the magnetic confinement system in both PCX and BRB.

improve the confinement in the tight corners of the cylindrical volume. They have the same water cooling design as the side rings and pass their cooling through the upper support flange.

The field from the permanent magnet assembly and the external Helmholtz coil set can be modeled using the analytical expression for a loop of current. In cylindrical coordinates, the poloidal field components of a loop of radius a carrying current I is [28]

$$B_r = \frac{\mu_0 I}{2\pi\alpha^2\beta}\frac{z}{r}\left[(\alpha^2 + r^2 + z^2)E(k^2) - \alpha^2 K(k^2)\right] \tag{2.1}$$

$$B_z = \frac{\mu_0 I}{2\pi\alpha^2\beta}\left[(\alpha^2 - r^2 - z^2)E(k^2) + \alpha^2 K(k^2)\right] \tag{2.2}$$

where $\alpha^2 \equiv a^2 + r^2 + z^2 - 2ar$, $\beta^2 \equiv a^2 + r^2 + z^2 + 2ar$, $k^2 \equiv 1 - \alpha^2/\beta^2$ and E and K are the elliptic integrals of the first and second kind, respectively. For a single magnet with uniform magnetization, the field is equivalent to that from a surface current along the faces perpendicular to the field. This surface current is approximated with excellent accuracy by placing an array of 8 loops along the magnet surface. The geometry of this is shown in Fig. 2.4. This allows an analytic representation of the field from the magnet assembly which can be easily plotted as shown in Fig. 2.5.

The magnet assembly does produce a weak ($\sim$ 3 G) residual dipole field due to the necessary odd symmetry of the magnet rings. During construction, the magnets were placed to ensure that this residual field was pointing downwards, in the same direction as the local earth field (~ 0.6 G). This way, a small positive Helmholtz field would ensure a magnetic field amplitude < 0.1 G throughout most of the volume. Canceling the central field does alter the cusp field geometry some, enforcing aligned fields and weakening opposite ones. This does not have a noticeable effect on confinement, but does require re-positioning of stirring cathodes located in the cusp for optimum edge flow.

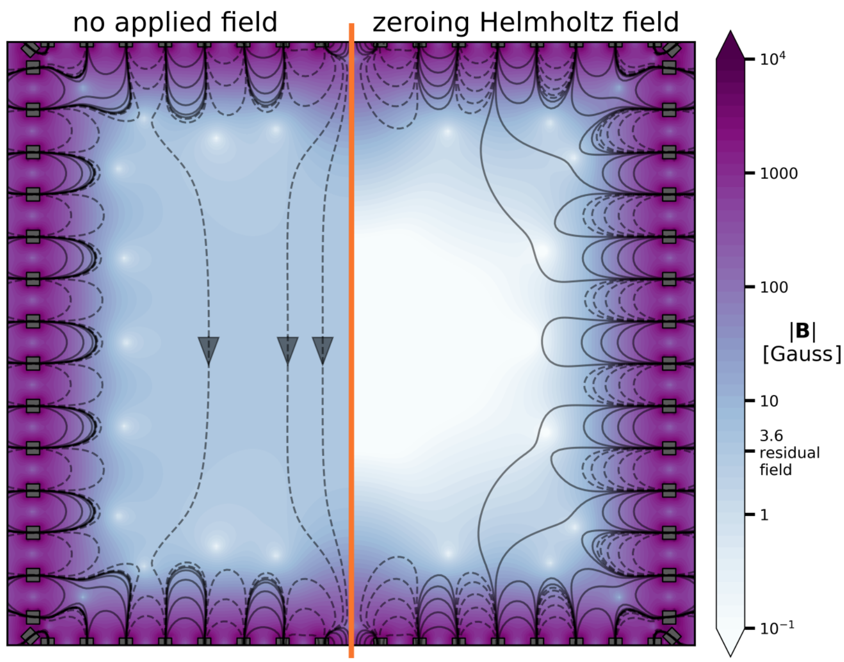

Figure 2.5: Calculated vacuum magnet field magnitude on PCX; on the left is a plot of the field with no Helmholtz current applied; on the right is a mirror across the axis of symmetry with a vertical Helmholtz field applied to cancel out earth field and the residual dipole from the magnet assembly. The contours are of Ψ and the same magnitude on both sides, showing the deformation of the cusp by applying an external field.

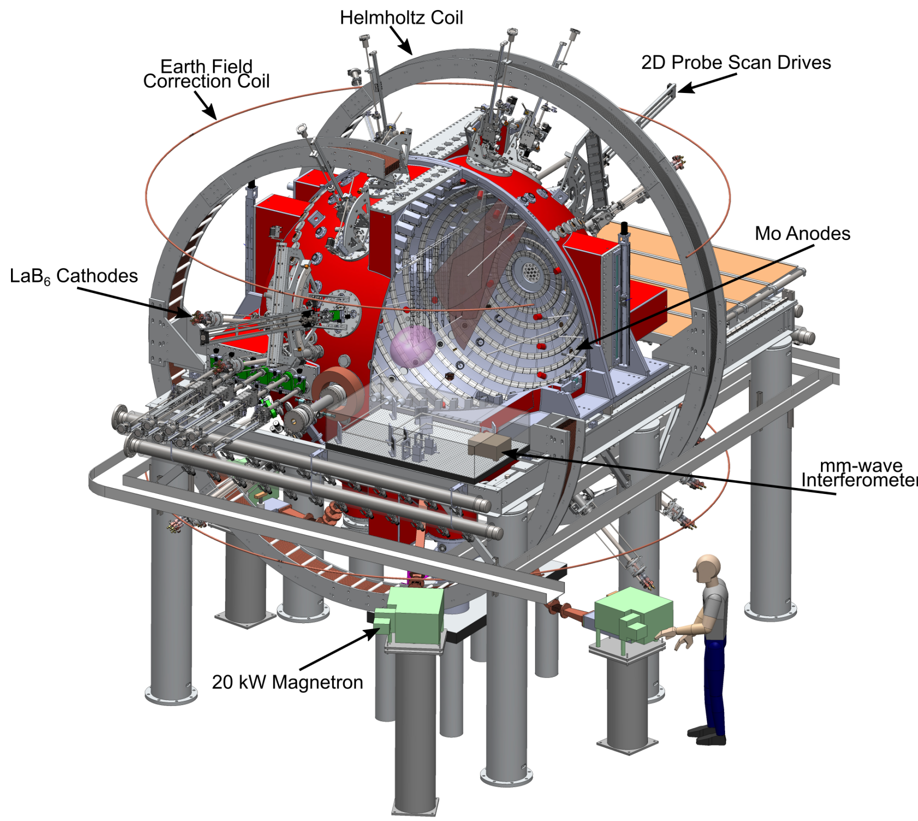

Figure 2.6: A CAD cutaway of the BRB vessel showing the location of various ports. The cut in this view is made at the equator of the vessel.

2.2 Big Red Ball

Originally, PCX served as a prototype experiment for proof-of-concept of the multi-cusp magnetic confinement and electromagnetic stirring technique for the Madison Plasma Dynamo Experiment (MPDX) [29]. After several years of dynamo-relevant flow experiments, MPDX was renamed the Big Red Ball (BRB) to reflect the much broader scope of this device. As its name suggests, the BRB device is a roughly 3 m diameter foam-insulated spherical chamber that is painted in red flame retardant paint (Fig. 2.1 Right). Like PCX, axisymmetric rings of permanent magnets line the wall of the chamber to provide confinement, while a water-cooled external Helmholtz coil set allows uniform fields up to 250 G to be applied to the otherwise unmagnetized plasma volume.

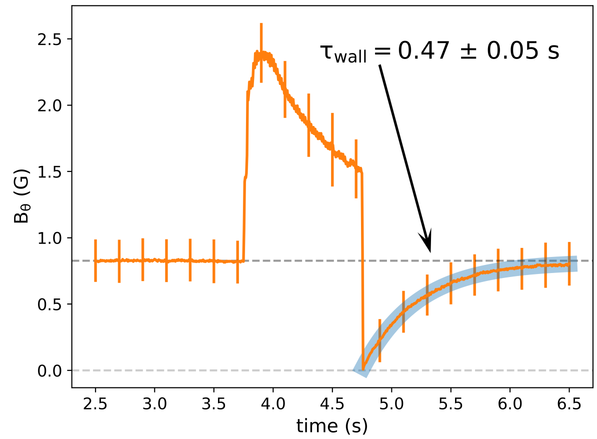

Figure 2.7: A measurement of the magnetic field made on the inside wall of the vessel during a discharge that produced a large magnetic field. When the plasma is extinguished at roughly $t = 4.75$ s, the created field slowly diffuses through the aluminum vessel wall. An exponential fit sets the BRB wall time at roughly 0.5 s.

The chamber is cast out of aluminum in two separate hemispheres with a wall thickness of ~ 3 cm. The magnetic wall time of this shell is roughly 0.5 s $($see Fig. 2.7$)$ for B_θ, but calculations of B_z predict a time on the order of 5 s due to the axial field in a spherical geometry. Over the outer surface, a system of stainless steel cooling pipes are cast into the wall to provide cooling of the entire chamber. The red insulation foam serves to improve the efficiency of this cooling, which has a capacity of about 1 MW.

The vessel is equipped with a large number of vacuum ports directly cast into the vessel $($see Fig. 2.6$)$. There are 184x 3″and 16x 14″ circular diagnostic ports as well as 12 rectangular box ports for optical diagnostic access and scanning. Ports are mostly aligned along lines of longitude, with few exceptions. Four 14″ ports are vertically aligned on extensions on the bottom of the device where two cryogenic pumps and two 1000 L/s turbo-molecular pumps keep the base pressure around 7×10^{-7} torr. Like PCX, the vacuum is diagnosed with a RGA and cold cathode gauges.

The SmCo magnets used on BRB are similar to those on PCX, with a $\gtrsim 3$ kG surface strength and 300° C maximum working temperature. They have a cross section of 1.5″x1″

and a footprint of 3″x1.5″ with a slight keystone shape to accommodate the spherical ring shape. Unlike PCX, the nearly 3000 BRB magnets are mounted directly onto the inside wall of the vessel in 36 separate rings. This represents a huge advantage because water cooling is maintained through the vessel wall without the need to install vacuum feedthroughs. The BRB magnets covered with 0.125 in thick alumina tile limiters placed over Kapton insulating film to ensure electrical isolation of the plasma from the chamber. [1] Additionally, the interior wall between magnet rings is sprayed with an alumina coating to further insulate the chamber from the plasma. A map of the magnetic field generated by the BRB magnet array is shown in Fig. 2.8.

[1]Ultimately, this Kapton insulation was difficult to install and found to be overkill. As a result, Kapton was not applied to the PCX magnet system when it was upgraded.

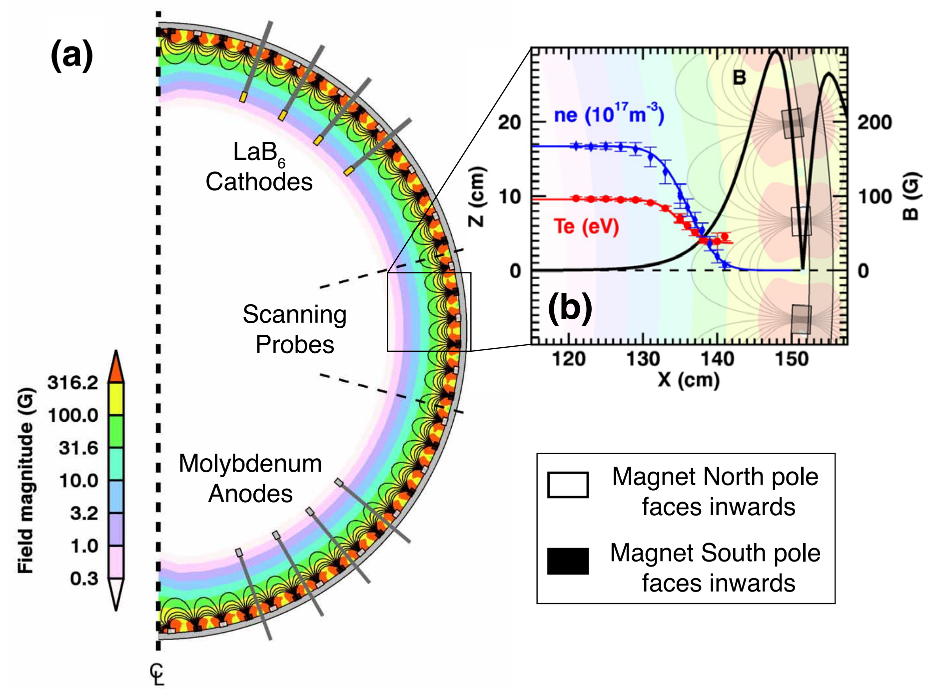

Figure 2.8: A plot of the calculated cusp magnetic field generated in BRB from the SmCo magnet array. Like PCX, the cusp field is highly localized to the edge, leaving almost no field in the central bulk of the device. The inset image shows the typical gradient scale for the plasma pressure in the cusp. Inside of roughly 130 cm, the plasma is extremely uniform. Image credit: [30]

2.3 Plasma creation and flow drive

The following section is focused on plasma creation, heating and stirring using hot emissive cathodes. For both PCX and BRB, the same electrodes and techniques are used unless noted.

2.3.1 Lanthanum hexaboride cathodes

A major technological achievement of the WiPPL group, led by Dave Weisberg [31], has been the development of reliable, high current density emissive cathodes. Due to its extremely low work function, lanthanum hexaboride (LaB_6) serves as an excellent electron

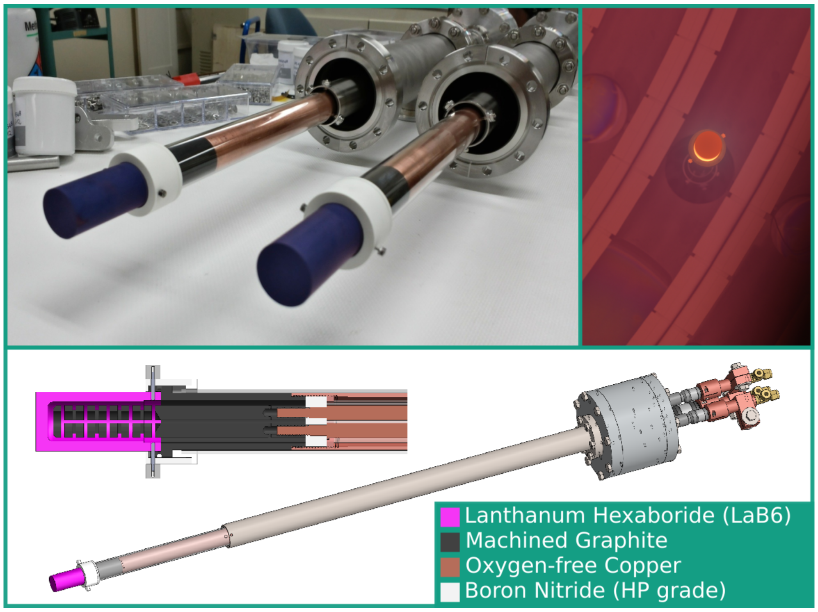

Figure 2.9: Images of the LaB6 cathodes used on PCX and BRB. Top Left: two cathodes outside the vessel before being inserted and heated. Top Right: Heated cathode seen across the BRB vessel. Bottom: CAD images of the cathode design with a cutaway close up of the tip.

emitter. Previous work with thoriated tungsten filaments has shown that the maximum current for these wires is around 5 A [27], while the LaB_6 can produce currents ≥ 100 A (which exceeds the capacity of the typically used power supplies). Unlike the tungsten wire, the LaB_6 is indirectly heated via radiation from a graphite filament. This design has the advantage of less 60 Hz leakage from the AC heating circuit and avoids the need to bias this heating circuit far below ground during a discharge. Of course, the advantages of LaB_6 come with some costs, notably the thermal management of these cathodes requires a larger diameter shaft to accommodate thick copper leads that are water cooled. Additionally, careful modeling was required to design a mechanical holder for the LaB_6 that was robust enough for movement during installation, but flexible when heated to nearly 1500° C. A schematic as well as real image of the LaB_6 cathodes used is shown in Fig. 2.9.

2.3.2 Typical discharge characteristics

A typical discharge on either device starts with the introduction of a very small amount of gas, most often argon or helium, into the vacuum. The gas is delivered either by a precise needle valve or a piezo-electric "puff" valve. Typically, argon can be introduced as a back fill with the needle valve, while helium requires puffing due to the difficulty of pumping it with the cryogenic pumps. Once the gas has been released into the vacuum, a bias of several hundred volts is applied between the LaB_6 cathode(s) and cold, molybdenum anodes. This bias accelerates primary electrons from the LaB_6 cathode into the gas, causing an ionization cascade which fuels the plasma. By controlling the initial neutral gas pressure and the electrical bias, different plasma densities can be achieved. Both PCX and BRB have ionization fractions roughly set by the confinement time of the systems, so a higher neutral fill typically leads to a higher density while maintaining roughly the same ionization fraction (given enough power is injected via the cathodes). This allows a high degree of flexibility through plasma density parameter space.

Figure 2.10 shows a typical LaB_6 argon discharge on PCX. Plasmas typically are programmed to last for 1-3 seconds in order to allow any flow to entirely spin up and to ensure that the cathode power supplies can regulate to their maximum current output. With the excellent heat management of both devices, these long discharges are thermally managed by relatively short repetition rates of 1-2 minutes. Common probe scans are of the order of 50 shots, allowing data sets to be generated in about one day of running. This degree of flexibility is essential to the WiPPL devices, because it allows for rapid exploration of many different experimental avenues.

2.3.3 Edge flow drive

A key feature of WiPPL experiments is the ability to drive fast, unmagnetized plasma flow. A combination of the strong edge-localized cusp field and injected currents from hot cathodes allows for electromagnetic stirring from the edge of the plasma. Figure 2.11 shows a diagram of this stirring technique. A strong bias voltage is applied between the

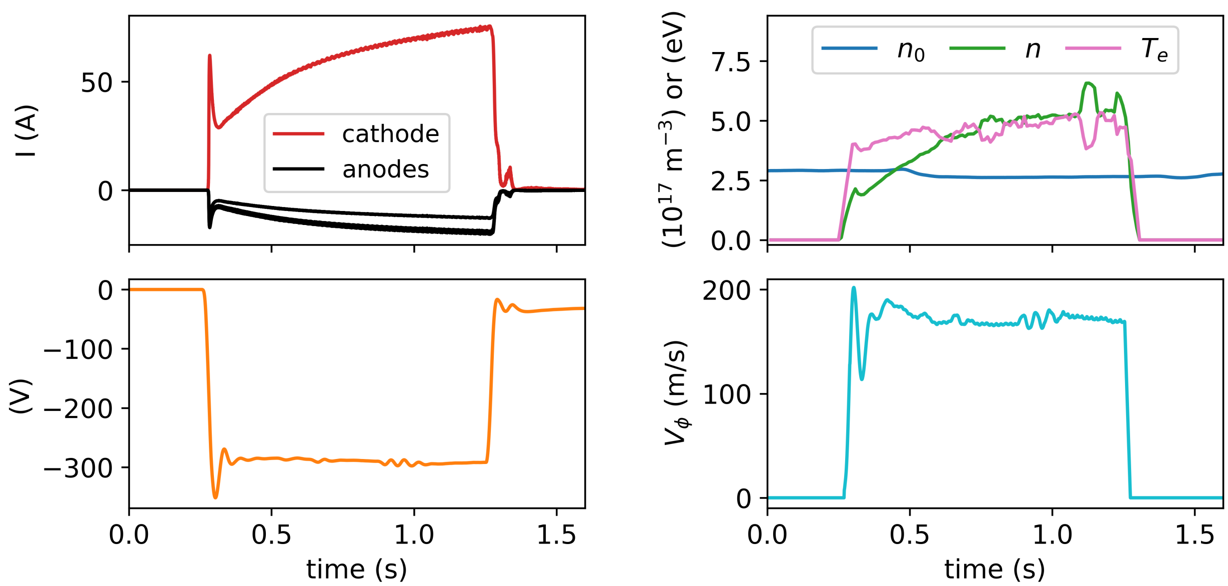

Figure 2.10: Time traces of standard measured values during a LaB_6 argon plasma in PCX. Top Left: the electrode currents. Bottom Left: the power supply bias voltage measured at the cathode with respect to the grounded chamber. Top Right: The neutral density, n_0, measured by the CCG along with the density, n, and electron temperature, t_e from a swept Langmuir probe. Bottom Right: the roughly calibrated ion flow speed from a Mach probe.

hot emissive cathodes (yellow) and the grounded cold anodes (gray). By positioning the cathodes at a larger radius, the current driven by this circuit is directed radially outward between every other set of rings. The strong cusp magnetic field alternates polarity between rings as well, so the cross product of the driven current and the magnetic field is in the same direction for each set of electrodes. The Lorentz force that arises from this cross-field current drives plasma flow at the edge, that then couples viscously inward and spins up the unmagnetized plasma bulk.

Many components of this drive mechanism must be tuned to maximize the flow, in particular the placement of the electrodes. When cathodes are retracted too far, the discharge current is heavily impeded by the magnetic field. Conversely, if the current is driven across

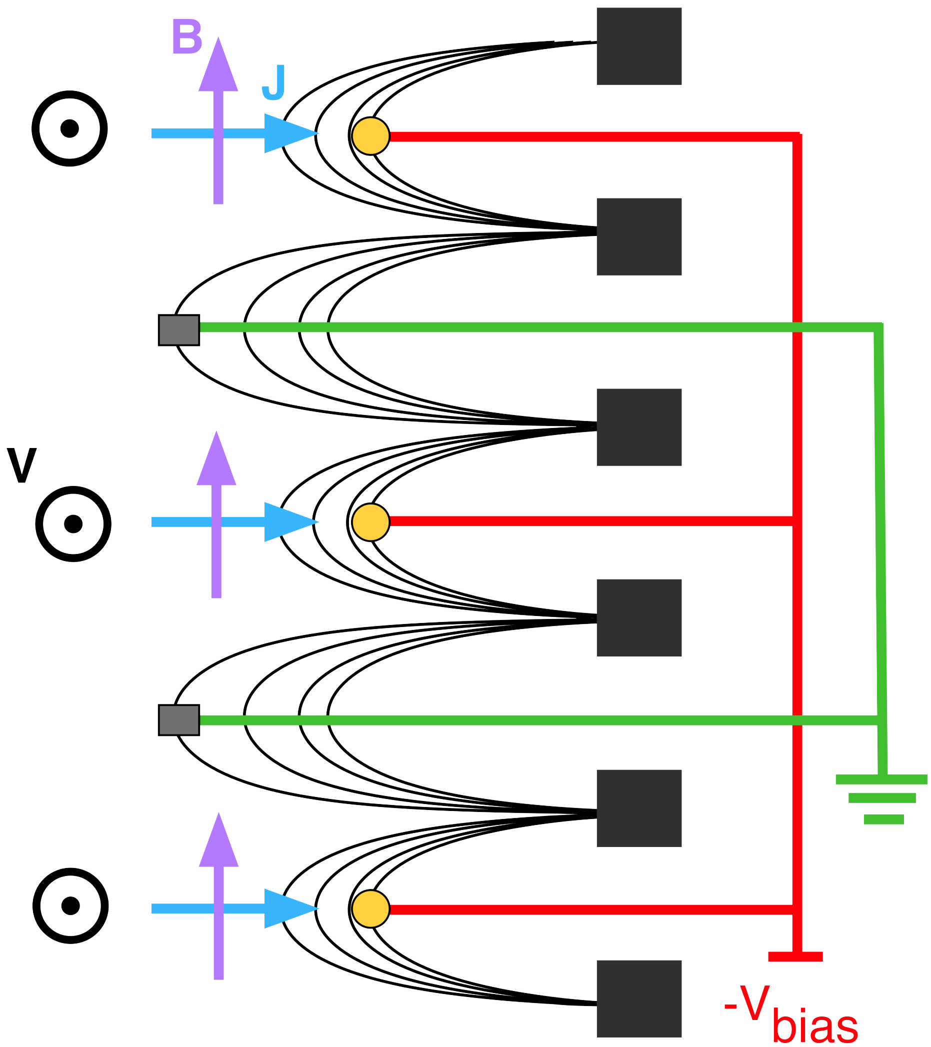

Figure 2.11: Simple diagram of the edge flow drive technique. Electrodes are placed in the strong, edge-localized magnetic field (purple) and drive cross-field currents (blue).

too weak of a field, the drive is inefficient and flow is weak. With the addition of externally applied Helmholtz fields, this balance can be further complicated. A more detailed description of how these edge-driven flows are modeled is given in Chapter 3.

2.4 Diagnostics

Both PCX and BRB provide excellent probe access for invasive measurements and are capable of supporting a wide array of advanced optical diagnostics. Most diagnostics are shared or copied between the two devices. This section will serve to outline how plasma and discharge parameters are measured and analyzed. Both devices are equipped with a standard set of vacuum and electrode measurements, a suite of electrostatic probes, magnetic probe arrays, and advanced optical diagnostics.

Data from the various diagnostics are recorded with one or more 96 channel, 250 kHz sampling rate D-tAcq digitizers. Signals from probes that are in contact with the plasma (i.e. electrostatic probes) are sent through custom built isolation amplifiers with 100 kHz bandwidth[2] before the D-tAcq to protect vital systems from any unwanted voltage spikes that can occur. Timing between various control and measurement systems is handled by a National Instruments field-programmable gate array (FPGA) module. Triggers can be set up with 1 ms resolution with a jitter less than 10 ns, ensuring that systems are synced very well throughout the lab.

2.4.1 Lab/maintenance diagnostics

On every discharge, a cold cathode gauge records the total neutral pressure at the wall. This gauge is placed on an angle, ensuring that there is no line-of-sight to the plasma, to protect sensitive components. A species dependent factor is applied to pressure to accurately reflect the neutral pressure of specific operating gases[3]. The neutral density is calculated from the pressure typically assuming that the neutral gas is at room temperature

[2]For electrical schematics see Cami Collins's thesis, Appendix B [27]

[3]Some common correction factors used are: 0.18 for helium, 0.46 for hydrogen, and 1.29 for argon. These factors are multiplied by the measured gauge value which is calibrated for nitrogen.

(300K or 0.025 eV). An array of LEM current and voltage transducers monitor the currents to and from electrodes and the voltages across power supplies. An additional current LEM is used to measure ground current leakages to ensure a low noise level throughout the lab.

Routine optical measurements are made in both devices as well. Several survey optical emission spectrometers (OES) from Ocean Optics are used to record the visible spectrum emitted from a plasma. This spectrum can be analyzed to determine the level of impurities present, particularly H-α from water, providing feedback while conditioning the experiment. Modeling can also be applied to determine a neutral density profile [32] and electron temperature [33, 34].

2.4.2 Electrostatic probes

An integral part of the diagnostic suite at WiPPL is a set of simple electrostatic probes. These probes feature combinations of Mach faces for measuring ion flow and either swept Langmuir tips or sets of tips for a triple probe configuration.

These probes all share the same basic design apart from the tip: a copper tube (1/4″ OD) runs down the length of the probe and is insulated from the plasma with a mirrored quartz tube. Wires connected to the various tips run up the tube into a custom stainless steal cup that holds the copper and quartz in place and acts as an o-ring surface for a sliding seal. The wires then attach to various electric vacuum feedthroughs at the back of the cup. These probes are generally between 1.5-2.5m in overall length depending on the application and device they are meant for.

2.4.2.1 Swept Langmuir and triple probes

The most prevalent diagnostic in medium-to-low temperature plasmas, the Langmuir probe, operates by recording the collected current, I, to a probe tip while an applied voltage, V, is scanned. The resulting I-V curve can then be analyzed to determine the ion density, floating potential, electron temperature and plasma potential at the probe location. In order to record entire I-V curves at a reasonable rate, a voltage sweep generator can

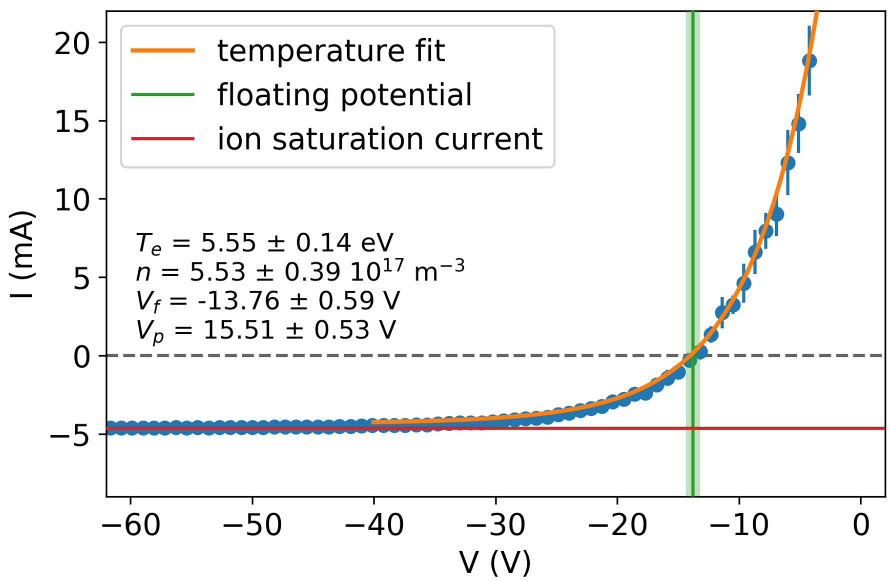

Figure 2.12: A typical I-V curve in a PCX discharge. The electron temperature fit (performed in log space) is shown along with the floating potential and ion saturation current.

be used to apply alternating voltages to a Langmuir tip while simultaneously measuring the associated plasma current. For the relatively slow time dynamics in most equilibrium PCX and BRB plasmas, the Langmuir sweep frequency is set at 100-500 Hz.

The analysis of Langmuir I-V curves in this work follows standard techniques for Maxwellian plasmas [35, 36, 37]. Before considering the I-V curve, it is necessary to remove offsets caused by the load across measuring resistors and to apply the appropriate factors from voltage dividers. Once the corrected voltage and current time traces are found, they are analyzed to find the peaks and valleys of the triangle wave voltage trace. Then both voltage and current time traces are cut up into individual sweeps (typically only up-sweeps are used to avoid any hysteresis caused by the tip heating up during electron saturation). At this point each sweep constitutes a single measurement point for the parameters that are derived from the I-V curve.

Figure 2.12 shows a typical I-V curve from a PCX plasma. The first parameter found is the floating potential, which is simply the voltage value where the current is zero. This can be taken as the point on the curve closest to $I = 0$ or, for higher precision, the zero current from a linear fit made with a handful of points near $I = 0$. Next, the ion saturation current is measured by finding the asymptotic value of the current as the voltage goes to $-\infty$. In some cases, sheath expansion must be taken into account at lower voltages by fitting a line to the current below the floating potential and subtracting this to find an ion saturation current. In other cases, as is common in multi-cusp confinement devices, there can be a hot tail of electrons that can be mistaken as sheath expansion. This effect can be seen when making multiple measurements at different distances from primary-electron producing cathodes.

The electron temperature is found by subtracting the ion current (with sheath expansion when applicable) from the total I-V curve and then making a linear fit in log space. Following the standard Langmuir analysis, the slope of the log space I-V curve between a few volts above the floating potential to a few volts below the plasma potential is equal to $1/T_e$. Typically, a lowest temperature fit technique is used where the fit window is scanned and the lowest temperature from the resulting set of fits is taken as the best value. In plasmas with hot tail electrons, a second temperature fit can be made if there is a clear two-slope curve in log space.

Once the electron temperature is found it can be used to calculate the ion density from the ion saturation current,

$$I_{isat} = 0.6neA\sqrt{\frac{kT_e}{m_i}} \tag{2.3}$$

where A is the area of the probe tip. Finally the plasma potential can be found by either determining the "knee" in the electron collecting portion of the I-V curve or by applying the Maxwellian simplification,

$$V_{\text{plasma}} - V_{\text{float}} = \frac{kT_e}{2e}\ln\left(\frac{2m_i}{\pi m_e}\right) \tag{2.4}$$

where this factor is about $3.5T_e$ for hydrogen, $4.2T_e$ for helium and $5.4T_e$ for argon. This simplification matches the "knee" approach fairly well for most steady plasmas produced on PCX and BRB and is used to avoid the need to sweep far into electron saturation where the tip can be heated from the increased current.

Due to the relative complexity of the I-V curve analysis and the need for a complex voltage sweep generator, triple probes are also used on BRB and PCX plasmas. The basic principle of a triple probe is to sample three points along the I-V curve with separate probe tips and then infer the floating potential, density and electron temperature from those points [38, 39]. For the triple probes used on BRB and PCX, four tips are used to remove the influence of the voltage divider required for the floating potential measurement. Figure 2.13 shows the circuit used for the triple probe measurements. A floating DC voltage supply, usually a stack of 9V batteries, drives a current through a circuit consisting of an ion saturation tip, the plasma and a mostly electron current collecting tip. The current through this circuit is taken as the ion saturation current that gives the ion density and the voltage between the electron collecting tip (V_+) and a floating tip (V_{float}) is used to calculate the electron temperature,

$$T_e = \frac{e(V_+ - V_{\text{float}})}{\ln 2} \tag{2.5}$$

This model assumes a perfect Maxwellian distribution, so the presence of sheath expansion or hot electrons will lead to erroneous values. Additionally, the different tips collect coatings at different rates, leading to unbalanced areas. In order to reduce this effect, the tips are permuted fairly often and are cleaned by biasing into ion saturation at the beginning of run days.

A huge advantage of the triple probe is the ability to let the circuit float to arbitrary potentials set by the plasma. In some cases in PCX and BRB, where injected current from the cathode exceeds the capacity of the anodes, the plasma potential can crash to roughly the cathode voltage [31]. When this happens, the ground-referenced sweep circuit for Langmuir probes can overload by drawing large electron currents. Replacement of these circuits is time consuming and fairly expensive, so when experiments are run where this plasma potential crash is possible, floating triple probes are preferred.

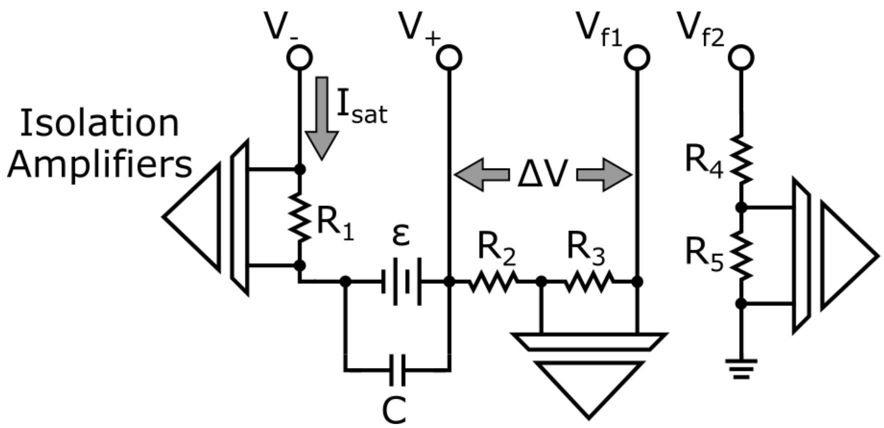

Figure 2.13: A sketch of the triple probe circuit. Image credit: Ethan Peterson [40]

2.4.2.2 Mach probes

The next most used diagnostic on WiPPL plasmas is the Mach probe, which measures ion flow. The basic principle of a Mach probe is to measure the ion saturation current on two equal-area faces, one facing the flow and one facing downstream. The difference in the collected current can then be inferred to give the Mach number of the flow, which is simply the factor of the sound speed of the flow. The most commonly used expression for the Mach number, M, is

$$\frac{J_A}{J_B} = e^{KM} \tag{2.6}$$

where J_A and J_B are the ion current densities on the upstream and downstream faces, respectively. The critical part of this expression is the factor, K, which typically ranges from 0.5-4 depending on plasma conditions and what model is being implemented. The original derivation of this theory called for a factor, $K = 4\sqrt{T_i/T_e}$ [41], but it has been shown that this model does not work well for many different plasma conditions, particularly unmagnetized plasmas like those on BRB and PCX [42].

In order to find a good value for K, groups have performed PIC simulations under certain parameters. The variation in derived K values and various plasma conditions is quite large, but an excellent review is given in [43]. For unmagnetized plasmas with $0.1 < T_i/T_e < 10$, PIC simulations have shown that $K = 1.34$ is an acceptable simplification [44].

For the work presented in this thesis this will be the value used unless otherwise noted. It is worth noting that this value is taken in the limit that the plasma Debye length is much smaller than the probe tip size. When the Debye length is large or comparable to the probe tip, complications can occur including collecting more current on the downstream side of the probe [45, 46]. Since plasmas in BRB and PCX have Debye lengths on the order of $10^{-5} - 10^{-6}$ m due to the relatively high density, this should not be a problem. Another complication that can arise due to collisions with neutral particles is shadowing of the flow by the probe [47]. Again, most BRB and PCX plasmas avoid this problem by having fairly long ion-neutral collision lengths.

Equation 2.6 describes the relationship between the Mach number and the current densities of the two probe faces, however the total current is what is measured. In order to correctly account for the differences in areas between the tips, an offset calculation is performed. First a measurement is made with face A directed upstream,

$$M_1 = \frac{1}{K}\ln\left(\frac{J_A}{J_B}\right) = \frac{1}{K}\left[\ln\left(\frac{I_A}{I_B}\right) - \ln\left(\frac{\mathbb{A}_A}{\mathbb{A}_B}\right)\right] \tag{2.7}$$

where $I \equiv J\mathbb{A}$ for both the faces. Then a second measurement is made with the probe flipped such that face B is directed upstream.

$$M_2 = \frac{1}{K}\ln\left(\frac{J_B'}{J_A'}\right) = \frac{1}{K}\left[\ln\left(\frac{I_B'}{I_A'}\right) + \ln\left(\frac{\mathbb{A}_A}{\mathbb{A}_B}\right)\right] \tag{2.8}$$

where the $'$ denotes this second measurement. Assuming that the flow is the same for these two cases, $M_1 = M_2$, the area ratio offset, Θ_{off}, is

$$\Theta_{\text{off}} \equiv \ln\left(\frac{\mathbb{A}_A}{\mathbb{A}_B}\right) = \frac{1}{2}\left[\ln\left(\frac{I_A}{I_B}\right) - \ln\left(\frac{I_B'}{I_A'}\right)\right] \tag{2.9}$$

This calculated offset can be taken into account for other Mach measurements made with face A directed upstream using,

$$M = \frac{1}{K}\left[\ln\left(\frac{I_A}{I_B}\right) - \Theta_{\text{off}}\right] \tag{2.10}$$

In practice, this calibration is performed at the beginning and end of any Mach probe scan to account for any changes that can occur day-to-day. In addition to calibrating the areas,

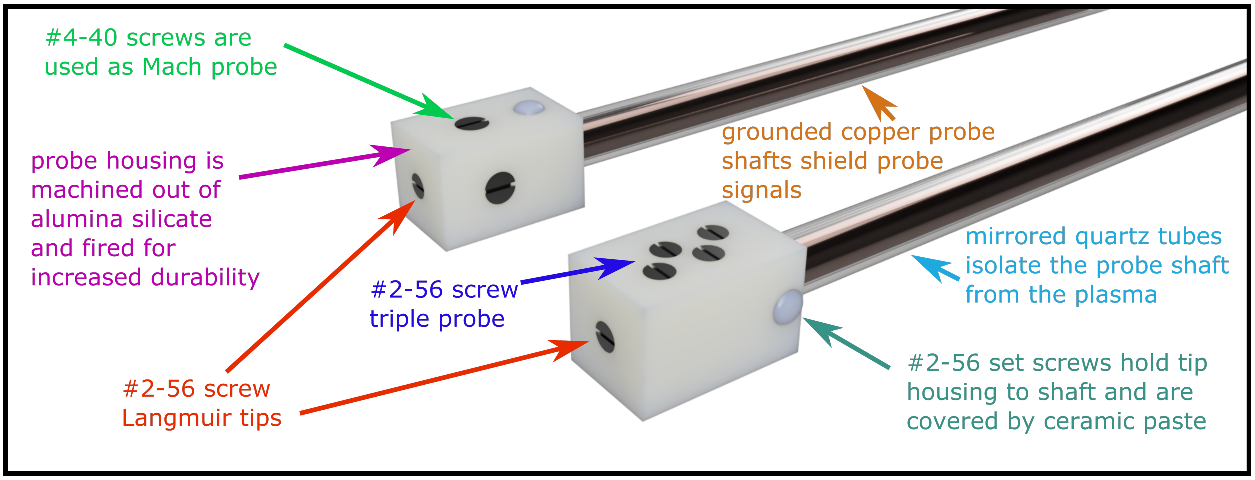

Figure 2.14: Image of a combination Mach/Langmuir (top) and a combination Triple/Langmuir (bottom) probe with the various features labeled.

this also will calibrate any multiplicative difference between the current measurements (such as different resistor values or isolation amplifier gains). If a single Mach measurement is needed rather than a scan, a single normal and flipped set of measurements, M_1 and M_2 averaged gives the Mach number with the offset removed. This is easily seen by adding together both of these expressions above.

2.4.2.3 Tip design

Since a major focus of WiPPL is producing flowing plasmas, it is important to be able to make local flow measurements with a probe. In order to calculate the actual velocity from a Mach probe a measurement of the sound speed is required. The additional tips on a combination Mach/Langmuir or Mach/Tripe probe can measure the local electron temperature either by a I-V curve fit or a triple probe technique.

Multi-tip probes are made by machining aluminum silicate and then firing the result in a furnace to ensure that the material is hardened and water-free. Aluminum silicate does come in easy-to-machine forms, but it is still quite challenging to produce these tips, often requiring several attempts and picking the best of the lot. In order to reduce the need to make many tips, they have been designed to be reusable. The metal tips are small #4-40 or #2-56 molybdenum flat-head screws, so the aluminum silicate only needs to have drilled and tapped countersunk holes instead of more difficult to produce mounting for flat faces. Additionally, the screws are used to mechanically hold the wire running down the probe. The aluminum silicate tip assemblies are mechanically secured to the copper probe shaft with small (#4-40) set screws. A small amount of ceramic paste is used to cover the set screw head, ensuring that the probe shaft is insulated from the plasma. Details of the combination probe tips are shown in Fig. 2.14.

2.4.3 Hall probe array

In addition to electrostatic probes, a 15 position, 3-axis linear Hall probe array can be inserted inside a quartz dip tube. More details of the construction and calibration of this array can be found in Ethan Peterson's thesis [40]. Positions are separated by 1.5 cm, for high-density measurements, or 3 cm, for lower density, on a custom PCB board that is mounted in a 3D printed housing. Due to the high heat load in denser plasmas, the Hall probe array is actively air cooled to ensure that the sensors operate at $\leq 50°$ C. The Hall array has a time resolution of roughly 100 kHZ and a sensitive of approximately 0.5 G. The Hall probe array is the main magnetic diagnostic for any long time-scale (> 500 ms) experiments at WiPPL.

The Hall probe array used on PCX uses a combination of high-sensitivity and low-sensitivity sensors (Melexis 91205LB and 91205HB, respectively) along the board to allow measurements to be made in the cusp field without saturating. The sensors are spaced 1.5 cm apart with the first (closest to the tip) 9 positions having a high-sensitivity of 28 mV/G and the last 6 positions having a low-sensitivity of 10 mV/G. The saturation limit of these sensors set by the power supply rail, which is ± 2.5 V. This means that the high sensitivity probes are accurate to about 90 G, while the low sensitivity probes are good to about 250 G.

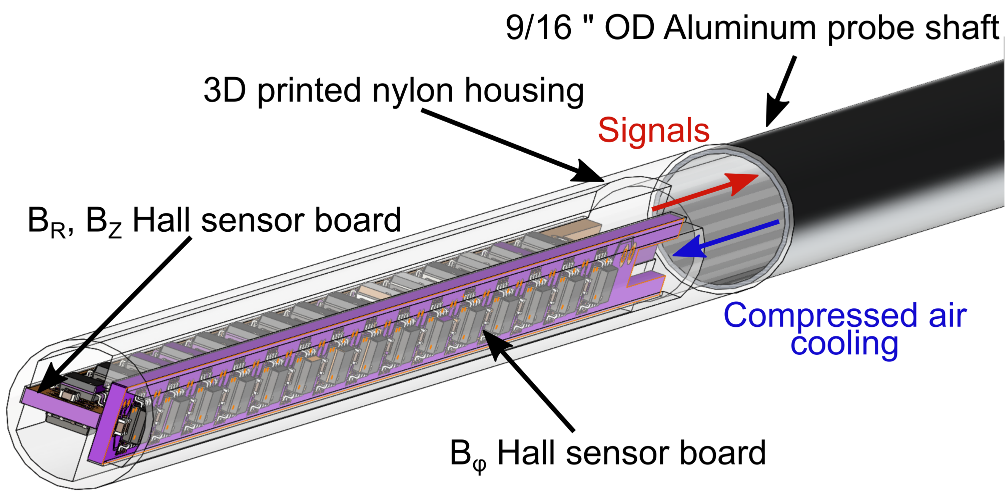

Figure 2.15: CAD image of a linear Hall probe array probe. Image credit: Ethan Peterson [40]

The Hall probe array offsets are calibrated by making measurements with the same magnetic field after flipping the probe 180°. For the B_z and B_ϕ measurements this is fairly simple since the Helmholtz coil set on PCX is axially aligned. (The B_ϕ offset is calibrated by simply turning the probe 90°). These offsets are typically small, but do lead to better measurements, especially at low field strengths. The B_r positions are more difficult to calibrate offsets, so they are typically less trusted than the B_z or B_ϕ positions. In the future, a 3-axis Helmholtz calibration set-up would greatly benefit these Hall probe arrays and make for very fast calibration. For the sensitivity, the minimum and maximum values provided in the datasheet for the sensors is taken to be 2σ of Gaussian error and propagated through any analysis.

2.4.4 mm-wave interferometer

For absolute density measurements and electrostatic probe calibration, BRB is equipped with a single chord mm-wave interferometer mounted near the south pole of the device. The design of this system was borrowed from a similar interferometer installed on the

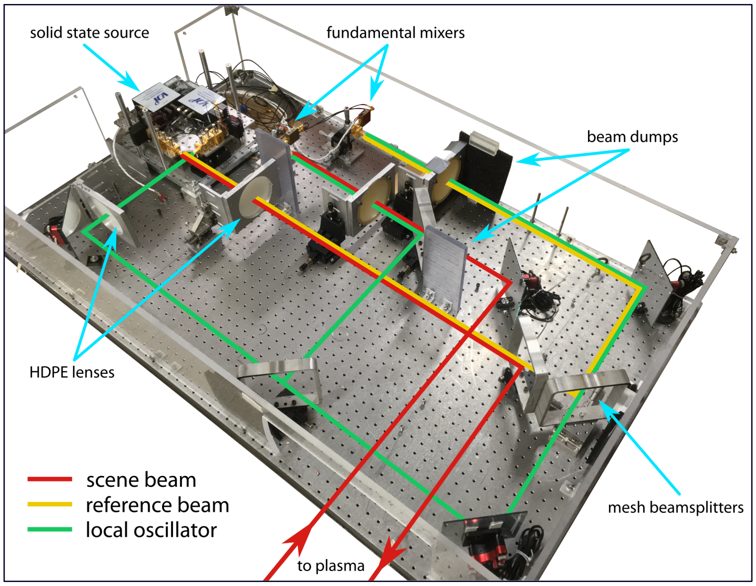

Figure 2.16: An image of the mm-wave interferometer with the various beam paths indicated. The solid state source produces two outputs: one is used for the interferometer measured and the other is used as a local oscillator input for the fundamental mixer detectors. The beams are directed with metallic mirrors, HDPE lens and mesh beam splitters.

Madison Symmetric Torus (MST) [48, 49]. Generally, far-infrared interferometery has been used to measure the absolute density of medium density plasmas in many different devices. Due to the in-house expertise, adapting the MST system to BRB was fairly straightforward. However, the long discharge time scales of BRB compared to MST has led to the development of a FPGA algorithm used for on-the-fly phase difference measurements, which allow the phase difference to be recorded at the intermediate frequency of the interferometer (approximately 1-10 MHz).

The basic principle of this measurement is based on the index of refraction change of an O-wave propagating through a plasma. Applying the cold-wave approximation for plasmas, the phase difference, $\Delta\phi$ between a beam traveling through a plasma with an electron density, n_e, and a reference beam traveling the same distance through air is [50],

$$\Delta\phi = \frac{\omega}{2cn_c}\int n_e\,dl \tag{2.11}$$

where $\omega \equiv 2\pi f$ and the cut-off density,

$$n_c = \frac{m_e}{\mu_0}\left(\frac{2\pi}{e\lambda}\right)^2 \tag{2.12}$$

is defined as the density above which the O-wave will not propagate in the plasma. This expression is valid when $n_e \ll n_c$, which is met when using a millimeter wavelength ($n_c \approx 10^{21}$ m^{-3}) in BRB plasmas ($n \approx 10^{17} - 10^{18}$ m^{-3}). The line integrated plasma density can be found by comparing the relative phase difference between an electromagnetic wave traveling through a plasma and a reference beam.

$$\bar{n}_e = \frac{4\pi c m_e \epsilon_0}{e^2}\frac{f\,\Delta\phi}{L} = 1.2\,\frac{f_{\mathrm{THz}}\,\Delta\phi_{\mathrm{rad}}}{L_{\mathrm{m}}}\ 10^{18}\mathrm{m}^{-3} \tag{2.13}$$

where L is the distance through the plasma and f is the wave frequency. In order to make good phase difference measurements, it is desirable to choose a beam frequency that will produce a large phase difference less than 2π for a given density. For BRB plasmas, millimeter wavelength ($f \simeq 0.3$ THz) beams are ideal in this respect.

The quasi-optical setup for the interferometer is shown in Figure 2.16. A solid-state source (Virigina Diodes VDI-Tx-S176) produces a fixed frequency beam at 319.9 GHz and an adjustable frequency synthesizer beam. The synthesizer beam frequency can be set via computer control between 314 GHz and 326 GHz. After setting the synthesizer frequency it is necessary to allow the oscillator to settle for roughly 10 minutes before making a measurement. Both of the beams from the source are emitted from WR2.8 wave-guide horns and are collimated by large high-density polyethylene (HDPE) lenses. At the far-infrared frequencies used here, HDPE works as an excellent lens material with an index of refraction of approximately 1.5 [51].

The fixed frequency beam is then sent to a mesh beam splitter to send one beam through the plasma (the scene beam) and keeping the other (reference beam) on the optics table. Mesh beam splitters are very effective in the far-infrared because metal is highly reflective to radiation at these wavelengths [52]. The beam splitters used on BRB are made up of a 70 lines per inch nickle mesh with 90% transmission bonded to a 6 in stainless steel frame.

Smaller splitters have been experimented with, but it was ultimately difficult to avoid reflections from the frame in these cases. The scene beam is sent through a box port window near the south pole of the BRB through the device to a pair of first surface mirrors which reflect the beam back through the plasma slightly offset along the box port.

The scene and reference beams are directed to a pair of fundamental mixers that use the adjustable frequency beam as a local oscillator to output a lower frequency signal. The resulting signal encodes the phase information of the beams, but at a frequency equal to the difference between the beam frequency and the local oscillator. Typically the adjustable frequency output is chosen so this intermediate frequency is between 1 and 10 Mhz. This signal is then sent to a pair of high-speed comparators (Analog Devices AD8561) that act as zero crossing detectors to effectively digitize the signals while maintaining the phase relationship.

The density calculations are performed on a FPGA that is fed the digital signals from the high-speed comparators. For discharges that last several seconds, it would be very resource intensive to fully record these 1-10 MHz signals at a high enough time resolution to perform good phase calculations. Rather, the FPGA operating at a clock frequency of roughly 100 MHz counts the clock cycles between zero crossings of both signals and computes the difference at every period. This difference is directly related to the phase lag between the signals. After the discharge, the FPGA outputs the recorded phase lag and the density is calculated.

2.4.5 Fabry-Pérot spectrometer

Perhaps the most exciting optical diagnostic at WiPPL is the Fabry-Pérot spectrometer, which measures the chord integrated ion distribution function with high precision. Moments of the distribution function, such as temperature and flow speed can be determined by fitting. Modeling a thermal broadened, Doppler shifted Maxwellian distribution, this diagnostic is capable of measuring ion temperatures with < 0.1 eV precision and flow

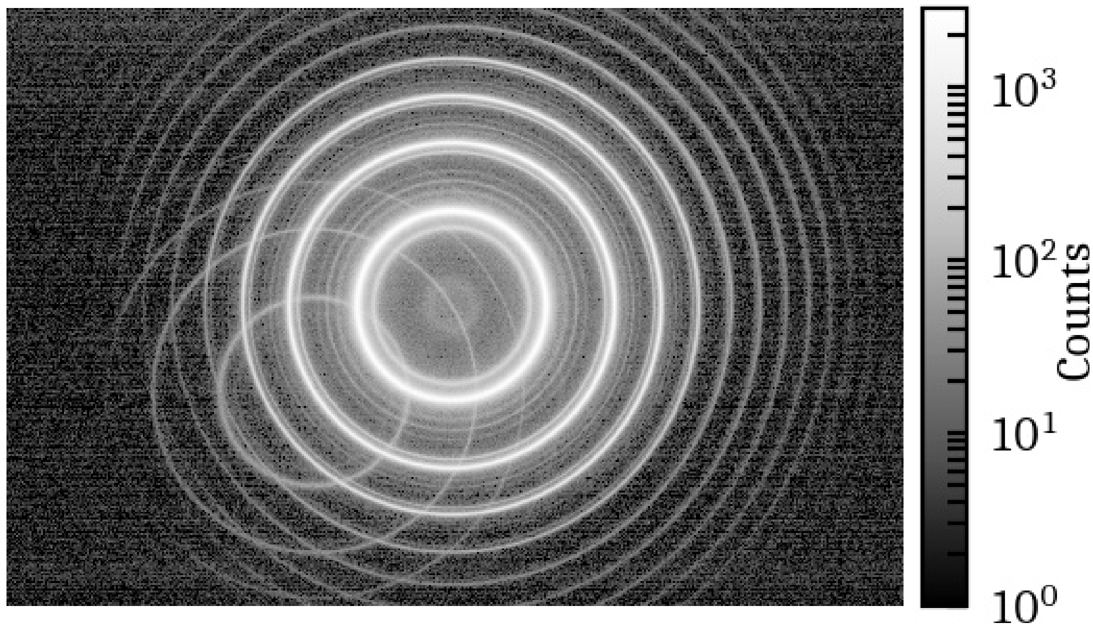

Figure 2.17: Fabry-Pérot image of Th Ar-fill hollow cathode lamp. The log scale emphasizes the undesirable secondary ring pattern from misalignment.

speeds at the 10 m/s level. This section will provide more detail on the Fabry-Pérot's design and analysis to highlight this novel optical diagnostic.

2.4.5.1 Basic operating principle

At the core of the diagnostic, is a Fabry-Pérot etalon, which consists of two highly reflective plates carefully spaced a set distance apart. For the Fabry-Pérot system at WiPPL, this spacing is approximately 0.88 mm with mirror plates roughly 50 mm in diameter. The plates must be very flat, therefore only the central 10-15 mm is used for the diagnostic. When light is shined into an etalon, rays reflect many times between the plates and constructively interfere according to the condition, [53]

$$m\lambda = 2nd\cos\theta \quad m \in 0, 1, ..., m_0 = \text{Floor}\left(\frac{2nd}{\lambda}\right) \tag{2.14}$$

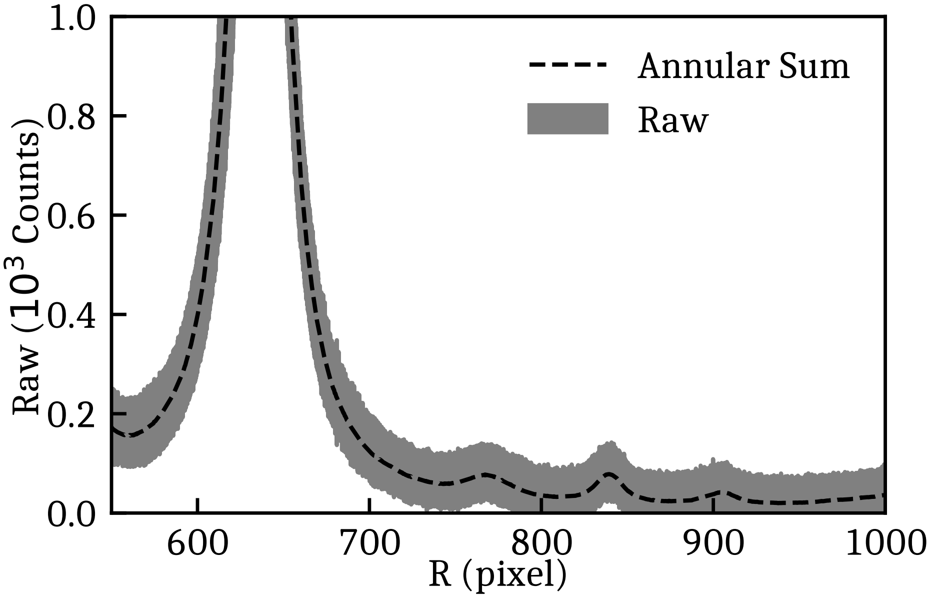

Figure 2.18: Intensity in counts is shown as a function of radius from the center of the ring pattern. Annular Summing reduces the uncertainty of the mean counts in a bin to approximately 1 count.

where n is the index of refraction in the cavity, d is the cavity spacing, m is the integer order number of interference, and θ is the angle which the light ray enters/exits the cavity with respect to the optical axis. The result of this interference is a characteristic ring pattern (shown in Fig. 2.17) where each ring represents a wavelength peak in the incoming light spectrum and rings are repeated at different orders.

2.4.5.2 Design and optimization

The ring pattern is imaged using a 2D CCD/CMOS array; either a commercial DSLR or a scientific camera from Thorlabs. Since the rings are ideally axisymmetric, the data can be reduced through a ring summing technique [54, 55]. Individual pixels are binned by their radial distance from the center and then averaged in these bins to produce a 1D intensity profile. Ring summing not only helps reduce the data for quicker analysis, but

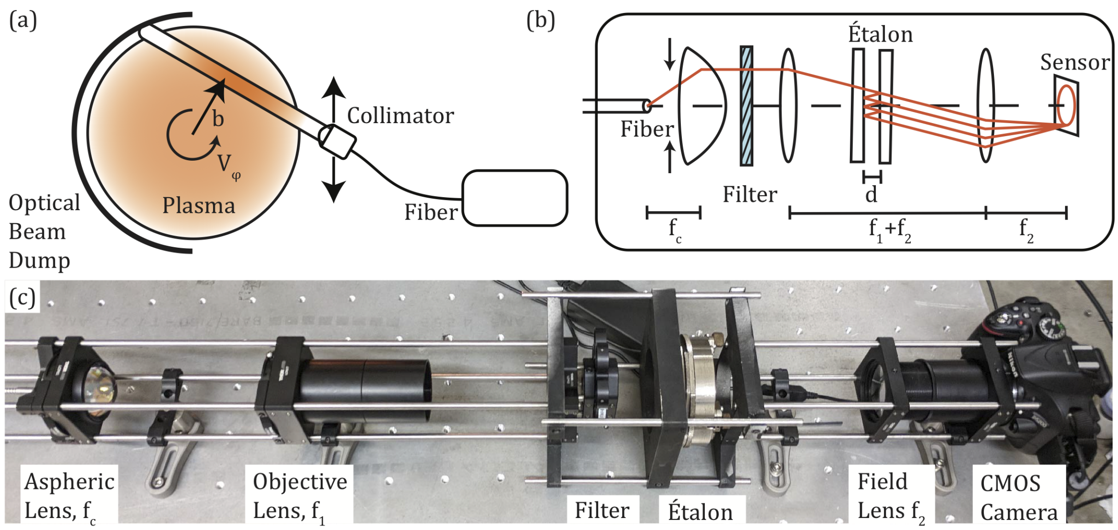

Figure 2.19: (a) Fabry-Pérot optical schematic. Light is collected from the plasma with a f/1.0 collimator mounted on a linear stage to allow scanning of the plasma volume. The chord's closest distance to the origin is labeled by its impact factor, b. An optical beam dump is located on the far side of the vessel to limit reflected light from entering the collimator. (b) Optical Schematic of Fabry-Pérot. (c) Picture of Fabry-Pérot. Light from the fiber is collimated by a f/1.0 collimator and focused by the objective lens ($f_1 = 350$ mm) onto 5 mm spot size on the étalon ($d = 0.88$ mm). The light exiting the étalon is focused onto the CMOS sensor via the field lens ($f_2 = 150$ mm) as concentric rings due to the interference condition, Eq. 2.14. Image credit: [56]

also drastically improves the signal-to-noise ratio by way of averaging. An example of this improvement is shown in Fig. 2.18.

The ion light that is captured from the plasma is dim enough that special design considerations were needed to ensure a large enough étendu for the spectrometer. Several iterations of setups were used before arriving at the final version which is made up of a high numerical aperture collimator, a thick optical fiber bundle, and a rail-mounted imaging system, shown in Fig. 2.19. The imaging stage is a telescope which ensures that the full view of the collimator is focused onto the sensor plane of the camera. The etalon and a

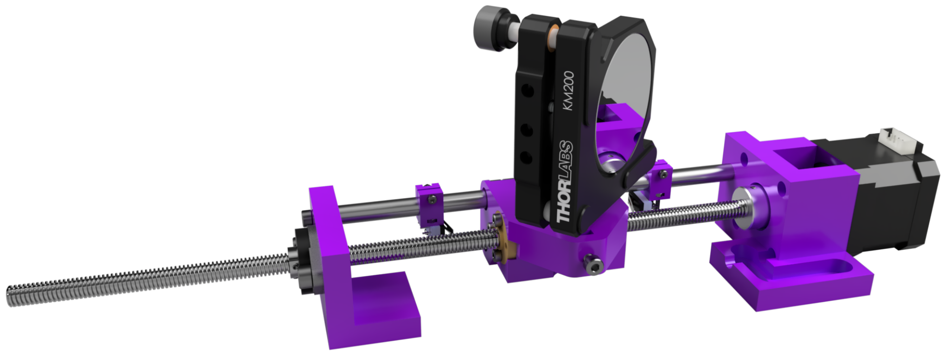

Figure 2.20: A stepper motor driven mirror is used to switch the collimator's view from the plasma to the calibration lamp after every shot. This is necessary to track the small variance in absolute calibration needed for precise velocity measurements. The parts highlighted in purple were 3D printed and the rest of the system was produced with spare parts from around the lab.

notch filter are placed in the telescope section where the beam is smallest. The camera focus is adjusted by selecting the focus that produces the narrowest rings (since broadening can be introduced by poor focus).

2.4.5.3 Analysis and performance

After the Fabry-Pérot image has been captured and ring-summed, the data must be properly analyzed to obtain the ion distribution function. Most Fabry-Pérot systems are used in situations with no time dynamics, so they can be calibrated relatively as a parameter such as the index of refraction or etalon spacing is scanned. For WiPPL plasmas, however, this is not an option, rather an absolute calibration is required. To do this, a thorium hollow-cathode lamp is imaged with the Fabry-Pérot after every discharge (the mechanism for this is shown in Fig. 2.20). The lines in the lamp are well known and the temperature of the lamp is very small compared to expected broadening from either an argon or helium plasma. Through a Bayesian statistics approach, called Multimodal Nested Sampling [57], the locations of the spectral peaks of this lamp can provide a calibration for the necessary parameters. This statistical technique is required because the interference condition produces fairly similar fits over a wide range of order number, but a single order is needed for calibration. A much more detailed description of this calibration and analysis is presented in [56] and Jason Milhone's thesis [58].

Chapter 3

Exciting a Flow-Driven Instability

An obviously necessary feature of any experiment that wishes to observe a flow-driven instability is the ability to drive strong, sheared flows. Taylor-Couette flow[1], where a fluid held between two concentric cylinders is stirred at the inner and outer boundaries, is one of the most common flow configurations in hydrodynamics. Starting with Newton himself, this simple geometry has served as theoretical and experimental platform for hydrodynamics for over 300 years [59]. Couette flow was considered by Stokes when constructing the ubiquitous Navier-Stokes equations of fluid motion. It served as the basis for the design of the earliest viscometers, where the name Couette comes from [60, 61]. Couette flow has also been a major tool in modern studies of fluid turbulence, particularly the pioneering work of Taylor [62]. Extending beyond conventional fluids, Couette flow has been used to characterize more complex fluids such as visco-elastic polymers [63, 64] and magneto-fluids such as liquid metals, where the flowing fluid is subject to electromagnetic forces in addition to pressure and viscosity. Chandrasekhar and Velikhov simultaneously described the stability of MHD Couette flow in the presence of weak magnetic fields [3, 2], deriving the magnetorotational instability (MRI), which is a major focus of this work.

Building off of this long history of research, plasma Couette flow opens up experiments to wider range of phenomena associated with kinetic effects, compressibility, and two-fluid dynamics. Plasma Couette flow stands apart from Couette flow in conventional

[1] Taylor-Couette flow specifically relates to the flow in a cylindrical geometry, while Couette flow is any differentially driven flow. Often these two terms are used interchangeably.

liquids because stirring can not be achieved mechanically. This is due to the low particle density of most plasmas ($\lesssim 10^{22}$ m^{-3}) compared to other fluids. Rather, an electromagnetic stirring method is used at the boundaries of the cylindrical plasma volume, driving Couette flow profiles [23, 24].

In this chapter I will outline the model of plasma Taylor-Couette flow (TCF) and discuss the effect of viscosity and neutral collisions on momentum transport. Then I will present a global stability analysis of plasma Taylor-Couette flows with respect to the magnetorotational instability as well as interchange-like fluid instabilities. I will show how the two-fluid Hall effect and neutral collisions can drastically alter the linear growth of the MRI in these flows and outline a real experimental parameter space for observing the MRI. Finally, I will discuss the prospects of reaching the required parameters in current plasma experiments and motivate alternative methods of flow drive. This chapter is largely based off of the study presented in [26] with an updated discussion of the experimental prospects for observing the MRI.

3.1 Plasma Couette flow

In order to drive Couette flow in an unmagnetized plasma (or any fluid for that matter), torque must be imparted near the edge that then viscously couples inward to the bulk. In conventional fluids, this torque is usually provided by rotating inner and outer boundaries. In plasmas, the applied torque can come in the form of gradient drifts, plasma injection (neutral beams), or electromagnetic forces. In this work, edge torque is imparted via electromagnetic forces, specifically the $\mathbf{J} \times \mathbf{B}$ Lorentz force, in which a perpendicular alignment of an plasma current and magnetic fields forces both plasma ions and electrons in the same direction (see Fig. 2.11 in Chapter 2). In PCX, measured edge-drive flow profiles are well described as a balance between the viscosity of the ion fluid and the momentum loss to charge exchange collisions [23, 27].

Ions carry most of the momentum in a plasma flow, so ion viscosity is the dominant coupling mechanism for the bulk flow. As defined by the Braginskii transport coefficients

[21], unmagnetized ion kinematic viscosity is given by the expression,

$$\nu_i = 0.96 V_{thi}^2 \tau_{ii} \quad , \tag{3.1}$$

where V_{thi} is the ion thermal speed and τ_{ii} is the ion-ion collision time. Viscosity in fluids is a diffusive process and is mathematically described by the Laplacian of the flow,

$$F_{\text{visc.}} \propto \nu_i \nabla^2 \mathbf{V} \quad . \tag{3.2}$$

In addition to viscosity, there is a force exerted on the plasma caused by charge-exchange collisions with neutral particles. In these collisions, slow, cold neutral particles collide with the flowing ions and transfer an electron to render the flowing particle a fast neutral that quickly leaves the volume and replace it with a slow ion. The ionization mean-free path for neutrals is larger than the experiment size, so neutrals are not strongly coupled to ions. Therefore, we can assume a uniform background of stationary neutrals that act as a momentum sink on the total ion flow,

$$F_{\text{neut.}} \propto -\frac{\mathbf{V}}{\tau_{i0}} \quad , \tag{3.3}$$

where $\tau_{i0} \equiv (n_0 < \sigma_{cx} V >)^{-1}$ is the ion-neutral charge exchange collision time, which can be determined by looking up the correct cross section for a given gas species and using the ion thermal speed as the mean velocity. For this work, the cross sections used are $\sigma_{cx} = 6 \times 10^{-19}\, T_i^{-0.093}$ m^2 for argon [65] and $\sigma_{cx} = 3 \times 10^{-19}\, T_i^{-0.106}$ m^2 for helium [66].

In the unmagnetized bulk of the flowing plasma, these are the only two forces exerted on the plasma in the azimuthal direction. Working in a cylindrical geometry, the two forces can be added to produce a Bessel differential equation for the flow equilibrium as a function of r,

$$\frac{\partial^2 V_\phi}{\partial r^2} + \frac{1}{r}\frac{\partial V_\phi}{\partial r} - \left(\frac{1}{L_\nu^2} - \frac{1}{r^2}\right) V_\phi = 0 \tag{3.4}$$

where L_ν is the momentum diffusion length defined by,

$$L_\nu \equiv \sqrt{\nu_i \tau_{i0}} \tag{3.5}$$

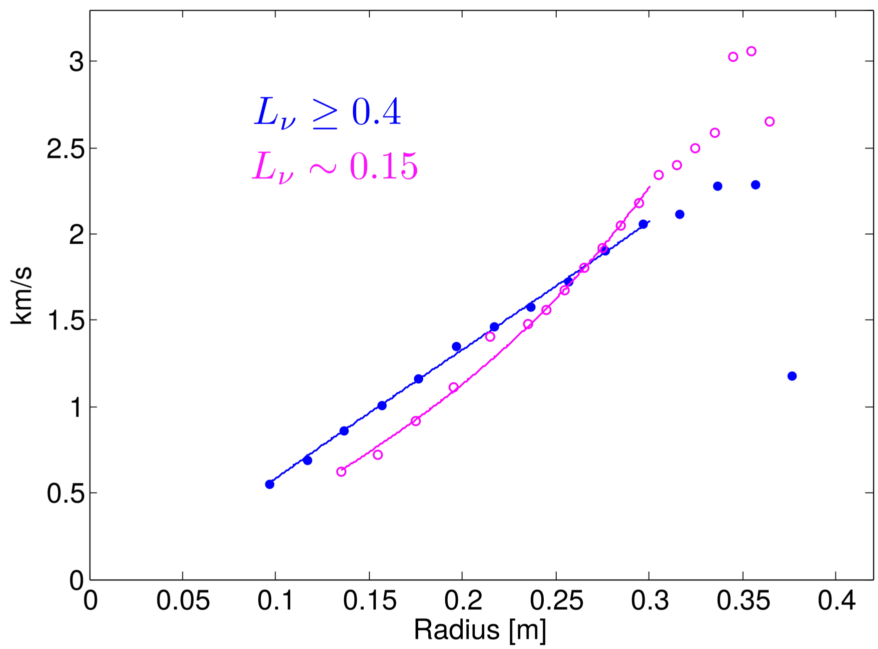

Figure 3.1: Two radial flow flow profiles measured on PCX. Argon plasmas (blue profile) can be produced with a fairly high ionization fraction, leading to a long momentum diffusion length. In helium discharges (pink profile) the ionization fraction is much lower and the resulting momentum diffusion length is shorter than the plasma radius. The fits of these profiles are made with Eq. 3.6. Image credit: [23]

The solution of this differential equation is a linear combination of the modified Bessel functions,

$$V_\phi(r) = A\mathcal{I}_1(r/L_\nu) + B\mathcal{K}_1(r/L_\nu) \tag{3.6}$$

with

$$A \equiv \frac{\mathcal{K}_1(R_2/L_\nu)V_1 - \mathcal{K}_1(R_1/L_\nu)V_2}{\mathcal{I}_1(R_1/L_\nu)\mathcal{K}_1(R_2/L_\nu) - \mathcal{I}_1(R_2/L_\nu)\mathcal{K}_1(R_1/L_\nu)} \tag{3.7}$$

$$B \equiv \frac{\mathcal{I}_1(R_1/L_\nu)V_2 - \mathcal{I}_1(R_2/L_\nu)V_1}{\mathcal{I}_1(R_1/L_\nu)\mathcal{K}_1(R_2/L_\nu) - \mathcal{I}_1(R_2/L_\nu)\mathcal{K}_1(R_1/L_\nu)} \tag{3.8}$$

where R_1 and R_2 are the inner and outer boundary radii, respectively, and V_1 and V_2 are the inner and outer edge velocities, respectively. This solution is set by the radii and velocity at the inner and outer boundaries and the momentum diffusion length. Examples of these modified Taylor-Couette flow (TCF) profiles are shown in in Fig. 3.1.

The momentum diffusion length is the effective distance over which momentum can be transported from electrodes on the edge towards the center of the plasma. If L_ν is larger than the system size, momentum can be efficiently coupled from the edge, but if L_ν is smaller, the bulk plasma will not spin up because neutral charge-exchange collisions inhibit momentum transport. The momentum diffusion length can be recast in terms of operating parameters for a plasma as[2],

$$L_\nu = \sqrt{\frac{5.43\pi\epsilon_0^2}{\sigma_{cx}\ln\Lambda_{ii}e^4}}\frac{T_i}{\sqrt{nn_0}} \simeq 1\text{ m}\,\frac{T_{i,eV}}{\sqrt{n_{11}n_{0,11}}} \tag{3.9}$$

At first look, it seems that in order to increase the momentum diffusion length an experiment must operate at low densities. While this does work, it has been shown empirically to be more difficult to drive the flow at lower densities [27]. Rather, the collisional heating of the ions can be leveraged at higher densities, while working to increase the ionization fraction (lower n_0).

Differential flow profiles have been produced in PCX with a center stack stirring assembly on the inner boundary [24] (see Fig. 1.4 from Ch. 1). These profiles were very well

[2]Notably, this expression is not explicitly dependent on the ion mass; however, the charge-exchange cross section will depend on the ion species.

matched with the Bessel function expression in Eq. 3.6, leaving the momentum diffusion length as a fitting parameter. Despite this success these flows did not produce any unstable behavior, mainly because drive was only attempted in the fully unmagnetized case with no applied field. Additionally, the assembly used to drive flow at the inner boundary proved to be difficult to maintain and challenging to drive large torques via the necessarily small tungsten cathodes.

3.2 Magnetorotational instability in Taylor-Couette flow

In this section, I will outline the global stability analysis conducted to determine the stability threshold for the MRI in Taylor-Couette flows on PCX. This analysis includes both the Hall term and neutral drag effects. Previous global stability analyses for PCX have included the Hall term, but not the neutral drag body force [67]. The analysis produced a stability parameter space that highlights the limiting factors for exciting the MRI in PCX.

3.2.1 Global stability model

In order to capture both the Hall and neutral collision effects, an incompressible dissipative Hall MHD model with collisional neutral drag is used. The neutral drag body force is included as a momentum sink term dependent on the momentum diffusion length. The governing equations used for this analysis are:

$$\frac{\partial \mathbf{V}}{\partial t} = -(\mathbf{V}\cdot\nabla)\mathbf{V} - \nabla\frac{P}{\rho} + \frac{1}{\mu_0\rho}(\nabla\times\mathbf{B})\times\mathbf{B} + \nu\nabla^2\mathbf{V} - \frac{1}{\tau_{i0}}\mathbf{V} \tag{3.10}$$

$$\nabla\cdot\mathbf{V} = 0 \tag{3.11}$$

$$\frac{\partial \mathbf{B}}{\partial t} = \nabla\times\left[\mathbf{V}\times\mathbf{B} - \frac{1}{\mu_0 ne}(\nabla\times\mathbf{B})\times\mathbf{B}\right] + \eta\nabla^2\mathbf{B} \tag{3.12}$$

$$\nabla\cdot\mathbf{B} = 0 \tag{3.13}$$

where P is the scalar pressure, ρ is the mass density and η is the magnetic diffusivity (in m^2 s^{-1}). In these equations, plasma parameters n_e, ρ, τ_{i0}, ν and η are assumed to be constant and uniform throughout the volume. Measured profiles of T_e and n_e on PCX from Langmuir probes and the OES system support this assumption.

In order to study linear stability these equations are cast in terms of non-dimensional parameters and linearized near the equilibrium state: $\mathbf{V}_{eq} = V_\phi(r)\,\mathbf{e}_\phi$ and $\mathbf{B}_{eq} = B_0\,\mathbf{e}_z$. The unit of length is the radius of the inner cylindrical boundary R_1 and the unit of velocity is the plasma velocity at this boundary, so $\mathbf{V} = V_1\mathbf{v}$ and $P = \rho V_1^2 p$. The magnetic field is normalized by the applied axial field: $\mathbf{B} = B_0\mathbf{b}$. The dimensionless equations are

$$\gamma\mathbf{v} = -\left(\mathbf{v}_{eq}\cdot\nabla\right)\mathbf{v} - (\mathbf{v}\cdot\nabla)\mathbf{v}_{eq} - \nabla p + \frac{1}{M_A^2}(\nabla\times\mathbf{b})\times\mathbf{b}_{eq} + \frac{1}{Re}\left(\nabla^2 - \mu^2\right)\mathbf{v} \quad (3.14)$$

$$\nabla\cdot\mathbf{v} = 0 \quad (3.15)$$

$$\gamma\mathbf{b} = \nabla\times\left[\mathbf{v}_{eq}\times\mathbf{b} + \mathbf{v}\times\mathbf{b}_{eq} - \frac{\delta_i}{M_A}(\nabla\times\mathbf{b})\times\mathbf{b}_{eq}\right] + \frac{1}{Rm}\nabla^2\mathbf{b} \quad (3.16)$$

$$\nabla\cdot\mathbf{b} = 0 \quad (3.17)$$

where γ is the growth rate in units of angular frequency $\Omega_1 \equiv V_1/R_1$. The dimensionless parameters that enter these equations are: the fluid Reynolds number, $Re \equiv V_1R_1/\nu$; the magnetic Reynolds number, $Rm \equiv V_1R_1/\eta$; the Alfvén Mach number, $M_A \equiv V_1/V_A \equiv V_1\sqrt{\mu_0\rho}/B_0$; the normalized ion inertial length for the Hall effect, $\delta_i \equiv d_i/R_1 \equiv c/(\omega_{pi}R_1)$; and the normalized momentum diffusion length for the neutral collision effect, $\mu \equiv R_1/L_\nu \equiv R_1/\sqrt{\tau_{i0}\nu}$. Equations (3.14)-(3.17) are solved for axisymmetric modes using a standard finite difference eigenvalue method assuming no-slip, non-conducting side walls and periodicity in the axial direction. The numerical methods used are more fully described in [68].

In this stability analysis the effect of the neutral drag enters consistently both through the modification of the equilibrium rotation profile (see Fig. 3.2) and as a drag force in the linearized momentum equation. In this way, the damping effect of the neutral collisions affects both the initial flow shear in the system and the linear growth of the instability. The equilibrium profile is set using chosen boundary velocities, rather than solving for the flow drive with a given current. This has the advantage of having the simple Bessel function form from Eq. 3.6. Additionally, the top and bottom boundaries are periodic, removing the effects of Ekman circulation and Hartmann layers. These assumptions greatly simplify present analysis, allowing us to focus on the global MRI physics and not on the boundary

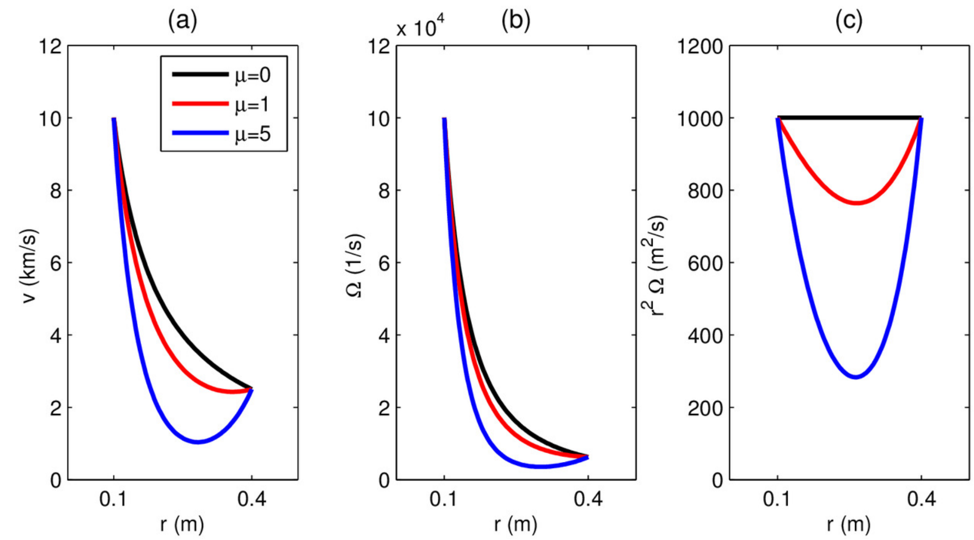

Figure 3.2: Input profiles of the (a) toroidal velocity, (b) angular frequency, and (c) angular momentum of modified Taylor-Couette flow with different $\mu \equiv R_1/L_\nu$ values. The effect of the neutral drag is increased at greater values of μ. The profiles in this figure all have the same edge boundary conditions, but a increasingly smaller momentum diffusion length (or larger μ). The case with no neutral drag would be unstable to the MRI, but those with more neutrals present become hydrodynamically unstable.

effects. In the experiment, these boundary layers effectively reduce the threshold for fluid instabilities and would warrant their own analysis.

Unless otherwise noted, all the analysis in this section is done assuming a singly ionized ($Z = 1$ and $n_e = n_i \equiv n$) helium plasma with $T_e = 12$ eV and $T_i = 0.4$ eV. Fixing the temperatures allows viscosity to vary only with density and resistivity, η, to be mostly fixed (there is a weak density dependence in the Coulomb logarithm). The dimensions of this system are matched to PCX, $R_1 = 0.1$ m, $R_2 = 0.4$ m, and $H = 0.8$ m, where the height determines the axial wave-number $k_z = 2\pi/H$. The boundary flow velocities for the equilibrium are chosen to give a $v_\phi \propto 1/r$ profile when no neutrals are present. A $v_\phi \propto 1/r$ profile marginally meets the Rayleigh criterion (but is fully stable when viscosity is included) [69] and meets the ideal-MRI condition [4]. For this analysis an inner velocity

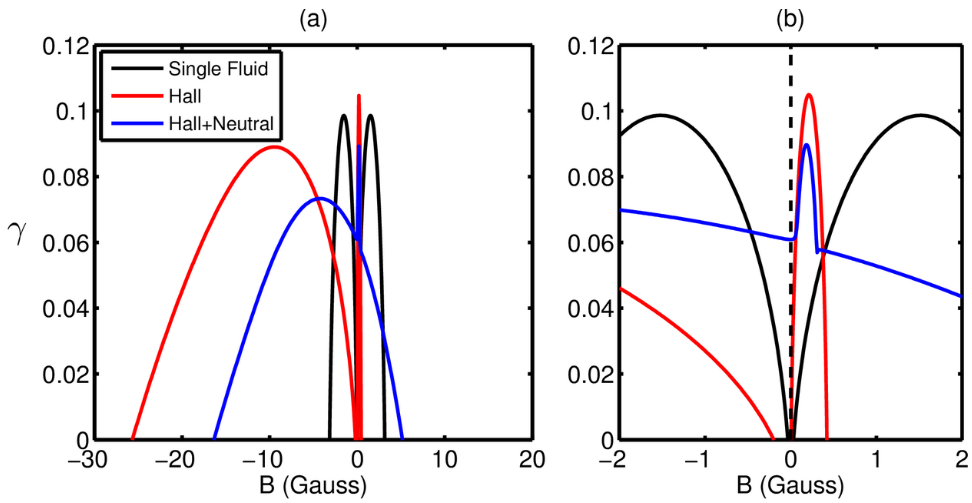

Figure 3.3: Growth rate, γ in units of Ω_1, plotted as a function of applied magnetic field. The different curves present the single fluid MHD case, the inclusion of the Hall term and the inclusion of neutral charge exchange collisions. For this plot $n_e = 10^{18}$ m^{-3} and $P_0 = 10^{-5}$ torr corresponding to $\delta = 4.55$ and $\mu = 0.95$. (a) The full range of magnetic field that gives positive MRI growth rates. (b) A close-up view near $B_0 = 0$ shows the small (less than earth field) positive B_0 branch for the Hall and Hall+Neutral cases.

of $V_1 = 10$ km/s was chosen, which sets $V_2 = 2.5$ km/s when a $v_\phi \propto 1/r$ profile is desired (see Fig. 3.2). All of these fixed values fall into the range of parameters and flows that can be reached on PCX in an edge-drive configuration.

3.2.2 Stability phase space

The Hall and neutral drag momentum sink terms both produce large qualitative effects on the stability of flows as shown in Fig. 3.3. For the case when neither of these terms are included (single fluid MHD) positive MRI growth rates occur for very small magnitude magnetic fields (on the order of Earth's field) both parallel and antiparallel to the axis of rotation. This is in agreement with the simple ideal MRI condition where the maximum field for instability is set by the magnitude of the flow shear and the smallest wavenumber available to the system.

When the Hall term is included, positive MRI growth rates are found for stronger magnetic fields and only when the field is antiparallel to the axis of rotation (negative values of B_0 in this analysis)[3]. This Hall asymmetry is a well-known fact caused by the handedness of the electron motion, where right-hand circularly polarized waves (whistlers) act to either enhance or diminish flow shear [70, 71]. It is also notable that the effect of the Hall term widens the range of field strengths that produce a positive growth rate for a given wavenumber. Experimentally, this is useful because it allows for larger, easier to measure magnetic fields.

If the neutral drag term is added as well, the growth rate is slightly reduced and the magnetic field at the peak growth rate is smaller in magnitude. In heavily neutral dominated analysis, the MRI growth rate is always reduced from the fully ionized value when there is sufficient neutral coupling [72]. This is very similar to the effect of adding in viscous and resistive dissipation. The more dramatic effect of neutral collisions is the increased shear but reduced velocity in the equilibrium flow profile. As neutral collisions become more dominant, the increased shear drives a hydrodynamic instability (positive growth rate at $B_0 = 0$) at the particular plasma density and pressure shown in Fig. 3.3. Under this condition, the momentum injected at the inner and outer boundaries does not couple across the whole profile. With fixed boundary velocities, this leads to increased shear at the edges of the flow profile. If the shear is great enough, the Rayleigh criterion is violated for a portion of the profile near the inner boundary, causing the hydrodynamic instability. In order to distinguish this interchange-like hydrodynamic instability from the MRI, it is necessary to find a region in parameter space where the momentum diffusion length is sufficiently large and the MRI can still be excited with a weak B_0.

For experimental reference it is important to determine real operating parameters that produce a growing MRI mode. By fixing, T_e, T_i, V_1, V_2 and the dimensions of the system, the remaining variable plasma parameters are the plasma density, n; the neutral pressure,

[3]There is a small positive B branch of the Hall MRI, but the magnitude of these fields is much smaller than earth's field and would not be controllable in the experiment.

P_0; and the magnetic field B_0. In a real experimental setting the density and neutral pressure are linked by the confinement time and power input of the system, which are both reasonable parameters to use as design points. Given these three variables, the dimensionless parameters of interest to this analysis have the following dependencies:

$$\delta_i \propto n^{-1/2} \tag{3.18}$$

$$\mu \propto (nP_0 \ln \Lambda_{ii})^{1/2} \tag{3.19}$$

$$M_A \propto n^{1/2} B_0^{-1} \tag{3.20}$$

$$Re \propto n \log \Lambda_{ii} \tag{3.21}$$

$$Pm \propto (n \log \Lambda_{ii} \log \Lambda_{ei})^{-1} \tag{3.22}$$

where $\log \Lambda_{ii}$ and $\log \Lambda_{ei}$ are the weakly density dependent Coulomb logarithms for ion-ion and electron-ion collisions, respectively.

Using neutral pressure and density to map out a phase space, regions of stability can be identified with respect to the MRI and hydrodynamic instabilities as shown in Fig. 3.4. This map is produced by choosing the magnetic field for each n-P_0 point that corresponds to the maximum growth rate. If the maximum growth rate is less than zero (region I), then the system will be stable. Region II represents the region where a MRI experiment would need to operate, where the maximum growth rate is positive for non-zero B. Here flowing plasmas are hydrodynamically stable, but an applied axial magnetic field sets off the MRI. It is clear that to ensure that an experiment is in region II with these fixed temperatures and flow velocities, the neutral pressure must be as low as possible and the density must be neither too low nor too high. At higher neutral pressures and higher densities, μ can become of order unity, at which point the shear in the velocity profile caused by neutral drag is large enough to trigger hydrodynamic instabilities (region III). The MRI threshold between region I and region II appears to be set mainly by the density, i.e. viscosity. For low enough densities, the viscosity is large enough to damp out any instabilities.

The onset of the hydrodynamic instability can be seen when scanning density at a fixed neutral pressure as in Fig. 3.5. For a given neutral pressure there is a density (i.e. viscosity)

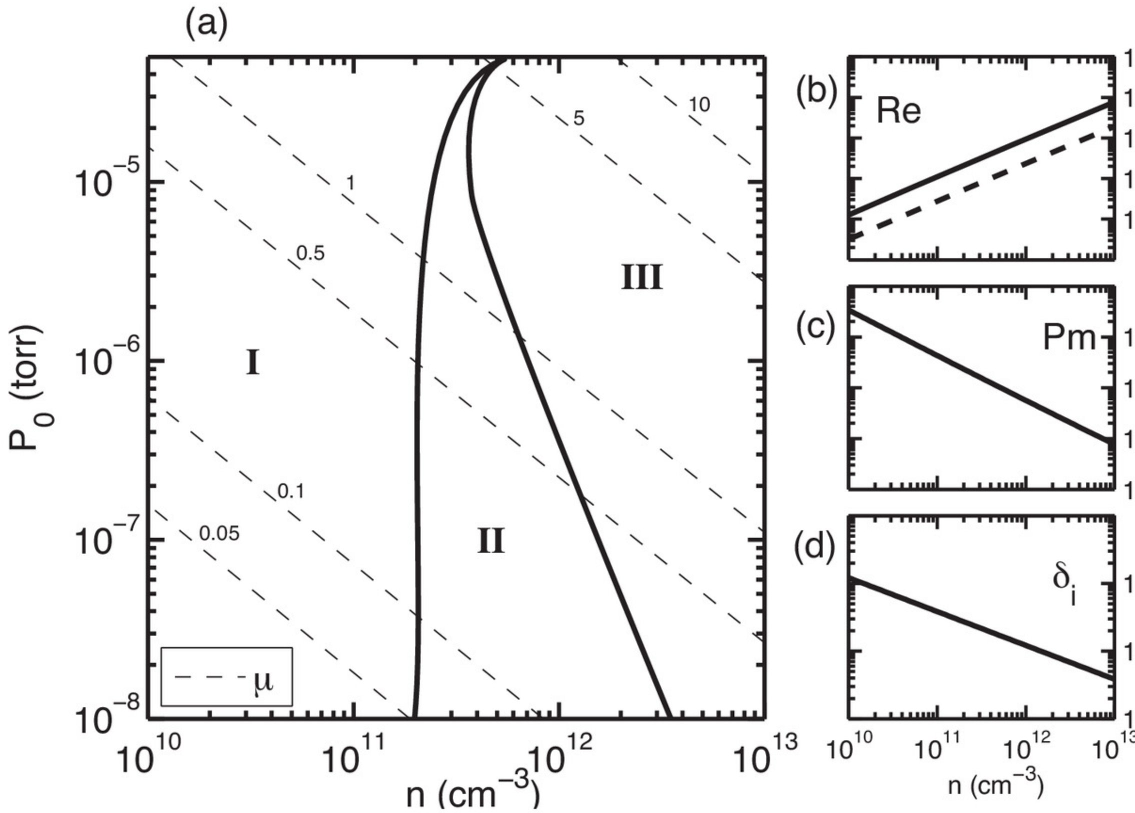

Figure 3.4: (a) Stability curves as functions of n and P_0. Region I is stable. Region II is hydrodynamically stable, but unstable to the MRI. Region III is hydrodynamically and MRI unstable. Contours of μ are also plotted. On the right, the density dependence of (b) Re for both V_1 (solid) and V_2 (dashed), (c) $Pm \equiv Rm/Re$, and (d) δ_i are plotted to highlight how relevant dimensionless parameters scale with density.

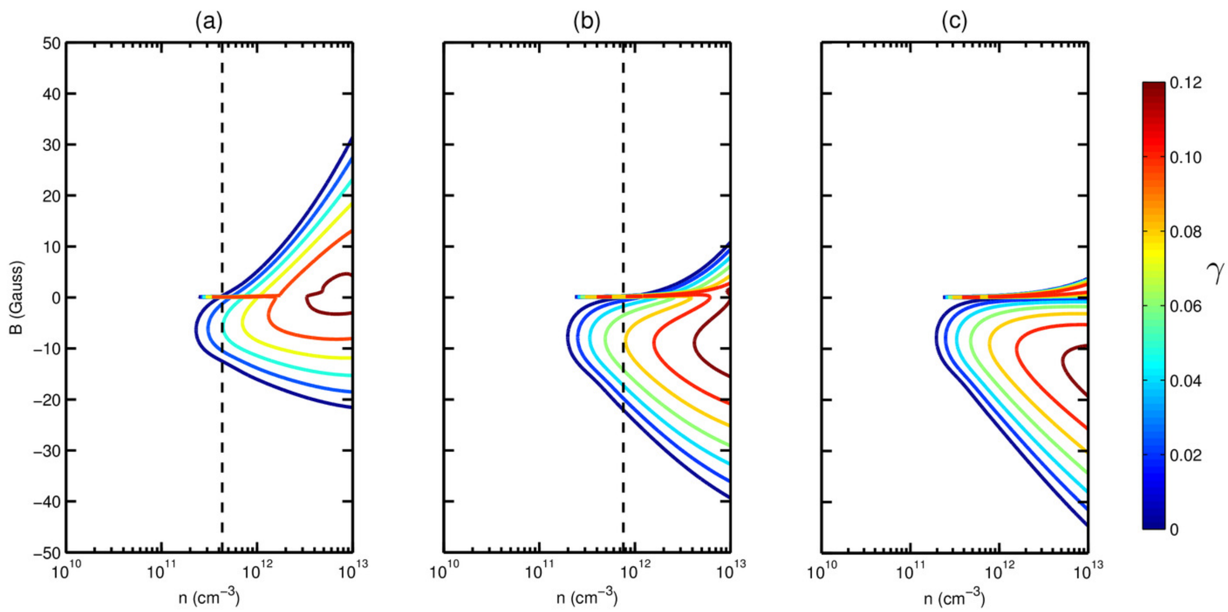

Figure 3.5: Contours of normalized growth rate γ as a function of density and applied magnetic field for the case with (a) $P_0 = 10^{-5}$ torr, (b) $P_0 = 10^{-6}$ torr and (c) no neutrals. The dashed vertical line represents the density at these neutral pressures above which the flow becomes hydrodynamically unstable due to a decrease in viscosity and increased shear caused by neutral drag.

at which the shear caused by neutral drag counter-acting viscous transport becomes great enough to drive a hydrodynamic instability. As the amount of neutrals are decreased this threshold density becomes larger, because less shear is caused by neutrals. In the case when there are no neutrals present (plot (c) in Fig. 3.5), there is no hydrodynamic instability and larger MRI growth rates can be reached by increasing the density (lowering the viscosity).

3.3 Prospects for exciting the MRI with plasma Couette flow

The stability analysis above indicates that at reasonably achievable densities and neutral fills, the MRI could be excited by plasma Couette flow. However, there are some notable issues with the current state of edge-drive plasma Couette flows that must be addressed.

First, the base flow used in the analysis ($V_1 = 10$ km/s and $V_2 = 2.5$ km/s) is quite optimistic given previously achieved flow profiles. In PCX, the flow drive at the inner boundary has been difficult to optimize due to the small size of the cathodes placed in this region. Pushing these cathodes to higher currents has led to catastrophic failures that often require arduous vacuum breaks to fix. The maximum speed achieved in helium on PCX is roughly 12 km/s, but this was reached at the outer boundary using larger, more robust cathodes. In the PCX upgrade (for details see Appendix A), design choices were made to allow for a larger center stack assembly that could accommodate larger cathodes. Alternatively, the BRB offers a larger system that could also accommodate a center stack assembly.

Secondly, Couette flow profiles in PCX have been driven in a fully unmagnetized plasma only, where no applied magnetic field is present. Applying the weak field necessary for the MRI can be easily done with a set of Helmholtz coils, but the effects on the equilibrium flow are uncertain. Optimization of the cathode placement in the steep gradient cusp region showed that the local magnetic field strength at the electrode location is critical to driving flow. In a region with too large of a field, the cross-field impedance can prevent breakdown or severely limit the overall current drawn. Conversely, if the electrodes are placed in too weak of a field, a strong torque cannot be driven. By applying a background field, the geometry of the cusp is altered significantly in the optimized electrode region, requiring alternative positioning. In order to maximize the flow with a background field, careful work would be required to optimize at every field strength of interest.

Finally, the parameter space required to excite the MRI without additional hydrodynamic instabilities is quite narrow. This is highlighted quite clearly in Figs. 3.4 & 3.5, where the range of plasma densities that result in positive MRI growth is smaller for higher neutral fill pressures. For helium discharges in particular, which are preferred for the high flow speed, operating at neutral pressures below 10^{-5} torr has not been successful for the current generation of multi-cusp devices at WiPPL. This means that a very exact plasma density is required to assure that potential MRI observations are not muddled by hydrodynamic instabilities. Additionally, this study has purposely neglected parasitic boundary layer instabilities (Ekman and Hartmann) that would also be impacted by the lower viscosity required.

Driving strong centrally peaked flows and optimizing edge-drive in the presence of applied magnetic fields are both problems that can be addressed with optimization of the experiment. However, the increased shear and subsequent excitement of parasitic hydrodynamic instabilities is an inherent feature of edge-driven Taylor-Couette flow. This is well captured by the momentum diffusion length parameter, which highlights the trade off between viscous coupling and neutral momentum loss. In order to decrease the effects of neutral drag, more viscosity is required, which can damp out any instabilities. On the other hand, if viscosity is lowered, neutral drag can be very strong at the neutral pressures required for operating multi-cusp devices. In chapter 4, I will present an alternative flow drive that no longer relies on viscous momentum coupling, removing the effect of increased flow shear by neutral collisions.

3.4 Summary

In summary, we preformed a global stability analysis for the MRI specific to PCX plasmas. For the first time, we have included both the Hall effect and charge-exchange collisions with neutral particles. The Hall term creates a preferential alignment for positive growth, where the magnetic field and flow angular momentum must be anti-parallel to excite the MRI. The Hall term also expands the range of magnetic field strengths that can excite the MRI, which can be helpful for experimental considerations. Neutral charge-exchange collisions complicate the MRI parameter space, frequently driving hydrodynamic instabilities that would inhibit study of the MRI.

In fast flowing, hot helium plasmas on PCX, the required density and neutral pressure for exciting the MRI and avoiding hydrodynamic instabilities is tantalizingly close to the the range available in the experiment. However, the input flows have not yet been achieved on PCX in the presence of a weak applied field. While theoretically possible, work must be done to address the physical difficulties associated with driving fast flows at the inner boundary. Additionally, the work presented here neglects boundary effects that could introduce complications that have already been observed in liquid metal MRI experiments.

In order to excite the MRI in edge-driven Taylor-Couette flow both the drive mechanism and the momentum transport must be improved upon. This is still an active area of research and a viable path for studying the MRI in a laboratory plasma. As an alternative, I will present a different drive mechanism that simultaneously address both of these hurdles in chapter 4.

Chapter 4

Volumetric Flow Drive

Volumetric flow drive (VFD) is an alternative flow scheme to the Taylor-Couette edge drive shown in chapter 3. By design, VFD does not rely on momentum transport to drive high Mach number flows and naturally leads to centrally-peaked profiles. The basic principle is to apply a weak magnetic field to the entire plasma volume, that only marginally magnetizes the ions, and then to drive large cross-field currents from emissive cathodes. The resulting $\mathbf{J} \times \mathbf{B}$ torque is applied to the entire volume, rather than the edges. If the applied magnetic field is uniform, the expected flow profile will follow the cross-field current density profile (assuming no axial variation in the current). For cylindrical geometry $J_r \propto 1/r$, therefore the expected flow profile will also be $\propto 1/r$ in the inviscid limit.

Volumetric flow drive has been considered as a drive mechanism for liquid metal MRI experiments [68, 73]. Relaxation method solvers show that the flow profile is indeed $\propto 1/r$ in cylindrical geometry given that the boundary Hartmann layers remain sufficiently small compared to the channel width [74]. Cross-field flow drive has been used in helicon plasma experiments [75] as well as in Hall thrusters, but in these applications the applied field is quite strong and dominates the flow.

In this chapter, I will discuss volumetric flow drive and experimental results from two different VFD geometries. First I will give a description of VFD and discuss the various limits in which WiPPL plasma operate. Then I will present the results of VFD experiments carried out on the BRB, where centrally peaked flow is accompanied by massive magnetic

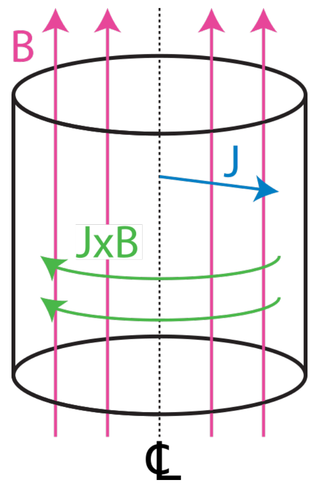

Figure 4.1: A simple diagram showing volumetric flow drive in a cylindrical volume. The Lorentz force imparted on the plasma is the result of an injected current forced across a uniform applied magnetic field.

field amplification. Using the BRB data, I will use a simple local dispersion relation to determine what is needed to excite the MRI with this flow. Then, I will present the results of simulations matching the VFD configuration used on the experiment that highlight the importance of the Hall term for this equilibrium. Finally, I will end this chapter with a simple two-fluid model of the electron and ion dynamics that are behind this unique flow drive scheme.

4.1 Configurations and Description

The simple configuration for volumetric flow drive is shown in Fig. 4.1. A radial current is driven by applying a large bias between emissive cathodes located at the outer edge of the volume and anodes placed on axis. This radial current flows across a uniform, externally applied magnetic field. The perpendicular arrangement of current and magnetic field drives a Lorentz force torque on the plasma across the entire profile. In the inviscid MHD limit with no gradients, the radial equilibrium momentum balance and Ohm's law

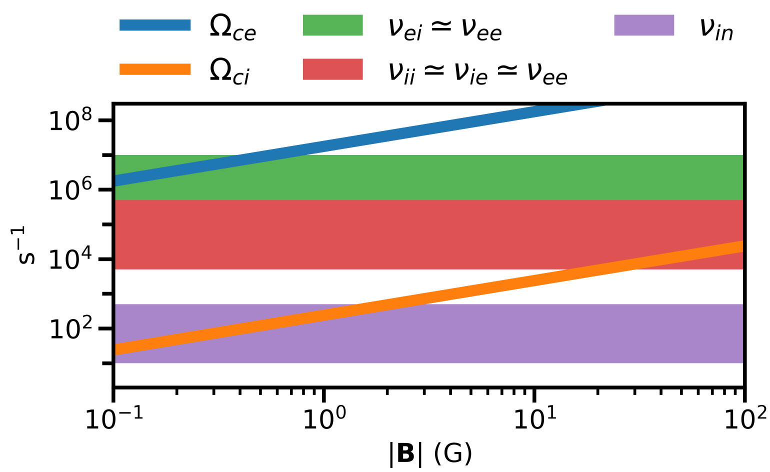

Figure 4.2: Typical collision frequencies for an argon BRB/PCX plasma along with cyclotron frequencies for both electrons and singly-charged argon ions. The ranges are set by the input ranges of: $T_e = 2{-}5$ eV, $T_i = 0.5{-}1$ eV, $n = 2{-}8{\times}10^{17}$ m^{-3}, $p_0 = 2{-}4{\times}10^{-5}$ torr. Most argon plasmas on BRB or PCX fall in these ranges.

equations describe this drive.

$$0 = -\frac{J_r B_z}{n m_i} - \nu_{in} V_\phi \tag{4.1}$$

$$E_r = \eta J_r - V_\phi B_z \tag{4.2}$$

where η is the plasma resistivity and can be related to the ion-electron collision frequency using the Spitzer definition, $\eta \equiv \frac{m_i \nu_{ie}}{ne^2}$, and ν_{in} is the ion-neutral collision frequency. Combining these equations, the resulting flow is

$$V_\phi = -\frac{E_r}{B_z}\left[1 + \frac{\nu_{ie}\nu_{in}}{\Omega_{ci}^2}\right]^{-1} \tag{4.3}$$

which is the $\mathbf{E} \times \mathbf{B}$ particle drift modified by collisions. This expression clearly shows the relationship of the drive on the magnetization of the ions. As $\nu_{ie}\nu_{in}/\Omega_{ci}^2$ gets larger than 1, collisions will begin dominating the ion dynamics and the flow will be reduced significantly. On the other hand, as B becomes large, the flow for a given electric field will

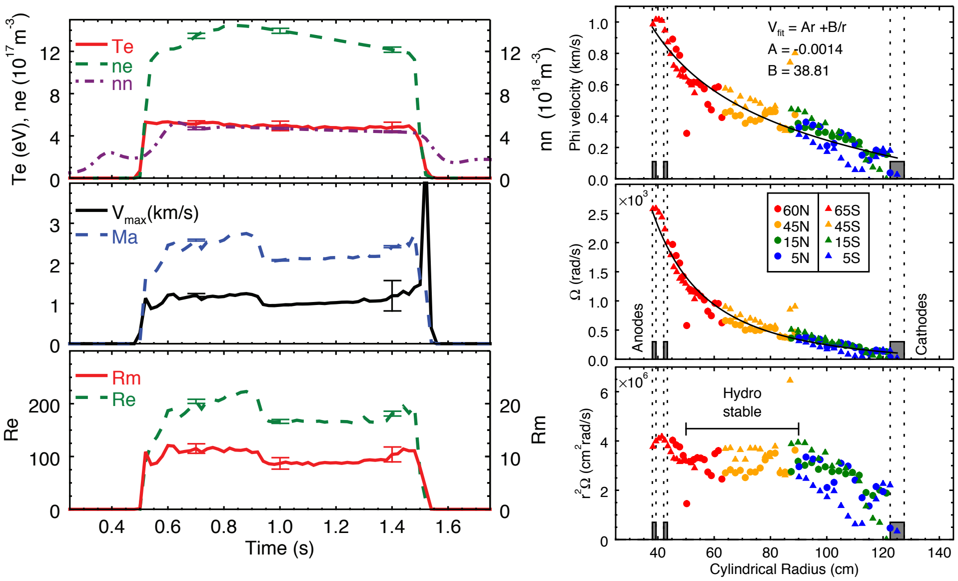

Figure 4.3: Panel of results from the previous flow experiments on the BRB. High Alfvén Mach number flows were driven in both argon and helium. Image credit: [30]

be reduced. Therefore, a fine balance of magnetization and field strength is required to maximize flow speeds.

The relative collision frequencies and cyclotron frequencies for a typical argon plasma produced on the BRB are shown in Fig. 4.2. For most of the range of magnetic fields shown in this plot, ions are unmagnetized (i.e. their collision frequency is greater than their cyclotron frequency). This indicates that the Lorentz force driving the flow will be reduced by collisional effects. The collision factor from Eq. 4.3 will be equal to one around 10 G at the parameters used to make this plot. So for applied fields less than approximately 10 G the drive will be significantly modified by collisions. However, a lower field does make for a larger flow for a given applied electric field, so these two features can counteract each other within a certain range of applied magnetic field.

Previous work on the BRB has shown that VFD does produce strong centrally peaked flows with the correct applied magnetic field strength (see Fig. 4.3) [30]. In argon plasmas strong flow is produced with applied fields $\lesssim 2$ G, while in helium the field must be $\lesssim 0.5$ G. In both argon and helium plasmas the peak flow speed had a Alfvén Mach

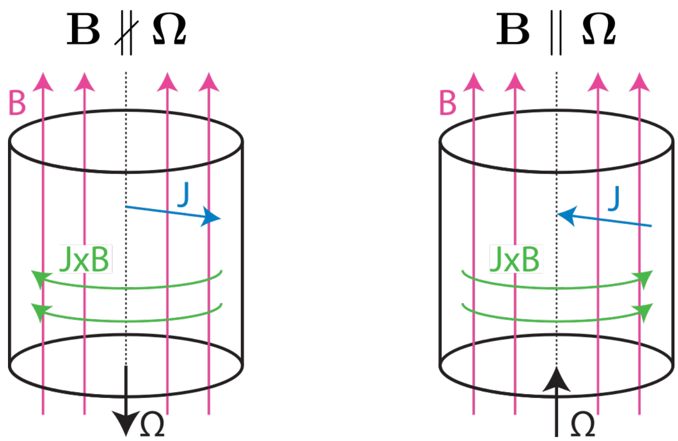

Figure 4.4: Simple diagrams of VFD in a cylindrical geometry. Left: cross-field current is directed radially outward, which leads to a flow rotation vector that is antiparallel to the applied magnetic field. Right: inward directed current leads to an aligned rotation vector and magnetic field.

number greater than 1 and for helium plasmas, R_m and R_e were quite high (100 and 200, respectively).

While these flow experiments established that VFD is possible with relatively weak magnetic fields, no flow instability was directly observed and no magnetic field measurements were made. Additionally, the flow measurements were not made on a cylindrical radius chord, rather taking advantage of higher latitude ports to reach smaller cylindrical radii. This probe placement makes the assumption of axial uniformity, which is uncertain due to the polar placement of anodes. The work presented here is the natural extension of these initial flow observations that seeks to answer some of these open questions and oversights.

4.1.1 Prospects for observing MRI in VFD

An major motivation of volumetric flow drive experiments was to produce flow that could be unstable to the MRI, taking advantage of the lack of profile effects from neutral collisions. The simple model of VFD certainly meets the ideal-MRI criteria of having high

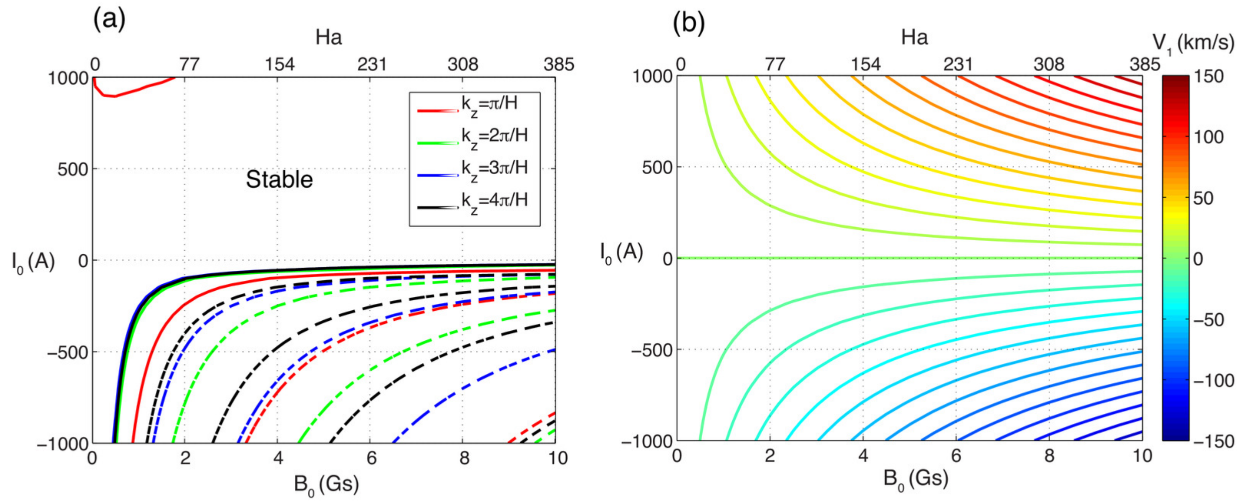

Figure 4.5: MRI regions in electrically driven flow for modes with different axial wavenumbers k_z. Dashed lines of the same colour denote stability boundaries for modes with the same k_z but different radial mode numbers. (b) toroidal velocity at the inner wall. Plasma parameters are listed in the text. Negative sign of I_0 corresponds to current flowing from the inner to outer wall.

Alfvén Mach number flows that are centrally peaked. However, as discussed in Chapter 3, other factors come into play including dissipation (resistive or viscous), neutral drag and the Hall term. Dissipation and neutral drag are overcome by driving flow in hot, dense, highly-ionized plasmas. The previous VFD experiments on BRB produced flows that had large R_m and R_e, indicating that the multi-cusp confined plasmas were hot and dense enough for instabilities to grow without too much damping.

The Hall term has a strong impact on most WiPPL plasmas. Typically, the importance of this term in extended Ohm's law is ordered by the ion inertial length, which at densities in the $10^{17} - 10^{18}$ m^{-3} range is on the order of 1 m. Since most characteristic length scales (like the flow shear from the previous VFD experiments) in WiPPL plasmas are typically order 10-100 cm, the Hall term will be very important in any potential instabilities and equilibria.

As discussed in Chapter 3, the MRI in the Hall regime only has positive growth rates when the rotation vector and magnetic field are antiparallel. Due to the cross-product term, the relative orientation of the rotation vector and the magnetic field can only be altered by changing the cross-field current direction. Experimentally, this corresponds to the placement of the emissive cathodes with respect to the anodes, as shown in Fig 4.4. Cathodes placed on the outer boundary of the volume will drive radially outward current ($\mathbf{B} \nparallel \mathbf{\Omega}$), while cathodes placed on axis will drive inward current ($\mathbf{B} \parallel \mathbf{\Omega}$). Therefore, for observation of the MRI in the Hall regime using VFD, the electron current-injecting cathodes must be placed on the outer radial boundary of the plasma.

Using the same stability analysis outlined in Ch. 3, VFD has been shown to drive the Hall MRI for cases with radially outward current drive [26]. Helium plasmas with $n = 10^{18}\,\mathrm{m}^{-3}$, $T_e = 12\,\mathrm{eV}$, $P_0 = 10^{-5}$ torr and a $1/r$ profile lead to multiple Hall MRI modes with modest total injected currents of approximately 100 A. The onset of several MRI modes and the peak flow speed are shown as a function of applied cross-field current and magnetic field in Fig. 4.5.

4.2 Volumetric flow drive experiments on BRB

The electrode configuration for the volumetric flow drive experiments presented in this work is shown in Fig. 4.6. A set of six LaB_6 cathodes arranged around the equator of the vessel inject roughly 300 A of current over the course of a 1 s discharge. Large, molybdenum ring anodes are inserted just past the cusp field at both poles to complete the bias circuit. These anodes have been custom designed to fit between the two smallest rings near the poles of the BRB device. Their position can be adjusted via sliding o-ring seals. The area of a single ring anode is approximately 530 cm^2, which corresponds to roughly eight of the commonly used BRB anodes. The large surface area of the ring anodes helps to mitigate the plasma ‘crashing’ phenomenon that has been observed in high current discharges with reduced anode area on BRB [31].

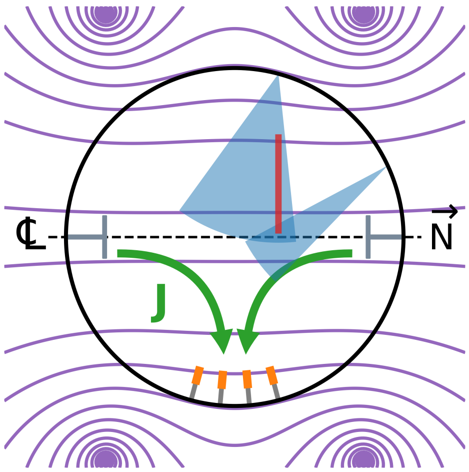

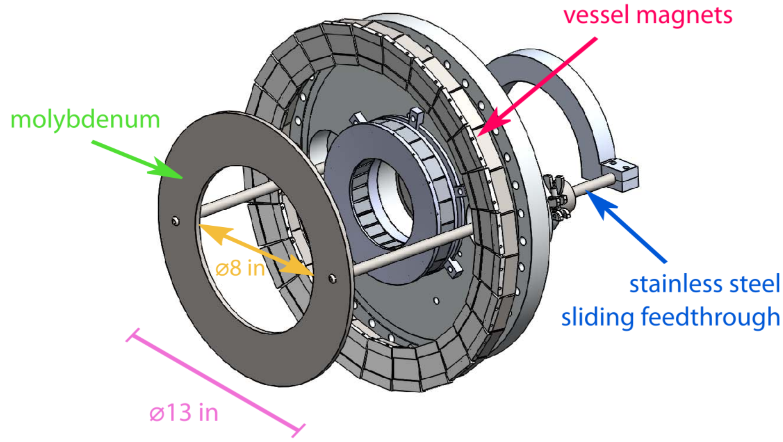

Figure 4.6: Left: Diagram showing the anode and cathode locations as well as the sweep probe area of coverage. Cylindrical radial scans were performed with a combination Mach/Triple probe along the red line. Right: CAD image of the ring anodes that are inserted just past the cusp field at either pole.

A 3-axis 15 position Hall probe array was swept out over the poloidal wedge areas shown in Fig. 4.6 over the course of roughly 100 shots with overlapping positions to verify shot-to-shot reproducibility. Throughout the course of the scan, the neutral pressure and cathode currents were carefully monitored to assure that controlled parameters were kept constant. In addition to the poloidal sweep scan of the Hall probe, a cylindrical radial scan was taken at an axial location approximately 40 cm from the equator (indicated by the red line in Fig. 4.6) with a single point combination Mach/triple probe. The Mach probe faces record both poloidal and toroidal flow and were calibrated using the method described in Chapter 2. In order to reduce triple probe errors, the bias of the individual tips was permuted roughly every 10-20 shots. The rest of this section will describe the results of this scan.

As expected, the configuration to drive volumetric flow on the BRB produced fast, centrally peaked flows. The measured cylindrical radial profiles of the flow are shown in Fig. 4.7. Compared to previous VFD experiments on BRB [30], this profile has a very

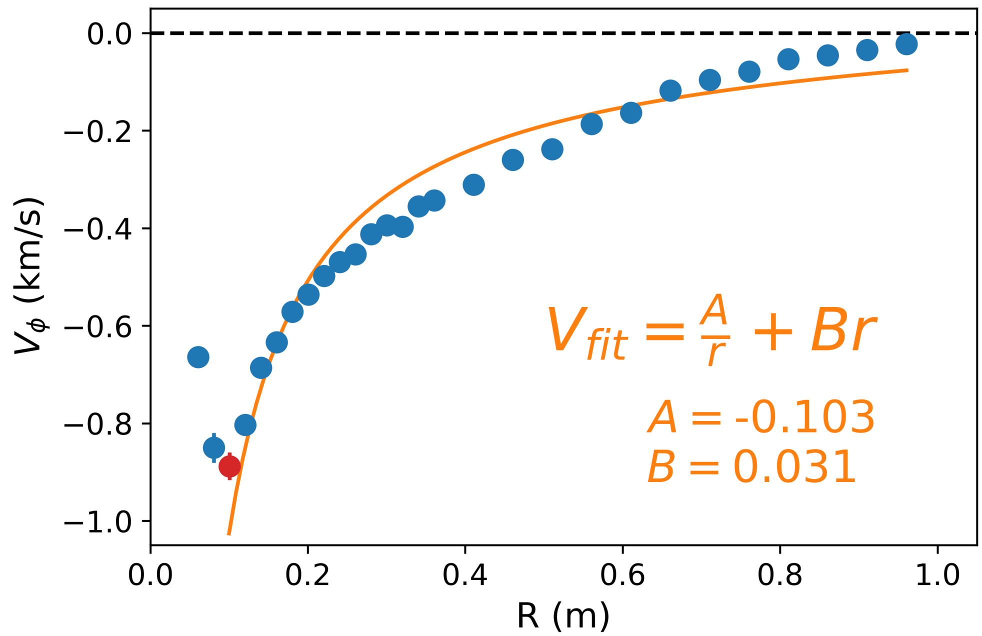

Figure 4.7: Toroidal flow profile measured along the cylindrical radius of the BRB. The flow is very strongly centrally peaked and fits well to a Couette profile.

Case	I_{HH} (A)	B_z^0 (G)	B_z^{eq} (G)	V_ϕ^{pk} (m/s)	n (10^{17} m^{-3})	M	M_A	β
1	0	+0.4N	+9.0N	-1000	2.5	0.36	0.16	0.5
2	1.42	+0.1N	+6.8N	-400	4.4	0.15	0.13	2.1
3	2.84	-0.6S	-4.6S	150	5	0.05	0.06	4.3
4	4.26	-1.6S	-9.4S	350	4.1	0.12	0.08	1.3

Table 4.1: Table of the four different applied field cases used in the BRB VFD experiments. The magnetic field (columns 1 & 2) points towards the north pole when positive. All values are calculated at the radial location of the peak flow at $t = 0.8$ s when the discharge has reached a steady-state. For argon plasmas, where the heavy ions do not reach as high speeds as helium, case 1 shows very strong flow, despite the relatively weak Alfvén Mach number.

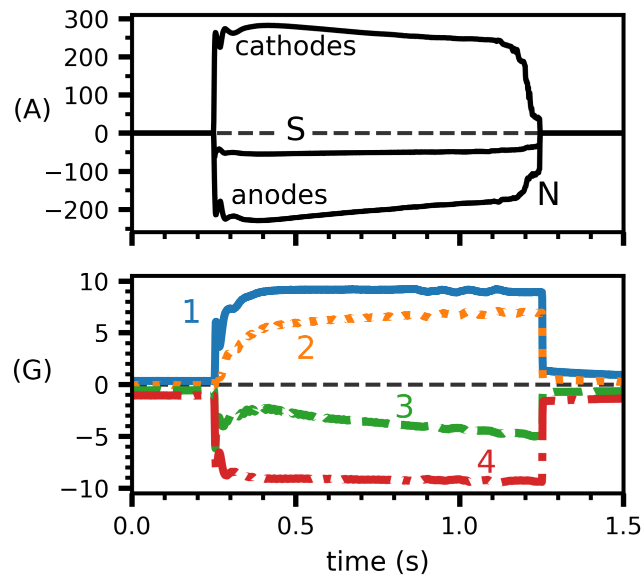

Figure 4.8: Time traces of VFD discharges on BRB. Top: The average electrode currents during the scan. The north polar anode draws much more current than the south pole mostly due to fine placement in the cusp field and, potentially, different surface coatings. Bottom: B_z for the four different initial field cases used in the scan measured on axis of the device.

pronounced peak near the axis. This is the result of the new uniform, axisymmetric ring anodes as opposed to discrete, radially inserted anodes near the poles.

For four different applied magnetic field cases (summarized in Table 4.1), a massive amplification of the initial magnetic field was observed. Figure 4.8 shows the average time trace of electrode currents and axial ($\hat{z}$) magnetic field on axis for the four cases. For an injected current of roughly 300 A, the magnetic field was amplified by up to a factor of 20. The amplification also is aligned with the initial field, such that reversing the initial field direction simply leads to a reversed amplification. Additionally, the final magnitude of the field scales with the magnitude of the initial field, such that a stronger initial field will yield a stronger amplified field. The ratio of initial to final fields, however, does not show a clear scaling.

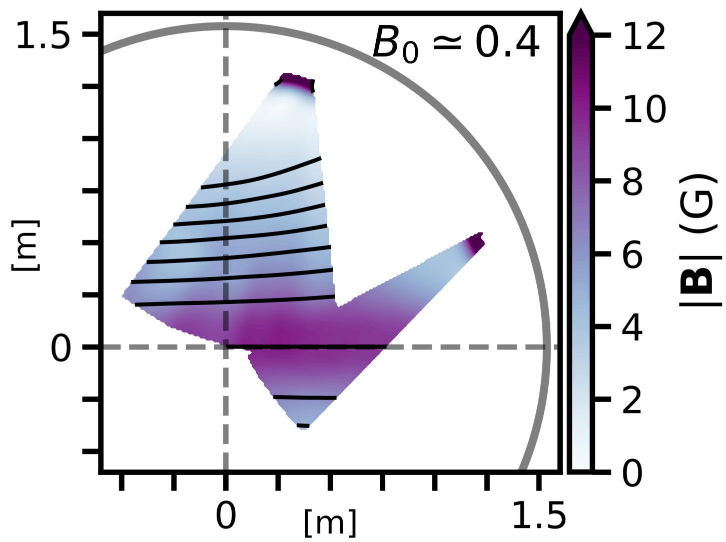

Figure 4.9: A poloidal sweep map of the magnetic field strength, $|\mathbf{B}|$, with field lines. This map is from case 1 in Table 4.1 and was taken late in time when the steady state of the discharge was reached. Within the shot-to-shot variations the magnetic field amplification is uniform axially (horizontal in this plot).

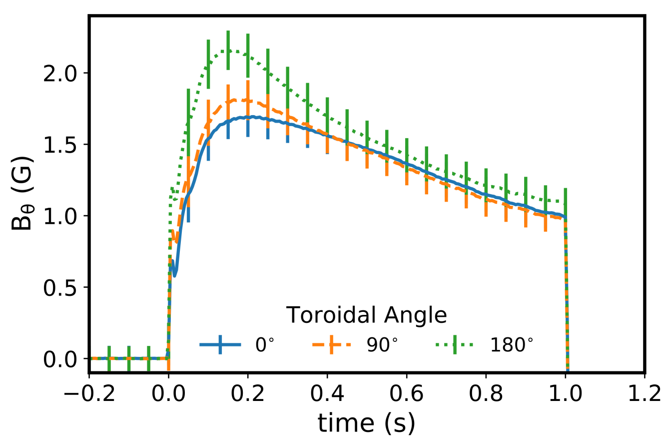

Figure 4.10: Three different 3-axis Hall probes mounted to the inside wall of the BRB vessel (out of the plasma) are located in the same ring (longitude) and spaced roughly 90° degrees apart toroidally (latitude). Within measurement error, the three probes record the same field during a BRB VFD discharge, indicating that the equilibrium is axisymmetric.

Figure 4.9 shows a poloidal sweep map of the magnetic field. Within shot-to-shot error the magnetic field amplification is both centrally peaked and uniform in the axial direction[1]. This map was taken at a late in time point during the discharge where there is very little temporal variation in the structure or magnitude of magnetic field. Toroidally separated Hall probes placed out of the plasma on the inside of the vessel [40] show that the magnetic field structure is also axisymmetric within measurement error (see Fig. 4.10). Both of these measurements effectively reduce the system to a 1D equilibrium with values largely uniform toroidally and axial, only varying in radius.

Along the radial chord scan, Figure 4.11 shows profiles of the flow, density and magnetic field. The direction of the toroidal flow is consistent with the simple $\mathbf{J} \times \mathbf{B}$ drive that we would expect, changing sign when the magnetic field direction is flipped. The centrally peaked flow reflects the expectations of volumetric flow drive, however, the amplified field plays a crucial role in driving the flow. Near the center of the device, the stronger field partially magnetizes the ions, which would not flow otherwise. The momentum imparted on the ions near the center then viscously couples outwards, similar to the edge driven flows from previous experiments.

Notably, there is an asymmetry to the different flow directions. The highest peak flow speed was driven in case 1 (see Table 4.1), when there was no externally applied field, leaving the small residual dipole field from the cusp magnets. When a similar strength field was applied in the opposite direction, the flow was oppositely directed, but significantly smaller in its peaked magnitude. The most likely explanation of this asymmetry lies in the detailed geometry of the cusp and the location of null points as an external field is applied. In future experiments, a high-resolution magnetic field measurement of the cusp region would hopefully elucidate the current paths near the edge of the plasma.

[1] The small structure in the z direction is caused by the slight misalignment of the probe as it is swept over the poloidal wedge and is non-existent within this measurement error.

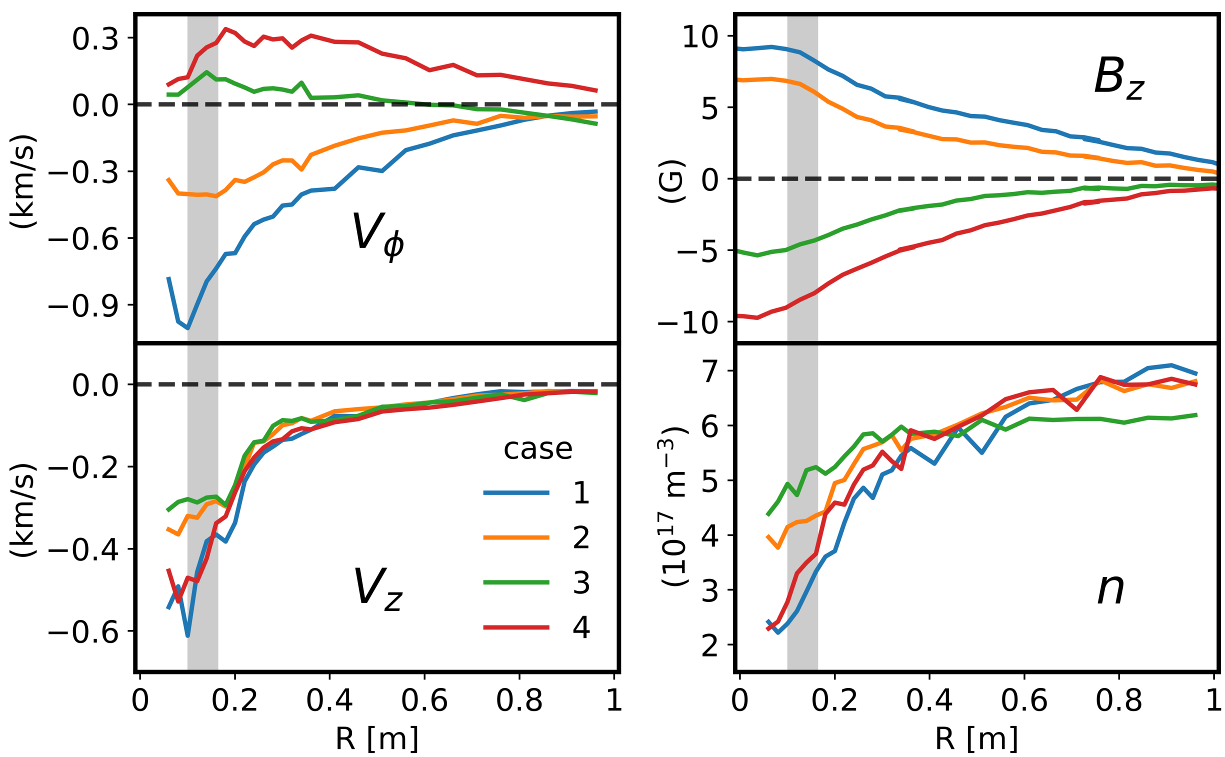

Figure 4.11: Radial profiles of the toroidal velocity (top left), magnetic field (top right), axial velocity (bottom left) and density (bottom right) for the four different cases outlined in Table 4.1. The absolute velocities are calculated using $C_s = 2.8$ km/s which corresponds to an electron temperature, $T_e = 2.3$ eV, and an ion temperature of $T_i \approx 1$ eV. The profile of electron temperature from the triple probe is not shown, because it is uniform within error. The ion temperature is an estimate based on Fabry-Pérot measurements of similar argon discharges on BRB. The gray shaded region in each plot shows the radial extent of the ring anode.

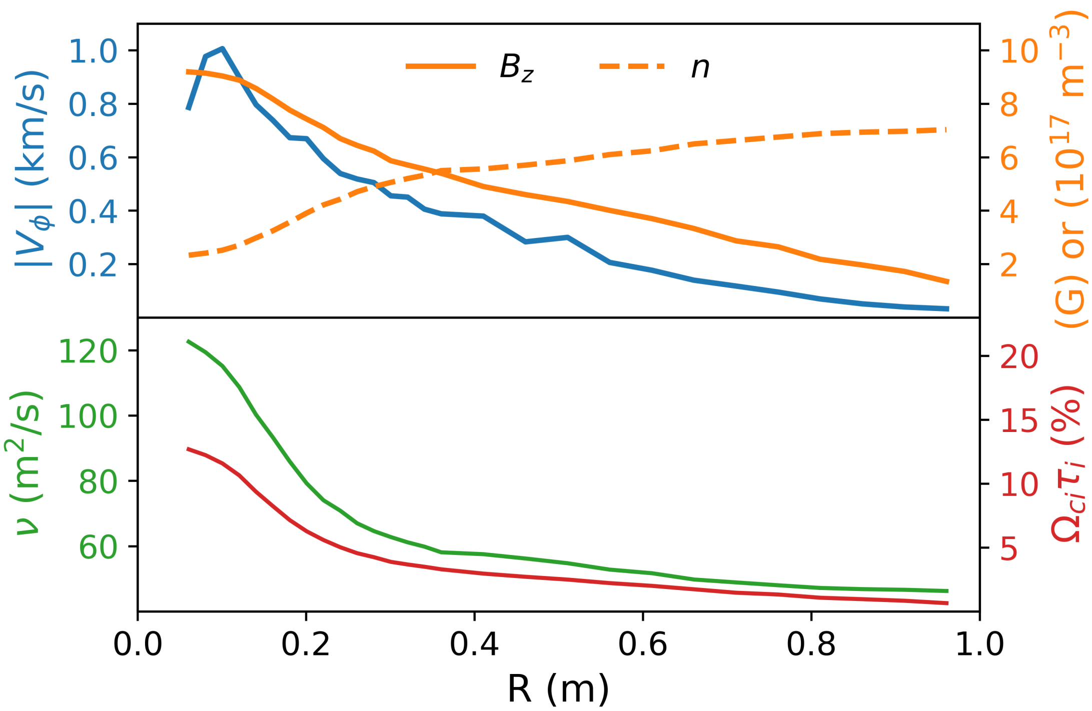

Figure 4.12: Profiles corresponding to case 1 in Table 4.1. (Top) shows the magnitude of toroidal velocity, the magnetic field and the density profiles. (Bottom) shows the kinematic viscosity and the percent magnetization using these profiles. As in Fig. 4.11, $T_e = 2.3$ eV and $T_i = 1$ eV.

In addition to the massive field amplification and centrally peaked flow, a hollow density profile was observed in these experiments. As shown in Figure 4.11, the density gradient magnitude changes with different levels of field amplification. More density is removed near the center when a larger field is present. That is to say that this system is acting diamagnetically, which is typical for simple plasma equilibria. As a result of the lower density on axis, the viscosity is quite high at the peak flow location due to the decreased density. For case 1, Figure 4.12 shows the profile of Braginskii viscosity calculated using the density and magnetic field profiles with a fixed $T_i = 1$ eV.

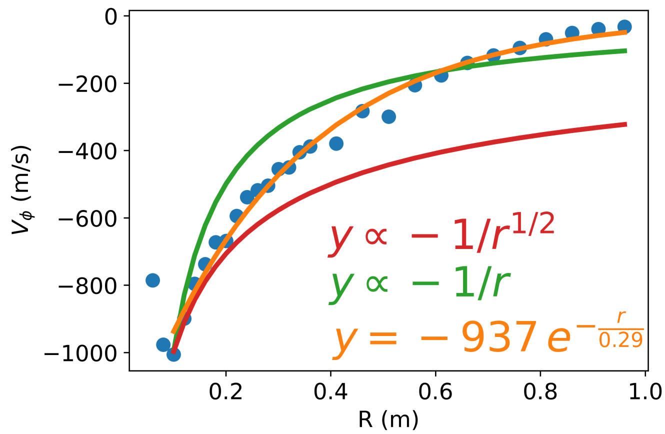

Figure 4.13: Simple fit to the BRB VFD radial flow profile. For comparison, Keplerian flow, $\propto r^{-1/2}$, and expected VFD flow, $\propto 1/r$, profiles are shown. The data is fit only in the region beyond the peak flow, neglecting the solid-body rotation near the axis ($R \simeq 0 - 0.1$ m).

4.2.1 Stability of VFD to the MRI

While no instabilities were observed in the VFD experiments shown above, it is instructive to consider what factors acted to stabilize the MRI. Under ideal MHD conditions, the MRI requires [4]

$$k_\parallel^2 V_A^2 \leq -\frac{\partial \Omega^2}{\partial \ln r} \tag{4.4}$$

where $\Omega = V_\phi/r$ and $k_\parallel$ is the wavenumber of the fastest growing linear mode. Additionally, in order to distinguish the MRI from a fluid instability (such as a simple interchange-like mode), it is necessary to have a profile with radially increasing angular momentum. This requirement is described by the Rayleigh instability criterion [69],

$$\frac{\partial}{\partial r}(r^2\Omega) \geq 0 \tag{4.5}$$

Both of these requirements are very simple to study using the linear profiles in Fig. 4.11. For the toroidal flow profile, it will be useful to perform a simple ad hoc fit to an analytical function to take radial derivatives without numerical effects. Taking a decaying exponential function as a model, the fit is shown in Fig. 4.13. As a comparison, $1/r$ and Keplerian profiles are plotted as well to highlight that the measured flow has more shear than a Keplerian profile and, over a region, more than $1/r$ as well.

A $1/r$ profile is the marginally stable case for the Rayleigh criterion, therefore this fit suggests that for the region where it is steeper than $1/r$, hydrodynamic instabilities would be expected. Experimentally, this flow was extremely stable indicating no such instabilities, but this is likely due to the lack of non-ideal effects, such as dissipation and boundary conditions, in this analysis. To test for the ideal-MRI criterion, a minimum wavenumber must be chosen for the BRB. Typically this is taken to be the wavenumber corresponding to the longest half-wavelength that can fit in the device. Since the axial extent of the experiment varies with radius due to the spherical geometry, we can take this minimum $k_\parallel$ for BRB to be a function of radius,

$$k_\parallel^{\mathrm{min}} = \frac{\pi}{2\sqrt{R_{\mathrm{plasma}}^2 - r^2}} \tag{4.6}$$

where $R_{\mathrm{plasma}} \simeq 1.5$ m. Figure 4.14 compares this minimum $k_\parallel$ to the $k_\parallel$ set in Eq. 4.4. In order to match the ideal-MRI criterion, the minimum $k_\parallel$ for BRB, Eq. 4.6, must be less than the $k_\parallel$ set by the MRI criteria. Additionally, it would be ideal to avoid flows that have enough shear to drive hydrodynamic instabilities.

In Fig. 4.14, the flow is hydrodynamically unstable according to Eq. 4.5 beyond $R \simeq 0.3$ m. In the region inside of $R \simeq 0.3$ m, the flow is unstable to the ideal MRI condition and meets the Rayleigh stability criterion. It is noteworthy that the amplified magnetic field does not stabilize the MRI with this flow profile. However, no instabilities were observed experimentally presumably due to dissipation as well as ion-neutral collisions. The degree to which these various effects stabilize the MRI can be addressed by a more detailed analysis.

In order to verify that the MRI is being stabilized by dissipation, it is necessary to consider a non-ideal stability condition. Rather than repeating the global stability analysis from Chapter 3, I will employ a simpler WKB method. The dispersion relation for the

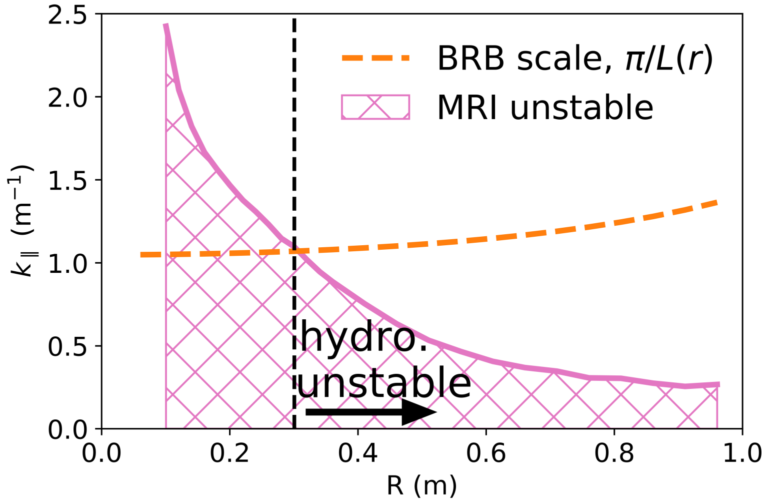

Figure 4.14: Radial profile of ideal-MRI stability on the BRB. The hashed region indicates the wavenumbers that are unstable to the ideal-MRI using the V_ϕ and B_z profiles from the BRB VFD experiment. The vertical dashed line indicates the region of the flow profile that has enough shear to excite hydrodynamic instabilities. A small region between the peak flow and $R \simeq 0.3$ is unstable to the ideal-MRI for wavenumbers that fit the experiment scale.

MRI that includes dissipation, neutral collisions and the Hall effect is,

$$0 = \left[(\gamma + \eta k^2)(\gamma + \nu k^2 + \nu_{i0}) + (k_z V_A)^2\right]^2 \frac{k^2}{k_z^2} + \kappa^2(\gamma + \eta k^2)^2 + \frac{\partial \Omega^2}{\partial \ln r}(k_z V_A)^2$$
$$+ C_H \Omega \frac{k^2}{k_z^2}\left[\left((\gamma + \nu k^2 + \nu_{i0})^2 + \frac{k_z^2}{k^2}\kappa^2\right)\left(\frac{\partial \Omega}{\partial \ln r} + C_H \Omega \frac{k^2}{k_z^2}\right) + k_z^2 V_A^2 \left(4\Omega + \frac{\partial \Omega}{\partial \ln r}\right)\right] \quad (4.7)$$

where $\kappa^2 = 4\Omega^2 + \partial\Omega^2/\partial \ln r$ is the epicyclic frequency, $C_H = (k_z^2 B_0)/(\mu_0 n e \Omega)$ is the Hall parameter, η is the resistivity, ν is the viscosity, and ν_{i0} is the ion-neutral charge exchange collision frequency. In the limit that $\nu_{i0} \to 0$ and $C_H \to 0$ the simpler dissipative MRI dispersion relation from [76] is recovered. This dispersion relation is copied directly from Cami Collins's thesis, which provides an excellent overview of its derivation that I will not include here [27].

In addition to the MRI dispersion, it is important to determine the local stability to hydrodynamic modes. In the presence of viscosity and neutrals the local condition for

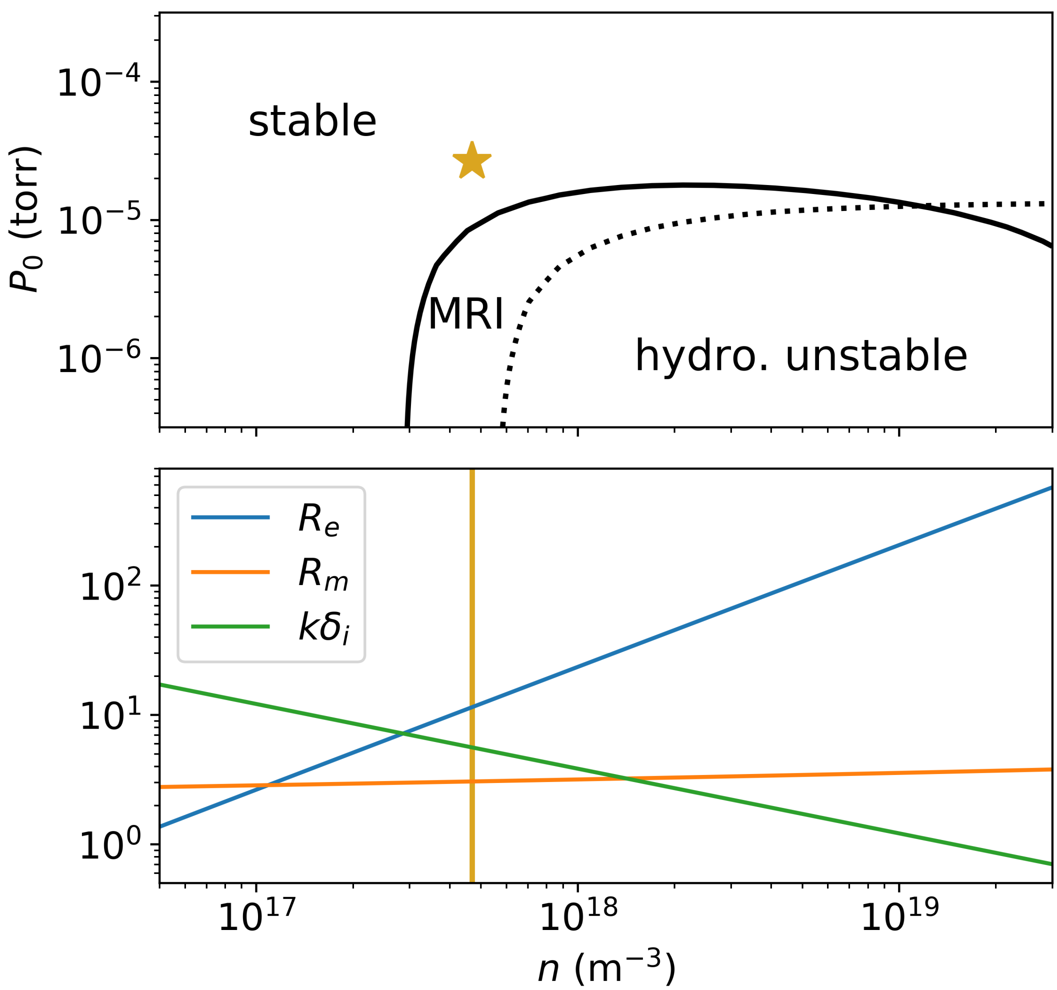

Figure 4.15: Top: n-P_0 phase space showing stability curves for the onset of hydrodynamic instability and the MRI. The gold star represents the parameters of the experiment on the BRB. This space was mapped using parameters from the BRB linear profiles at $R = 0.26$ m. Bottom: Scaling of R_e, R_m and $k\delta_i$ for the given flow versus density. The vertical gold line marks the experimental density.

hydrodynamic stability is [27],

$$\frac{1}{r|\Omega|}\frac{\partial}{\partial r}(r^2\Omega) \geq -\frac{k^2}{2k_z^2\Omega^2}\left[\nu^2k^4 + \nu_{i0}^2\left(1 + 2k^2\frac{\nu}{\nu_{i0}}\right)\right] \tag{4.8}$$

where the left hand side of this expression is the dimensionless vorticity of the flow. In the limit of no dissipation, this expression exactly reduces to Rayleigh's criterion.

Similar to the parameter phase space plot shown in Chap. 3 (Fig. 3.4), we can construct a parameter phase space map for local stability of the V_ϕ and B_z profiles from the experiment. Figure 4.15 shows this map for stability taken at $R = 0.26$ m, which is in the unstable region in the no dissipation limit. The curves in this phase space represent the stability boundaries of the local dispersion, Eq. 4.7. Regions above and to the left of the curves are stable due to viscosity and neutral charge-exchange collisions. There is a small region where the MRI is excited, but the flow remains hydrodynamically stable. With a low enough viscosity, hydrodynamic instabilities are present due to the large shear in the flow profile. The bottom of the figure shows the scaling of R_e, R_m and $k\delta_i$ for these parameters in density with fixed T_e, T_i, and V_ϕ.

The gold star in Fig. 4.15 indicates the parameters that the experiment operated at. Neutral charge-exchange collisions play a major role in stabilizing these flows above a critical density. This simple WKB analysis suggests that at a lower neutral pressure the MRI could develop in these flows, however, for a given plasma confinement time and input power, lower neutral pressures will produce lower density plasmas. Additionally, these stability curves are calculated locally, which ignores any real profile effects that could ultimately stabilize the mode.

4.3 NIMROD Simulations of VFD

The simulation code, NIMROD (Non-Ideal Magnetohydrodynamics with Rotation, an Open Discussion) has been developed by a national team to provide a platform for simulations of MHD and extended MHD instabilities and waves in hot, dense plasmas [77].

NIMROD solves the full set of extended partial differential MHD equations using 2D finite element methods in the poloidal plane and a truncated Fourier series in the toroidal direction. The equations are evolved in time from an equilibrium using implicit or semi-implicit time stepping, allowing for stability even with large time steps. Here I will present the NIMROD configuration used for studying VFD in the BRB and outline key results from simulations.

In the simulations presented here, an isotropic viscous stress is assumed along with an isothermal equation of state for both the electrons and ions. All physics parameters in NIMROD are run at full values, so no other physics simplifications are required for the input. The full set of equations that are advanced by NIMROD in these cases are,

$$\nabla \times \mathbf{B} = \mu_0 \mathbf{J} \tag{4.9}$$

$$\nabla \cdot \mathbf{B} = 0 \tag{4.10}$$

$$\frac{\partial \mathbf{B}}{\partial t} = -\nabla \times \mathbf{E} \tag{4.11}$$

$$\mathbf{E} + \mathbf{V} \times \mathbf{B} = \eta \mathbf{J} + \frac{1}{ne}\mathbf{J} \times \mathbf{B} - \frac{1}{ne}\nabla P_e + \frac{m_e}{ne^2}\frac{\partial \mathbf{J}}{\partial t} \tag{4.12}$$

$$\frac{\partial n}{\partial t} + \mathbf{V} \cdot \nabla n = -n \nabla \cdot \mathbf{V} \tag{4.13}$$

$$\rho \left(\frac{\partial \mathbf{V}}{\partial t} + \mathbf{V} \cdot \nabla \mathbf{V} \right) = \mathbf{J} \times \mathbf{B} - \nabla P - \nabla \cdot \overleftrightarrow{\mathbf{\Pi}} \tag{4.14}$$

$$\overleftrightarrow{\mathbf{\Pi}} = -\rho\nu \left(\nabla \mathbf{V} + \nabla \mathbf{V}^T - \frac{2}{3}\overleftrightarrow{\mathbf{I}} \nabla \cdot \mathbf{V} \right) \tag{4.15}$$

The first expression is Ampére's law without displacement current, which is neglected due to the timescales encountered in MHD. This is followed by the divergence-less magnetic field condition, Faraday's Law and the extended Ohm's law. Next is the continuity equation that describes the density evolution with particle conservation. Following is the momentum balance equation with the Lorentz, pressure and viscous forces on the right hand side. The final expression is the isotropic stress tensor that describes the viscous diffusion of momentum and closes the system.

As a result of the finite-element expansion used in NIMROD, the divergence-less magnetic field condition is approximately satisfied by adding a non-physical diffusive operator to Faraday's law of induction, together with NIMROD's high-order representation. This addition means that Faraday's law takes the form,

$$\frac{\partial \mathbf{B}}{\partial t} = -\nabla \times \mathbf{E} - \kappa_B \nabla(\nabla \cdot \mathbf{B}) \tag{4.16}$$

The diffusion constant, κ_B, is set to the minimum required value to reduce any non-physical effects. In practice this constant is simply set by the grid size and spacing.

4.3.1 NIMROD setup

In order to properly simulate the spherical geometry of the BRB in NIMROD, a custom poloidal mesh was designed. The mesh extends all the way to the origin and is unstructured to avoid degeneracy issues. To accommodate the geometry, six separate mesh grids are initialized and then stitched together to form a half sphere. An outline of the stitching process is shown in Fig. 4.16.

Beyond setting up the custom spherical mesh, a method of current injection is necessary for simulating the volumetric flow drive. This is done by specifying a toroidal magnetic field, B_ϕ, along the edge of the simulation domain. By Ampére's law this is equivalent to specifying a radial current profile around the boundary. Figure 4.17 shows the current injection scheme used for these runs. The electrodes are approximated as evenly distributed current injection areas along the outside of the sphere. The anodes take up 15° of the boundary near the top and bottom and the cathodes are evenly spread over 30° near the equator. By having the current uniform over the injection areas, the boundary profile is simply a series of step functions along θ. The resulting toroidal magnetic field is plotted as function of θ in Fig. 4.17 as well. At the very beginning of the simulations, this profile is ramped up to the full value over the course of 1 ms to avoid any unwanted numerical artifacts from an instant turn on. For the rest of the simulation run, this current injection profile is held as a boundary condition.

Figure 4.17 also shows that the simulation mesh is packed near the outer boundary of the sphere. This is purposely done to improve the resolution in the areas where currents

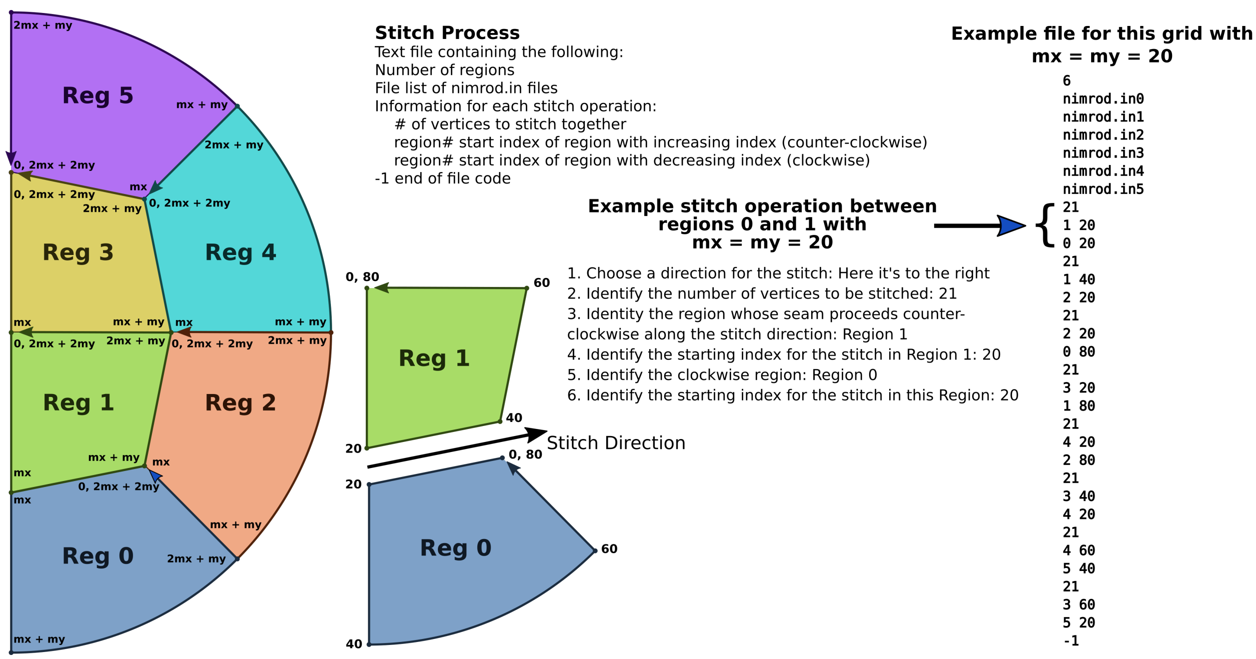

Figure 4.16: An outline of the stitching process needed for creating the mesh used for NIMROD simulations in the spherical BRB geometry. The builtin `stitch` executable in NIMROD performs the stitching, but a careful set of instructions are needed to properly connect the six regions. Image credit: Ethan Peterson [40]

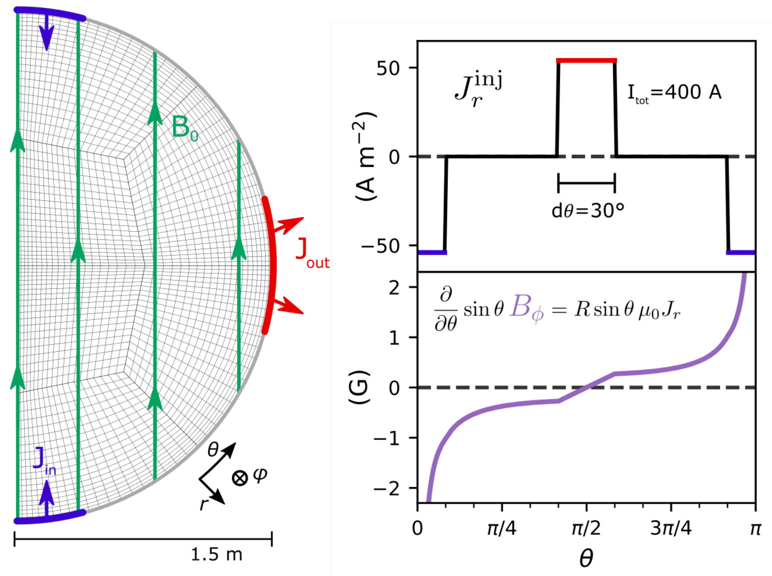

Figure 4.17: Left: the poloidal grid used for simulating the BRB showing the uniform initial field and the location of current injection areas. Upper right: the profile of current injection along the boundary. The case shown here is for a total injected current of 400 A and radially outward current. Bottom right: The resulting B_ϕ profile along the boundary for this case.

necessarily cross the uniform vertical field, allowing for better enforcement of $\nabla \cdot \mathbf{B} = 0$. Additionally, both the viscosity and resistivity are given shaping profiles as a function of spherical r that increase in these regions to avoid small boundary layers that could lead to convergence issues.

For the simulations presented in this work the physical inputs are chosen to represent the parameters where the fastest edge flow has been driven on BRB. This is not a direct one-to-one match to the argon VFD experiments, but it clearly highlights the mechanisms at play in this equilibrium. Simulations at the actual experimental parameters are very similar, but the effect is less dramatic. The used parameters are: $n = 6 \cdot 10^{17}$ m^{-3}, $T_e =$ 8 eV, $T_i = 0.5$ eV, and the initial magnetic field strength is 0.5 G. In a helium plasma, the Braginskii transport equations give $\nu = 21.3\ m^2/s$ and $\eta = 26.0\ m^2/s$ for the viscosity

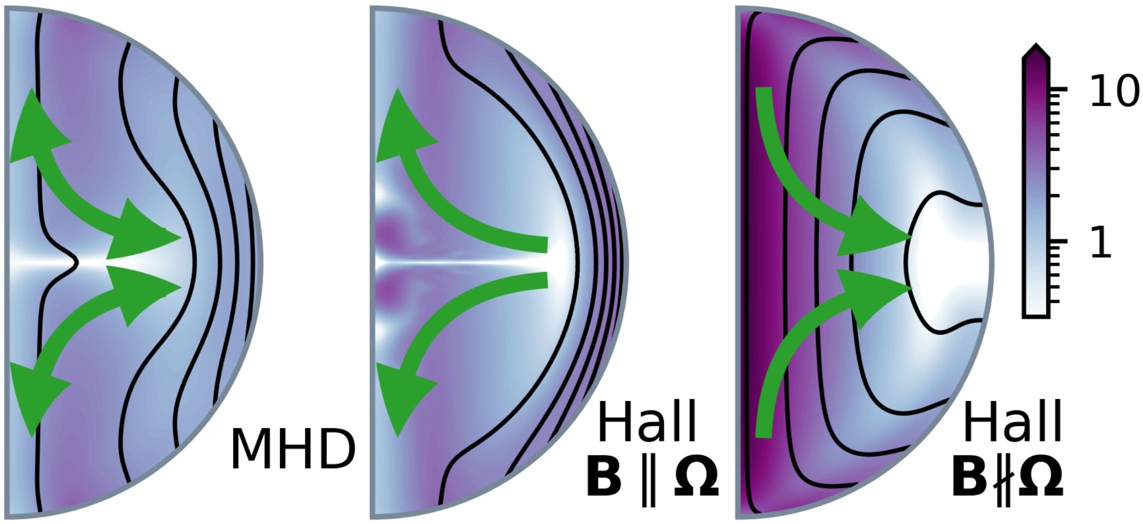

Figure 4.18: $|\mathbf{B}|/B_0$ and flux lines for NIMROD simulations. In all cases the initial field is uniform and has a strength of 0.5 G. The color contour is plotted on a log scale. Left: Case without Hall terms in Ohm's law. For either current direction, the resulting magnetic field is nearly identical; Middle: Case with Hall terms included in Ohm's law and the current directed inward. Right: Hall case with the current directed outward, which is the same as the experimental BRB case.

and resistivity, respectively. Unless noted, these are the values used for the simulations presented below.

4.3.2 Simulation results

Two major sets of comparisons were made with the NIMROD simulations: the inclusion of the two-fluid terms in Ohm's law and the direction of the injected current. For cases labeled as 'MHD' in this discussion, only the resistive term is included on the right hand side of Eq. 4.12 in the simulation. For cases labeled 'Hall', the full Ohm's law is used. This feature of NIMROD allows for a clear view of the relative importance of the Hall term in this equilibrium. Additionally, the current direction is easily changed in NIMROD. In cases where the anodes are located near the poles and the cathodes are near the equator, as in the BRB experiments described above, the radial current flows outward. In the VFD model, the flow drive is set by the $\mathbf{J} \times \mathbf{B}$ direction, so outwardly flowing currents will always produce a system where the flow rotation vector, $\mathbf{\Omega}$, is antiparallel to the initial magnetic field, $\mathbf{B} \nparallel \mathbf{\Omega}$. The other current direction, with cathodes near the poles and anodes positioned close to the equator drives the opposite case with $\mathbf{B} \parallel \mathbf{\Omega}$.

The simulations shown in Fig. 4.18 compare the equilibrium magnetic field for the different Ohm's law cases and injected current directions. In MHD Ohm's law cases there is no qualitative difference in the magnetic field when the injected current direction is flipped. However, when the Hall terms are included in Ohm's law, strong magnetic field expulsion or compression is shown. In the case with outwardly directed radial current, the same as the experiments on BRB, the field is strongly compressed on axis (this is labeled Hall $\mathbf{B} \nparallel \mathbf{\Omega}$ in Fig. 4.18). The factor of amplification is of the same order of magnitude as the experiment. When the current direction is flipped, the field is strongly expelled from the central volume.

In all the NIMROD simulations, a perfectly conducting boundary condition is used. As a result, magnetic flux is necessarily conserved in the volume and the field can only be expelled or compressed using the initial amount of flux. This is not observed in the experiment, where the total amount of flux is significantly increased and the aluminum vessel wall is not a perfect conductor. Despite this difference, there is a clear indication of strong field compression or expulsion when the two-fluid Ohm's law terms are included.

As in the experiment, the Hall $\mathbf{B} \nparallel \mathbf{\Omega}$ simulation drives a hollow density profile, shown in a radial cut at the midplane in Fig. 4.19. The hollow density profile shows diamagnetism of nearly 40%, which is fairly good agreement with the gradient observed in the experiment. Density profiles are not present in any of the other simulation configurations, suggesting that the extreme field compression is key to this feature.

The equilibrium flow is shown for the MHD and Hall cases with outward current in Fig. 4.20. In the MHD case, the poloidal circulation shows strong radially outward flow

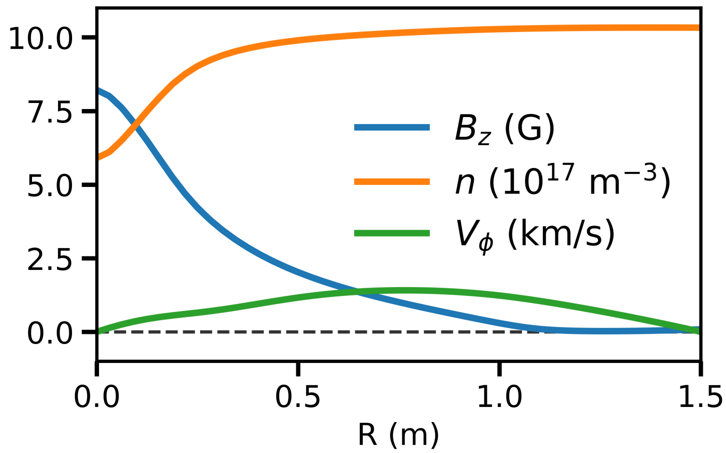

Figure 4.19: Linear cut at the equator of the density, toroidal flow and magnetic field from the Hall $\mathbf{B} \nparallel \boldsymbol{\Omega}$ case. The magnetic field and density profiles qualitatively match the experimental observations, but the flow is quite different.

near the equator, which drives the magnetic field advection. In both cases, the toroidal flow profile is not centrally peaked, as expected and observed. For the MHD case, the flow is peaked near the outer cathode location and for the Hall case the peak flow is close to the polar anode areas. There are several potential reasons for the mismatch in the predicted flow between the simulations and experiment. It is possible that the method of modeling the current injection does not capture a key feature that drives these flows or that there is an issue with the no-slip boundary condition used. Additionally, the flux-conserving boundary condition might be forcing a concentration of B_z near the walls, leading to drive at the anode locations.

A parameter scan of injected current and initial magnetic field strength, shown in Fig. 4.21, highlights the scaling of both the field amplification/removal and the diamagnetism. Over 250 simulations were run using the Center for High Throughput Computing (CHTC) cluster available through the UW-Madison computer science department. This

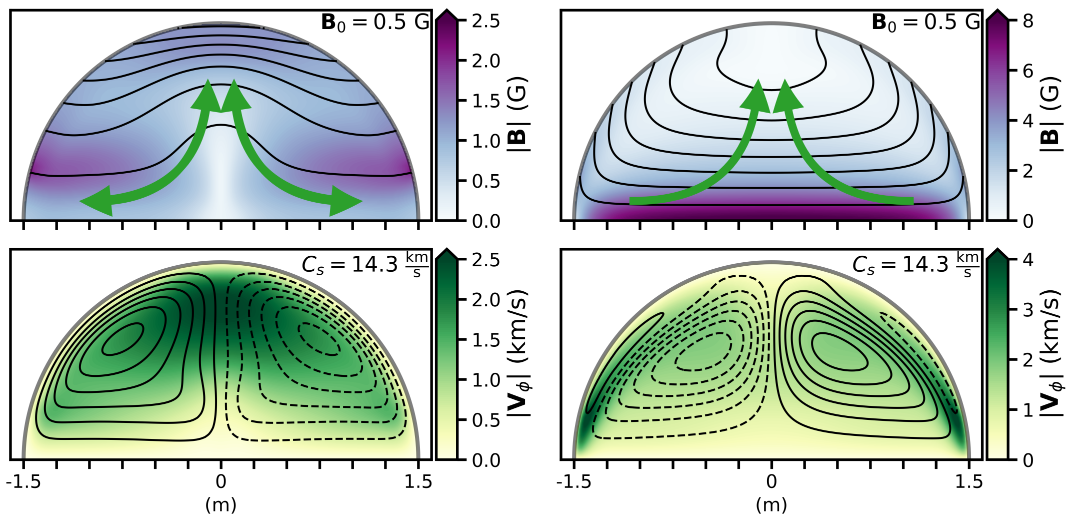

Figure 4.20: Left: MHD simulation showing the magnetic field (top) and toroidal flow (bottom). The poloidal flow streamlines are shown in the flow plot. For both current directions, the MHD simulations were very similar. Right: The same set of magnetic field and toroidal flow plots for the Hall case with outward radial current.

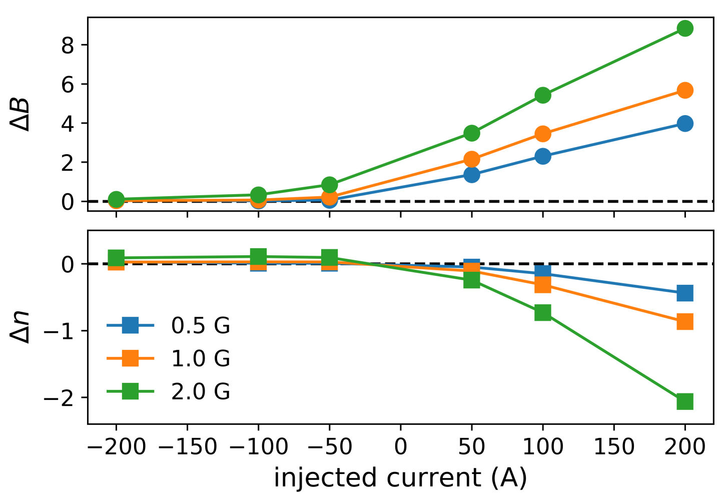

Figure 4.21: Top: a scaling of field amplification with injected current for three different initial field strengths. Bottom: the same scaling shown for the change in density. The values plotted are taken near the center of the simulation, at $R = 0.1$ m and $Z = 0$ m.

large scan produced results for a variety of applied field strengths, injected currents, temperatures, and densities. The scan shown here is limited to the same temperature and density used in the previously shown simulations.

The scalings indicated by Fig. 4.21 suggest that the injected current is the main driving force in both the field amplification and the hollow density profile. For cases with a negative injected current (radially inward current drive), the field is slightly removed from the center and the density in the center is relatively unchanged. For the radially outward current cases, the amount of field amplification and density hollowing is increased as the injected current is increased.

Throughout all the VFD NIMROD simulations, no evidence of any instability was observed. For many of the simulations, the toroidal mode number was set to $m = 0$ to reduce the computing time, however several cases with strong current drive were run with six toroidal harmonics. In these cases, as in the ones presented above, the toroidal flow was not centrally peaked and did not have sufficient shear to drive the MRI or any other flow-driven instabilities. Appendix B explores a different initial field and current injection configuration that mimics von Kármán flow. In this configuration NIMROD simulations did produce unstable behavior that seemed to be related to the slow dynamo instability.

4.4 Model

The NIMROD simulations presented in the previous section help to connect the field amplification to the inclusion of the Hall terms in Ohm's law. The Hall term describes the decoupling of ions from the magnetic field, which becomes frozen-in to the electron fluid. When the Hall Ohm's law is combined with Faraday's law, the induction equation clearly shows that the electron fluid is solely responsible for the magnetic field advection,

$$\frac{\partial \mathbf{B}}{\partial t} = \nabla \times (\mathbf{V} \times \mathbf{B}) - \frac{1}{ne}\nabla \times (\mathbf{J} \times \mathbf{B}) + \eta \nabla^2 \mathbf{B} \equiv \nabla \times (\mathbf{V}_e \times \mathbf{B}) + \eta \nabla^2 \mathbf{B} \qquad (4.17)$$

where the definition of the plasma current in the limit $m_e/m_i \ll 1$ has been used to combine terms. In this Hall regime, the electron fluid, which is the primary current carrier due

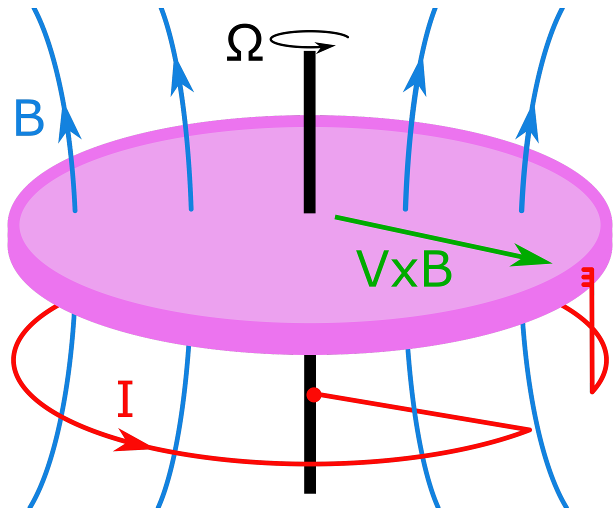

Figure 4.22: The homopolar disk dynamo is a similar system to the field amplification seen on the BRB. A rotating, conducting disk (pink) embedded in a magnetic field (blue) drives an electromotive force (green) which drive a current through a wire (red). The wire is wrapped around the system so the current acts to enforce the initial field. When the disk is spun fast enough, this system will sustain a self-consistent magnetic field.

to the high mobility of the light electrons, drags magnetic field lines. For the case with an outwardly directed radial current, the electrons will flow radially inward and compress the magnetic field on axis.

In addition to the electron field advection, this model should be able to describe the density gradient that is observed both experimentally and in the simulations as well as the centrally peaked flow. The density gradient is mitigated by a radial electric field that couples the magnetized electrons and the mostly unmagnetized ions. Below, I will first describe the field amplification via the Hall effect and then tie in the ion dynamics for a complete, simple model for this dynamic high-β Hall equilibrium.

4.4.1 Electron dynamics: field amplification and removal

The basic mechanism for the field amplification is similar to the homopolar disk dynamo model [78]. In this dynamo (shown in Fig. 4.22), a conducting disk threaded by a vertical magnetic field is spun, setting up an electromotive force (EMF) that drives a current through a wire. The wire is arranged such that the current acts to enforce the existing magnetic field. Above a critical rotation speed, this system can grow a magnetic field self-consistently. In the volumetric flow drive equilibrium, radially injected current drives the rotation, and via the Lorentz force, is deflected into the toroidal direction. The toroidal current acts like the wire in the homopolar disk dynamo system and reinforces the applied magnetic field. Our system is not a dynamo because there is no feedback mechanism. Rather, the injected current is driven by external power supplies and flux is brought into the system from the external Helmholtz coils.

In order for the plasma current to be deflected by the Lorentz force, it is key to have one of the charge species decoupled from the magnetic field. In the Hall limit, this means that the ions are decoupled and cannot drive inductive currents. Additionally, in the case of a weak magnetic field, collisions can become dominant over the Lorentz force for the ions. Both of these conditions are met in this model, effectively rendering the ion fluid completely unimportant for determining the magnetic field dynamics.

In the limit of inertia-less electrons, which is easily met in the plasma conditions considered in this work, Ohm's law fully describes their dynamics. This can be easily derived from the full two-fluid momentum balance equations in the limit that $m_e/m_i \ll 1$. In a steady state, axisymmetric, cylindrical system, it is necessary that the inductive electric field, E_ϕ is zero. The corresponding component of Ohm's law,

$$0 = E_\phi = \mu_0 \eta J_\phi - V_z B_r + V_r B_z + \frac{1}{ne}(J_z B_r - J_r B_z) = \mu_0 \eta J_\phi - V_z^e B_r + V_r^e B_z \qquad (4.18)$$

shows a relationship between the toroidal current and the electron flow when the definition of the plasma current is used in the limit that $m_e/m_i \ll 1$ as in Eq. 4.17. In our model, we wish to capture the simple dynamics of the vertical magnetic field because no other components were prominent in experimental observations. Therefore, the only component of the magnetic field is B_z, and the toroidal Ohm's law expression can be further simplified to a relation between the toroidal current and the radial electron flow,

$$J_\phi = -\frac{1}{\mu_0}\frac{\partial B_z}{\partial r} = -\frac{1}{\nu_e}\left(\frac{eB_z}{m_e}\right)(neV_r^e) = \frac{\Omega_{ce}}{\nu_e}J_r \tag{4.19}$$

where a simple form of resistivity has been used to relate η to the effective collision frequency, ν_e, and $\Omega_{ce} \equiv eB/m_e$ is the electron gyrofrequency [2]. Ampere's Law relates the inductive current, J_ϕ, to radial gradient of B_z, leaving a simple differential equation for the magnetic field. If V_r^e is negative, as in the BRB experiment, the magnetic field must be centrally peaked. In the opposite case, the field will increasing with radius. This relates to the observations made in both the experiment and the NIMROD simulations. The final equality in this expression clearly highlights the deflection of the injected radial current into the toroidal direction. It is clear that for sufficiently well-magnetized electrons, the toroidal current can be quite large for a modest injected radial current. In the plasmas created in the BRB experiments, Ω_{ce}/ν_e is greater than unity even at the initial field strength.

The electron flow can be determined from the radial component of Ohm's law,

$$E_r = \mu_0\eta J_r - V_\phi^e B_z - \frac{1}{ne}\frac{\partial P_e}{\partial r} \tag{4.20}$$

where the electron pressure, P_e, is included because the radial density gradient is a key feature observed in both the experiment and the simulations. Combining this component of Ohm's law with Eq. 4.19 results in a simple drift expression for the electron flow,

$$V_\phi^e = -\frac{\Omega_{ce}^2}{\Omega_{ce}^2 + \nu_e^2}\left[\frac{E_r}{B_z} + \frac{1}{B_z}\frac{1}{ne}\frac{\partial P_e}{\partial r}\right] \quad , \tag{4.21}$$

which is simply the $\mathbf{E} \times \mathbf{B}$ drift and the diamagnetic drift mitigated by collisions. The collision term in the front is often close to unity for the plasmas of interest because the electrons are well magnetized. The effect of the Hall term is to make the $\mathbf{E} \times \mathbf{B}$ drift capable of producing a current because the ions do not experience a strong Lorentz force.

[2] In this expression the sign of the magnetic field is included in the gyrofrequency, such that a positive or negative magnetic field is enforced by a positive radial current.

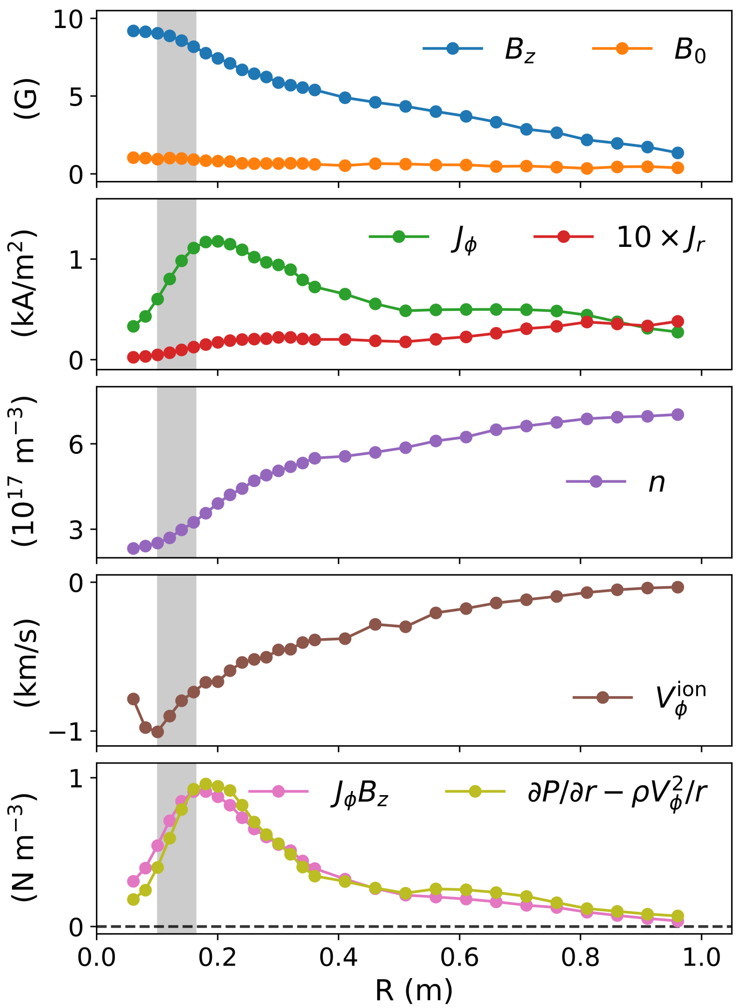

Figure 4.23: Linear profiles from case 1 on the BRB volumetric flow drive experiments. The ring anode radial shadow is indicated by the gray bar. From top to bottom: the magnetic field, the calculated current density, the plasma density, the ion toroidal flow, and force balance as described in Eq. 4.24

4.4.2 Ion dynamics: radial electric field and flow

Equation 4.21 indicates that the strong electron drifts are responsible for creating currents necessary for magnetic field amplification or removal is dependent on both a radial electric field and a radial pressure gradient. In order to understand these terms and their relative strengths, it is necessary to consider the largely unmagnetized ions. The steady-state radial component of the ion force balance without a Lorentz force is

$$m_i n \left(V_r \frac{\partial V_r}{\partial r} - \frac{V_\phi^2}{r} \right) = neE_r - \frac{\partial P_i}{\partial r} + nm_e \nu_e V_r^e \quad , \tag{4.22}$$

where the left hand side is the inertial forces and the right hand side has the electric field, the pressure gradient and the resistive collisions with the fast electrons (assuming $V_r^e \gg V_r$). The presumably weak radial flow can be neglected, leaving a simple expression for the radial electric field,

$$E_r = \frac{1}{ne} \frac{\partial P_i}{\partial r} - \frac{\nu_e}{\Omega_{ce}} V_r^e B_z - \frac{m_i}{e} \frac{V_\phi^2}{r} \quad . \tag{4.23}$$

Following an ordering based on the experimental BRB parameters, the radial electric field is mostly balanced by the ion pressure gradient. The second term is a small resistive electric field component and the last term is the inertial flow correction. If this electric field is used in the expression for the electron flow, Eq. 4.21, and the currents are considered to be full supported by electron flow, the standard 1-D, B_z only MHD equilibrium is recovered.

$$J_\phi B_z = \frac{\partial P}{\partial r} - nm_i \frac{V_\phi^2}{r} \tag{4.24}$$

where $P \equiv P_e + P_i$ is the total pressure. If this equilibrium condition is combined with the Hall mechanism for deflecting injected J_r into the toroidal direction, it is clear that the hollow density profile must accompany the amplified magnetic field on axis.

This simple equilibrium can be confirmed using the experimental BRB data. The toroidal current is calculated using the radial gradient of the magnetic field. At the bottom of Fig. 4.23, the terms in Eq. 4.24 are compared and show good agreement, indicating that the simple MHD equilibrium matches the data quite well. The small mismatch near the

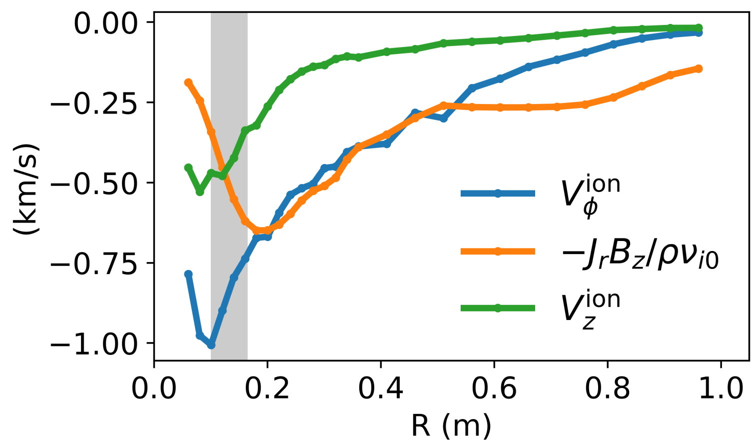

Figure 4.24: Radial profiles of the toroidal and axial ion velocity as well as the inviscid, inertia-less flow drive for the ions.

axis is likely due to the 2D nature of this equilibrium at small r due to poloidal circulation of flow and currents, which have been left out of this model.

The ion flow is complicated to model in the partly magnetized regime. Neutral collisions disrupt the ion gyro-orbits, which are on the order of the system size, and the strong density gradient is likely driving radial flow with inertia that must be accounted for in the toroidal force balance. Despite these complications, the simple model of the $\mathbf{J} \times \mathbf{B}$ force mitigated by neutral collisions (Eq. 4.3) does show reasonable agreement over a range of the profile in Fig. 4.24. The radial current is calculated using the toroidal current and the relation in Eq. 4.19 and the neutral charge exchange collision frequency is set at 760 Hz which corresponds to a neutral density of $n_0 \simeq 1.1 \times 10^{18}$ measured by the cold cathode gauge. As Fig. 4.24 suggests, the disagreement with the flow profile near the axis is most likely due to inertial forces associated with the poloidal circulation (measured here in V_z).

4.5 Summary

In summary, a new method of driving fast, weakly magnetized and centrally peaked flows has been demonstrated on the BRB. This so-called volumetric flow drive has been considered for MRI experiments in liquid metals where two-fluid effects are non-existent. In the VFD experiments presented here, the Hall term drives a large magnetic field amplification that drastically alters the equilibrium.

The equilibria driven on the BRB are shown to be unstable to the ideal MRI as well as simple interchange-like hydrodynamic modes. The amplified magnetic field does not fully stabilize the profile, rather dissipation and neutral collisions are the limiting factors. A straightforward linear WKB analysis of the MRI with dissipation, the Hall term, and neutral charge-exchange collisions shows that the same factors that were identified in Chapter 3 hinder MRI growth in this system. The key difference is that the flow profiles studied here were actually realized in the experiment. Future optimization of the density and neutral pressure either by more injected power or different gas species, could lead to flows that are MRI unstable based on this simple analysis.

The next half of this chapter focused primarily on understanding the mechanisms that go into this unique equilibrium. NIMROD simulations tailored to current inject experiments on the BRB show that the Hall term is key to the magnetic field amplification effect, and that a current reversal leads to extreme diamagnetism.[3] Beyond simply indicating that the Hall term is important for the magnetic field dynamics, these simulations also showed that the amount of field amplification is tied most directly to the total amount of injected current. A simple model describes how the radial injected current is deflected into the toroidal direction via the Hall term in the generalized Ohm's law. This model correctly predicts the field amplification and removal based on the sign of J_r and shows that in the limit of well magnetized electrons, a modest radial current can drive large toroidal currents responsible for the magnetic field dynamics.

Finally, the ion force balance shows that the extended density gradient is supported by a small radial electric field. When combined with the Hall amplification mechanism, this electric field completes the standard force balance between the $\mathbf{J}\times\mathbf{B}$ force and the pressure

[3] The reversed current also changes the relative alignment of the flow angular momentum and the magnetic field to the unfavorable, $\mathbf{\Omega} \parallel \mathbf{B}$, condition for exciting the Hall MRI.

gradient. Our model explains the hollow density profiles observed on the BRB and in simulations. The exact mechanism behind ion flow is poorly understood and likely tied to the partial magnetization of the ions across the profile as well as 2D poloidal circulation effects on inertial forces.

Chapter 5

High-β Hall Instability on PCX

A major prediction of both the NIMROD simulations and the simple model presented in the last chapter is the removal of an initial magnetic field when the cross-field current is flipped in the VFD configuration. In the high-β Hall limit, the electron fluid will advect the magnetic field lines radially outward when J_r is negative. This rearrangement of the magnetic field should have consequences for the ion flow as well, forcing the driving region to the outer boundary of the plasma. An instability is observed in this VFD configuration despite the alignment of the magnetic field and rotation vector that should not allow any positive growth rates for the MRI in the Hall regime.

In this chapter, I will describe the volumetric flow drive with radial inward current experiments performed on PCX. In stable cases, the plasma expels the magnetic flux as predicted and drives a relatively weak, solid-body profile flow. A parameter scan reveals large fluctuations tied to a mostly $m = 1$ mode rotating at frequencies between the ion and electron gryofrequency. After describing these observations, I will show that they are an electromagnetic extension of the gradient drift instability (GDI) [79]. In the $\beta = 0$ limit, the GDI is not expected in PCX; however, with the electromagnetic extension, a region of parameter space is opened that allows unstable modes in these plasmas. This electromagnetic instability could have implications for future Hall flow experiments as well as many other laboratory astrophysics plasmas.

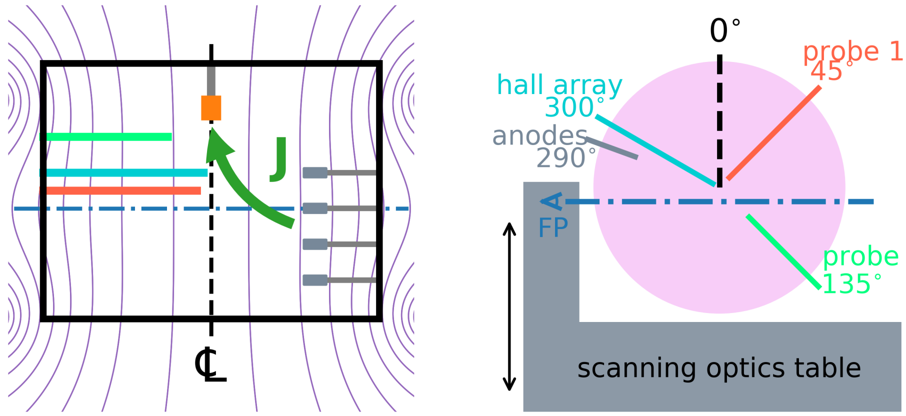

Figure 5.1: Schematic of the VFD setup on PCX. The left hand side shows the poloidal location of electrodes and probe along with the background Helmholtz field. On the right is a top down view that shows the toroidal location of the probes and electrodes. The Fabry-Perot line of sight has a fixed z location at the midplane of the Helmholtz coils, but the scanning optics table allows for multiple different tangency radii

5.1 Reversed current volumetric flow drive

As a natural extension of the BRB experiment, VFD with a inward radial current has been driven on PCX, with the configuration shown in Fig. 5.1. A single LaB_6 cathode is inserted on axis from the top of PCX and biased with respect to four molybdenum anodes placed near the outer edge of the plasma, just beyond the strong cusp field. The total injected current in PCX ranges from 20-100 A, mostly limited by the single cathode and power supply. Due to the small spacing between adjacent magnet rings, a poloidal sweep probe does not fit in the PCX geometry. However, ports are toroidally spaced around the vessel allowing for measurements of any non-axisymmetric features. Like the BRB experiment, PCX used a 3-axis 15 position Hall probe array for magnetic field measurements and a combination Mach/Triple or Mach/Langmuir probe for single point measurements of the electron temperature and plasma density.

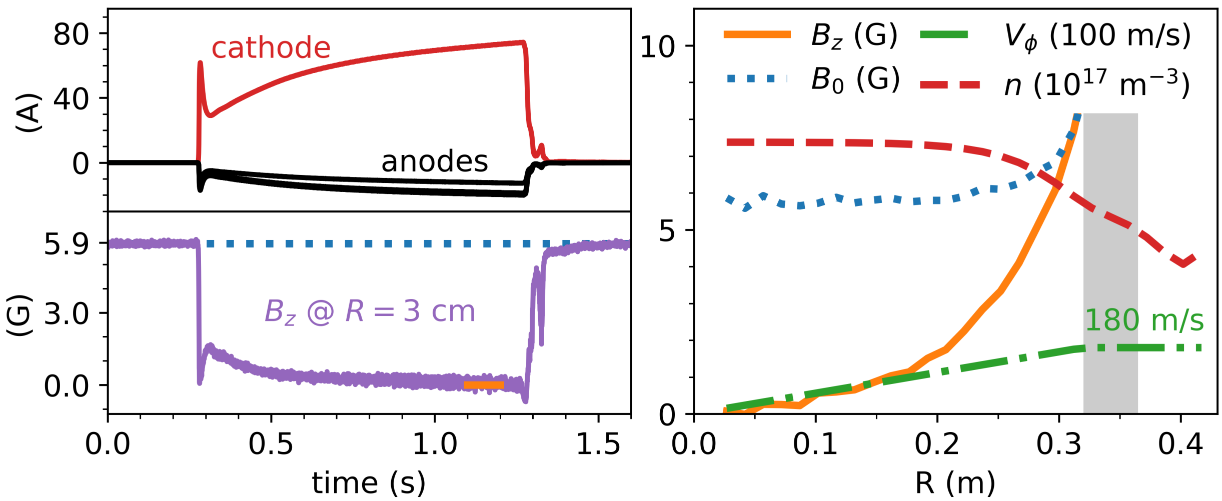

Figure 5.2: Equilibrium data for VFD on PCX. Top Left: time traces of the electrode currents. The anodes all draw roughly the same current except for the lowest one (furthest from the cathode). Bottom Left: time trace of the magnetic field measurement at the smallest radius reached by the Hall array. Right, linear profiles of the magnetic field (applied and equilibrium), the weak toroidal flow and the density. The gray shaded region indicates the radial location of the anodes. The probe measurements in this plot were made at the "probe 1" location indicated in Fig. 5.1

There are several key differences between the outwardly driven radial current case (BRB) and this inward current case. Figure 5.2 shows time traces of the injected current and the magnetic field as well as linear profiles of magnetic field, density and toroidal velocity. The most notable difference is the expulsion of the initial field rather than amplification. At the maximum injected current, the plasma removes nearly all of the applied magnetic field from the central region. This level of diamagnetism far exceeds other high-β helicon-type experiments, where the largest levels are usually $< 2\%$ [80, 81]. The change in magnetic field is negative throughout the entire plasma up to the anode location and positive outside of that, indicating that the injected current is the primary factor.

Another key difference is the relatively weak solid-body flow profile. The magnitude of the flow is small enough that Mach probe analysis could not reliably record it; however, the Fabry-Pérot spectrometer has excellent velocity resolution. Measurements of the flow profile are shown in Fig. 5.2. The peak flow occurs at roughly the anode location, similar to the central peaked flows on the BRB in the reversed configuration. With the removal of magnetic field, the region near the anode would correspond to the largest $\mathbf{E} \times \mathbf{B}$ drift velocities, indicating that the flow is driven locally at the anode.

The measured equilibrium on PCX shows excellent agreement with the model discussed in Chapter 4. As predicted, the change in current direction leads to an expulsion of the initial magnetic field. This is due to the strong toroidal electron current. Following the force balance equilibrium, a long density gradient is extended from the outer edge of the plasma well into the main volume, where the magnetic field has been mostly removed. The solid-body profile of the ion flow is similar to previous edge-driven experiments [23], where local torque injection is viscously coupled. In the absence of frequent ion-neutral charge-exchange collisions, this solid body profile is expected in a viscously coupled, outer boundary-driven flow.

The equilibrium present in Fig. 5.2 represents a single applied field case, however, a scan was undertaken to understand the dependence on certain features with respect to the initial applied magnetic field. Notably, the maximum injected current, therefore the peak flow speed, increases with increased applied field up to a point where strong fluctuations are observed.

For a fixed neutral fill pressure, Fig. 5.3, shows the scalings of both the maximum injected current and the final magnetic field (taken at $t = 1$ s). The final magnetic field is always smaller in magnitude than the initial field and, for stable cases, reduces to a fixed value despite the initial field. This is another experimental confirmation of the Hall mechanism acting to, in this case, reduce the initial magnetic field. As more radial current is injected and diverted into the toroidal direction, more initial field can be removed. The fixed value that the field reduces to is approximately 2 G and changes depending on the neutral fill pressure, which sets the plasma density. This fixed value appears to be dependent on the initial β of the plasma.

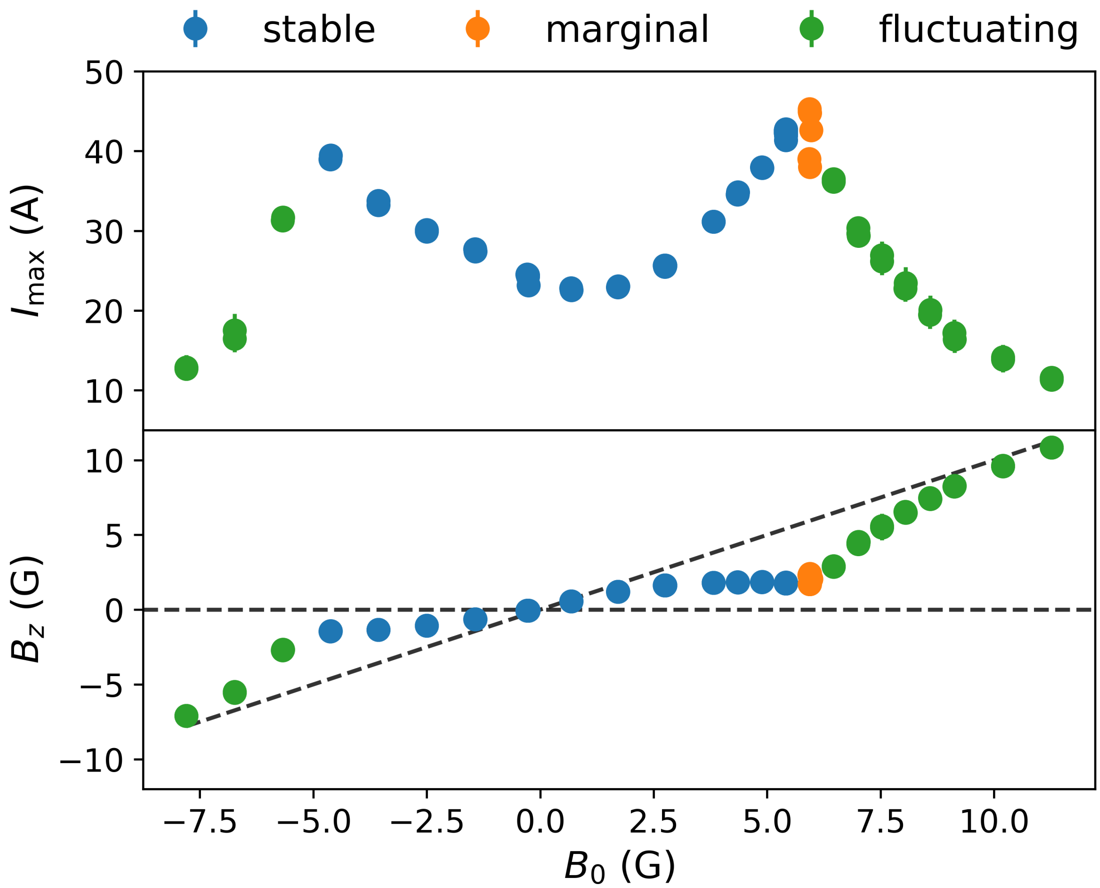

Figure 5.3: Top: The scaling of maximum injected current versus applied magnetic field. As the initial field magnitude is increased, more current is injected up to a point where strong fluctuations begin. Bottom: Scaling of final (at $t = 1$ s) magnetic field at $R = 20.7$ cm versus applied field. The sloped dashed line indicates the case in which the field is unchanged. For all cases measured, the magnitude of the final field is lower than the initial applied field. For stable cases, the field is reduced to roughly 2 G regardless of the initial field, most likely the result of increased current. Once fluctuations begin, the amount of field removed reduces mostly due to the reduction in injected current.

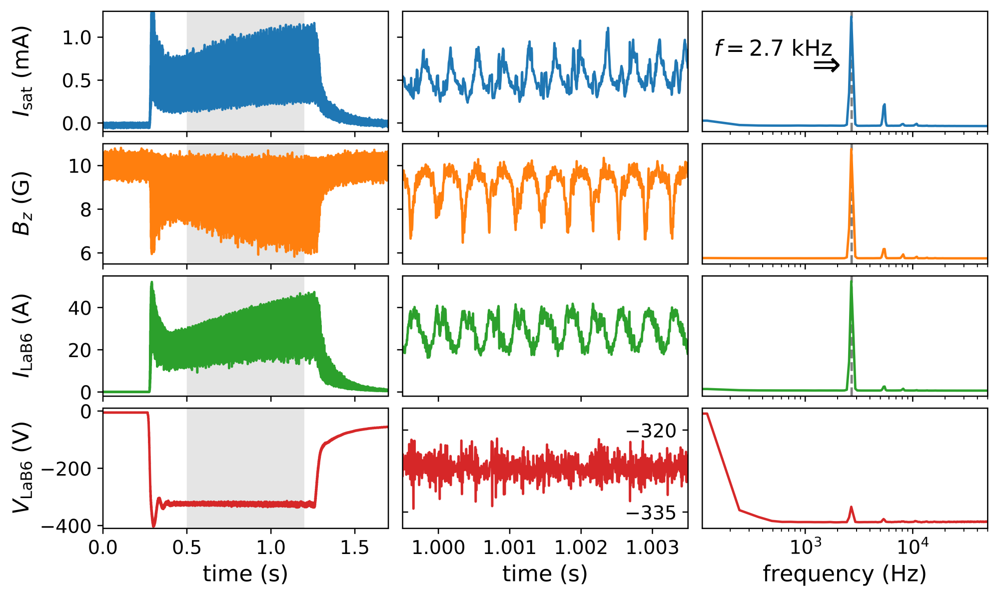

Figure 5.4: Left: Time traces of the ion saturation current, B_z, the cathode current and the bias voltage from top to bottom. Middle: a zoomed in view showing several periods of oscillation. Right: FFTs of the time traces (window is shown in grey on left) showing a dominant mode at $f = 2.7$ kHz. The small feature seen in the voltage trace is most likely due to pickup, indicating that the power supply is not responsible for driving any of these fluctuations.

5.2 Observations of instability

At higher initial magnetic field strengths large fluctuations were observed on all electrostatic probe signals as well as the B_z component of the Hall array. As indicated in Fig. 5.3, the onset of the fluctuations greatly reduced the injected current, and therefore, the field removal. The frequency of the fluctuations was roughly 2-3 kHz, which is well below the electron cyclotron frequency ($f_{ce} \simeq$ 5-20 MHz) and above the ion cyclotron frequency ($f_{ci} \simeq$ 100-300 Hz)[1]. Time traces and FFTs of various probes are shown in Fig. 5.4.

[1]Factors of 2π are important to keep track of when comparing experimental frequencies to those used in theory and models, $\Omega_{cs} = 2\pi f_{cs}$

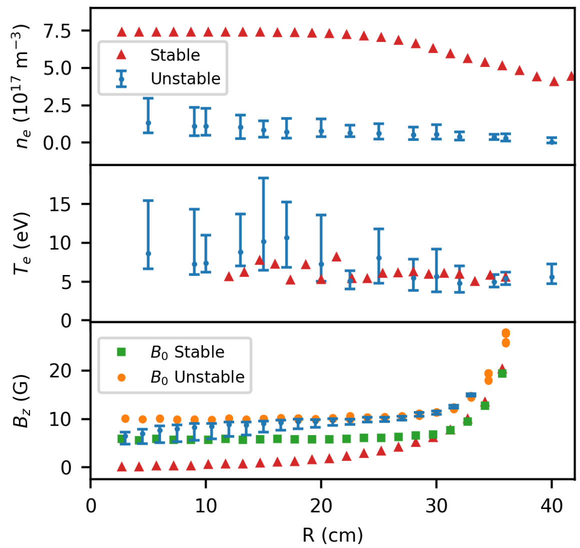

Figure 5.5: Radial profiles comparing the equilibrium case where no fluctuations are measured to a fluctuating case. The error bars on the fluctuating case show the median value over many periods with the extrema indicating the amplitude of the fluctuations.

The fluctuations are present on nearly all measurements, with the exception of the bias voltage. This clearly shows that the power supply is not introducing this relatively low frequency oscillation into the system. Hall probe array measurements of the radial and toroidal components of the magnetic field do not show any sign of coherent fluctuations. This could be due to the small magnitude of these components, but it does indicate that $k_{\|}$ must be very small compared to k_r for this mode.

In the marginal set of initial field cases (indicated in Fig. 5.3), the fluctuations are immediately present at the beginning of the discharge and then abruptly stop midway through the shot. Throughout most hot cathode discharges, the injected current slowly increases in time due to the self-heating of the cathode. In these marginal cases, a point is reached where the current can remove enough field via the Hall mechanism to stabilize the fluctuations. For the particular fill pressure investigated here, this critical magnetic field strength appears to be at around 2 G, above which fluctuations are observed. For the

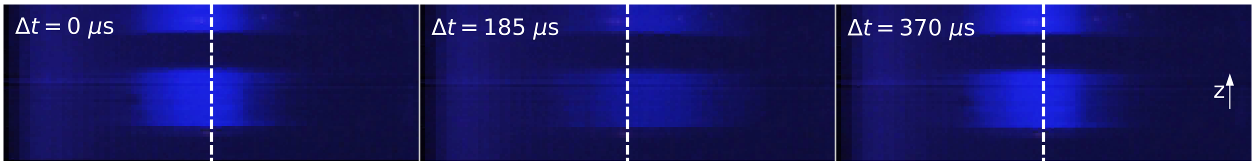

Figure 5.6: Stills from a high-speed video taken at a frame rate of roughly 27 kHz. This video is taken from a radial view near the midplane, showing that the mode is predominantly $m = 1$ and has little axial variation in the region captured.

fully fluctuating cases, the current is suppressed throughout the discharge, allowing for a stronger magnetic field.

Radial profiles comparing the density, electron temperature, and magnetic field for a non-fluctuating equilibrium case and a fluctuating case are shown in Fig. 5.5. The error bars for the fluctuating case indicate the median value taken over many periods, with the extrema showing the amplitude of these fluctuations. The density gradient is largely removed for the median and lower bound in the unstable case, indicating that the instability is acting to remove this source of free energy. The triple probe measurements of very high electron temperatures during fluctuations are suspect and likely caused by non-Maxwellian electron populations [2]. In the higher initial B_0 case, the instability is excited and less field removal is seen. This is consistent with the lower magnitude of injected current and the reduced radial gradient in B_z, which is equivalent to the toroidal current.

Using the large viewports near the midplane, high-speed video taken at a frame rate of roughly 27 kHz clearly shows an area of increased emission, which is tied to density, rapidly rotating at the frequency of fluctuations. A set of stills from this video, shown in Fig. 5.6, show that there is little variation in the axial direction and that the mode is mostly $m = 1$.

Taking advantage of the various toroidal probe locations on PCX, the mode structure of these fluctuations can be mapped, assuming a $m = 1$ mode. Figure 5.7 shows the ion saturation current measured by probes separated by $90°$ toroidally and 18.5 cm vertically. For

[2] Langmuir I-V curves of these plasmas were well fit with two electron temperatures.

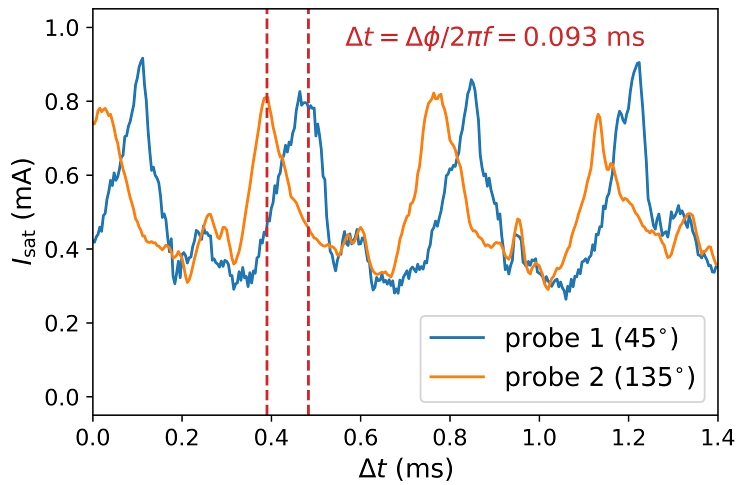

Figure 5.7: A comparison of the ion saturation current taken at two probe locations separated by 90° toroidally. For this case, the dominant frequency is 2.7 kHz which corresponds to a lag time of 0.093 ms. The vertical lines indicate the maximum current during a period at both these locations separated by this calculated lag time.

a positive applied magnetic field, the mode rotates in the anti-clockwise direction when viewed from above. The lag time between the two signals can be calculated using the dominant fluctuation frequency. These two probes are separated in z by 18.5 cm, yet a simple lag that assumes no variation along z matches the data very well.

Using the Hall probe array as a fixed reference, probe 1 was scanned radially with each separate location synced. A 2D map of the mode structure for B_z and I_{sat}, shown in Fig. 5.8, can be constructed by converting the measured period of fluctuation to toroidal angle. These two maps have been corrected for the toroidal lag due to the location of the Hall probe array to show the same structure. This rotating mode consists of an area of increased density and the resulting diamagnetic removal of magnetic field.

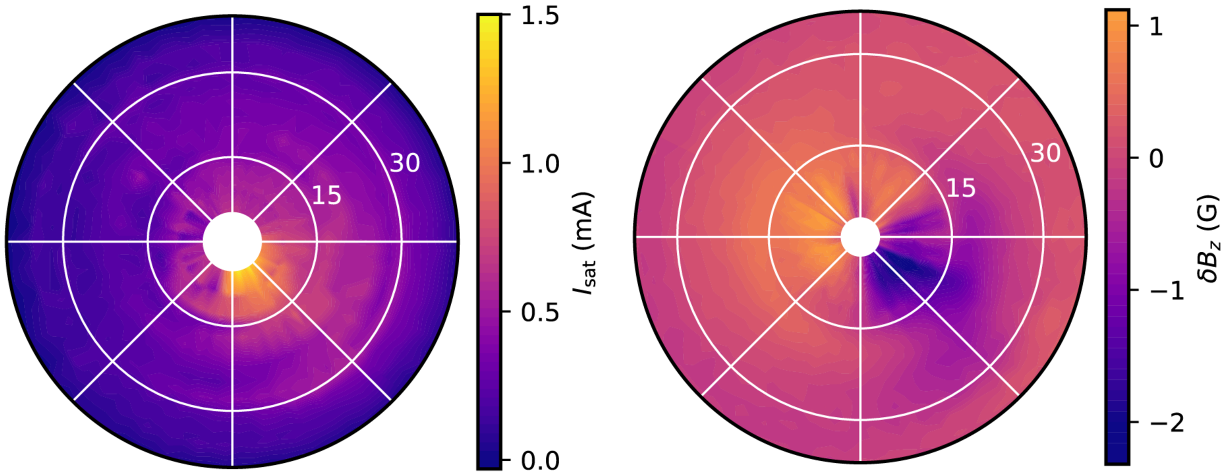

Figure 5.8: 2D reconstructions of the toroidal mode structure for the fluctuations observed on PCX. Left: the ion saturation current measured by a radially scanned probe at $\phi = 45°$. Right: B_z measured by the Hall array at $\phi = 300°$. The toroidal lag between these locations has been accounted for to line up the density and magnetic field features at $\phi = -45°$.

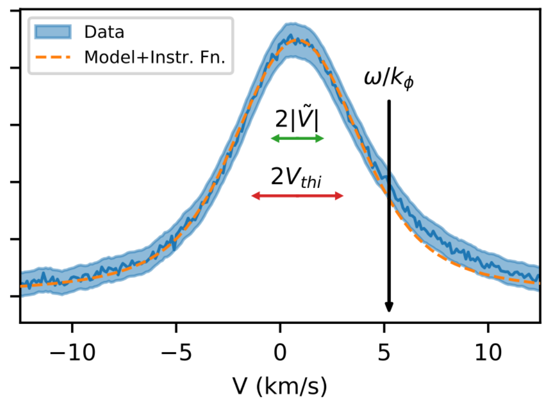

Figure 5.9: Spectrum from the Fabry-Pérot spectrometer. The model is a thermally broadened Gaussian with a quiver velocity estimated from probe data. The right tail deviates from the model where Landau damping heats the tail of the ion distribution function.

5.2.1 Ion heating

In addition to the toroidally separated probe measurements shown above, the Fabry-Pérot spectrometer was used to measure the ion temperature and velocity averaged over many periods of fluctuations. In addition to the standard modeling of the thermal broadened and Doppler shifted spectrum, the quiver velocity, $\tilde{\mathbf{V}}$, was included using an estimated value based on the magnitude of the ion saturation current fluctuations measured by the electrostatic probe,

$$\tilde{\mathbf{V}} = \hat{k}\left(\frac{\omega - \mathbf{k}\cdot\mathbf{V}_{i0}}{k}\right)\frac{\tilde{n}}{n_0} \tag{5.1}$$

where $\mathbf{V}_{i0}$ is the mean ion velocity. Using this model, Fig. 5.9 shows the measured ion distribution function mapped to velocity space at a tangency radius of 30 cm.

Near the phase velocity of the rotating mode, the measured distribution function deviates from the Gaussian model. This indicates that a non-Maxwellian feature most likely resulting from Landau damping of the rotating mode is present. Through this process, energy from the electromagnetic fluctuations (driven by the large electron currents) is transferred to the ion population and thermalized. The resulting ion heating is considerable compared to non-fluctuating plasmas at similar densities. In the case shown in

Fig. 5.9, the ion temperature fit is 1.4 eV, which is roughly 4 times the temperature of a similar density plasma without fluctuations. For a more detailed description of the Fabry-Pérot measurements of these plasmas, see Jason Milhone's thesis [58].

5.3 High-β, collisionless Hall instability

Instabilities that arise from cross-field currents have been the subject of research for quite some time. The Simon-Hoh [82, 83] instability describes how a cross-field electric potential and density gradient can destabilize a plasma, particularly when they are aligned such that $\mathbf{E}_0 \cdot \nabla n_0 > 0$. However, this instability does not consider the effects of a non-uniform magnetic field. Including the magnetic field gradient, the gradient drift instability (GDI) describes a very similar collisionless electrostatic instability driven by compressible electron drifts [79, 84]. The GDI is mainly applicable to Hall thrusters where strong magnetic fields remain unaffected by the low-β plasma. Here I will present a high-β, electromagnetic extension of the GDI that serves as an excellent linear theory for the fluctuations seen on PCX.

The general approach to this derivation is based on Sec. II of Frias et. al. [79], with deviations to allow for high-β. The continuity and momentum balance equations for both the ions and electrons are linearized in the Boussinesque approximation, assuming a Fourier solution, $\propto e^{-i\omega t + i\mathbf{k}_\perp \cdot \mathbf{r}}$, with $k_\perp^2 = k_r^2 + k_\phi^2$. Starting with the ion fluid, the continuity and momentum balance are

$$\frac{\partial n}{\partial t} + \nabla \cdot (n\mathbf{V}) = 0 \tag{5.2}$$

$$\frac{\partial \mathbf{V}}{\partial t} + (\mathbf{V} \cdot \nabla)\mathbf{V} = -\frac{e}{m_i}\nabla\Phi - V_{thi}\frac{\nabla n}{n} \tag{5.3}$$

where $V_{thi} = \sqrt{T_i/m_i}$ is the ion thermal speed and the temperature is assumed be constant. The momentum balance for the ions does not include the magnetic field or collisions because both of these forces are significantly smaller than the ballistic response from the fluctuating electric field and density gradient. Linearizing and rearranging these expressions leads to a Boltzmann-like response of the ions,

$$\frac{\tilde{n}}{n_0} = \frac{k_\perp^2}{(\omega - \mathbf{k}\cdot\mathbf{V}_0)^2 - k_\perp^2 V_{thi}^2}\frac{e\tilde{\Phi}}{m_i} \tag{5.4}$$

where fluctuating quantities are denoted by $\tilde{}$ and equilibrium values by $_0$. The weak ion flow enters only in the Doppler shift of the fluctuating frequency in the denominator of the right hand side of this expression. This expression is only valid when the Doppler shifted phase velocity is much higher than the ion thermal speed, $\omega - \mathbf{k}_\perp \cdot \mathbf{V}_0 \gg k_\perp V_{thi}$. In conditions close to this pole, a kinetic theory should be applied for the ions. For this analysis, I will drop this term because it will only be important for the Landau damping of the mode and will not strongly affect the real part of the frequency or the onset of the instability.

The electrons are modeled in the collisionless drift approximation, where flow is comprised of the $\mathbf{E}\times\mathbf{B}$ and diamagnetic drifts,

$$\mathbf{V}^e = \mathbf{V_E} + \mathbf{V}_{pe} \equiv \frac{\mathbf{B}\times\nabla\Phi}{|\mathbf{B}|^2} + \frac{T_e}{e|\mathbf{B}|^2}\frac{\nabla n}{n}\times\mathbf{B} \tag{5.5}$$

This drifting electron flow is compressible and leads to an electron continuity equation that includes the inverse gradient length scale of the magnetic field.

$$\frac{\partial n}{\partial t} + \mathbf{V_E}\cdot\nabla n - 2n\,\mathbf{V}^e\cdot\nabla\ln|\mathbf{B}| = 0 \tag{5.6}$$

The electromagnetic response of this instability is captured in the linearized form of Ampére's law in the limit that the ion flow does not contribute to the plasma current.

$$\nabla\times\mathbf{B} = \mu_0\mathbf{J} \simeq -\mu_0 ne\mathbf{V}^e \tag{5.7}$$

$$\frac{\tilde{B}}{B_0} = \frac{\beta}{2}\left(\frac{e\tilde{\Phi}}{T_e} - \frac{\tilde{n}}{n_0}\right) \tag{5.8}$$

where the second expression is reached by using the linearized form of the electron drifts and $\beta \equiv 2\mu_0 n_0 T_e/B_0^2$ is the electron plasma beta. Equation 5.8 clearly shows that in the low-β limit there are no magnetic fluctuations. This is the key component of this analysis

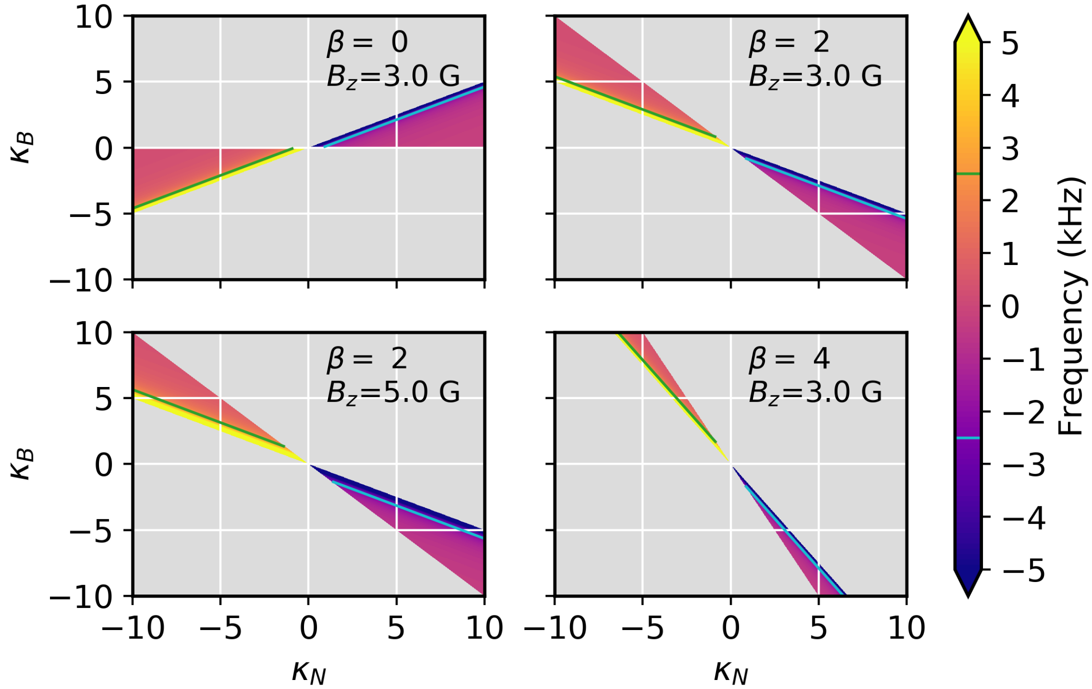

Figure 5.10: Regions of instability mapped in κ_B-κ_n phase space. For PCX, $\kappa_B > 0$ and $\kappa_n < 0$, so a finite β is required to have a growing mode. The frequency of the PCX fluctuations, nominally 2.5 kHz, is marked in the colormap to show that this linear theory matches well with the real experiment.

that differentiates the fluctuations seen on PCX from those present in Hall thrusters and other low-β systems.

Combining the linearized form of Eq. 5.6 and Eq. 5.8 leads to a relation between the electron density fluctuations and the fluctuating potential,

$$\frac{\tilde{n}}{n_0} = \frac{(1-\beta)V_* - V_D - \beta V_E}{(\omega/k_\phi) - (1+\beta)V_E - V_D - \beta V_*}\frac{e\tilde{\Phi}}{T_e} \equiv \frac{\mathcal{A}}{(\omega/k_\phi) - \mathcal{B}}\frac{e\tilde{\Phi}}{T_e} \tag{5.9}$$

where the equilibrium drifts are defined as,

$$V_* \equiv -\frac{T_e}{eB_0}\frac{1}{n_0}\frac{\partial n_0}{\partial r} \equiv -\frac{V_{the}}{\Omega_{ce}}\kappa_n\,, \quad V_D \equiv -2\frac{T_e}{eB_0}\frac{1}{B_0}\frac{\partial B_0}{\partial r} \equiv -2\frac{V_{the}}{\Omega_{ce}}\kappa_B\,, \quad V_E \equiv -\frac{E_0}{B_0} \tag{5.10}$$

The full dispersion for this linear analysis is found by equating Eqns. 5.4 & 5.9,

$$(\omega - \mathbf{k}_\perp \cdot \mathbf{V}_0) = \frac{1}{2}\frac{k_\perp^2}{k_\phi}\frac{C_s^2}{\mathcal{A}}\left[1 \pm \sqrt{1 - 4\frac{k_\phi^2}{k_\perp^2}\frac{\mathcal{A}}{C_s^2}(\mathcal{B} - V_0)}\right] \tag{5.11}$$

with a condition for instability (with $\mathcal{A}$ and $\mathcal{B}$ defined in Eq. 5.9),

$$\mathcal{A}(\mathcal{B} - V_0) > \frac{1}{4}\frac{k_\perp^2}{k_\phi^2}C_s^2 \tag{5.12}$$

This instability threshold is dependent on the equilibrium density and magnetic field as well as their inverse gradient length scales, κ_n and κ_B. Figure 5.10 shows the dependence of the stability on the inverse gradient length scales for several cases of density and magnetic field. For PCX, the density gradient is negative and the magnetic field gradient is positive (upper left quadrant of these plots). In the electrostatic limit ($\beta = 0$), there is no growing mode for this arrangement of gradients. However, when a finite β is included the unstable region of κ_B-κ_n phase space rotates, allowing for growth with the gradient directions found on PCX. At sufficiently high β, the region of instability is smaller, leading to stability for a fixed κ_n and κ_B.

5.3.1 Comparison to observations

The colormap in Fig. 5.10 represents the magnitude of the real frequency at the given densities and magnetic fields (neglecting the small Doppler shift due to the ion flow). For comparison to experiment, the nominal observed frequency of 2.5 kHz is indicated with a green or teal line. In cases where the gradient directions found on PCX are unstable, this frequency is present in the unstable region.

Figure 5.11 shows the growth rate, γ, as a function of β for fixed parameters from an unstable case on PCX. For low β, the mode is stable. As β is increased a region of instability is found that coincides with the observations on PCX. At even higher β, the mode is stabilized again. This β threshold is consistent with the onset shown in Fig. 5.3, where

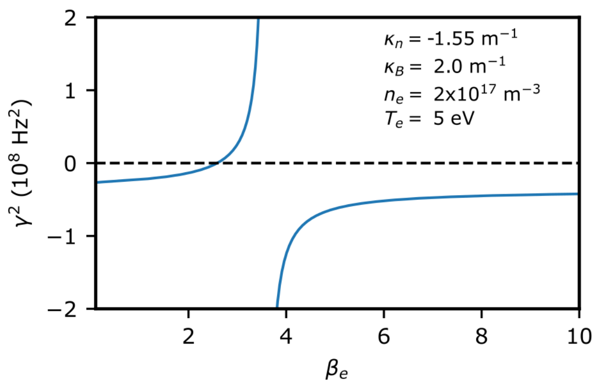

Figure 5.11: A plot of the growth rate squared versus β using parameters from an unstable case on PCX. The instability is only present when $\gamma^2 > 0$, which occurs only over a range of β.

fluctuations are only observed above a critical magnetic field. For all the unstable discharges in PCX, β was between 2 and 4, while the stable cases had $\beta > 5$, and in the case of complete field expulsion, $\beta = \infty$.

5.4 Summary

In summary, the reversed current configuration of volumetric flow drive has been implemented on PCX. In this mode, the Hall mechanism described in the chapter 4, expels flux and creates an extended density gradient at the outside of the plasma volume as expected. The accompanying flow is quite weak and solid-body like, indicating that the drive location is near the anodes and that the large magnetic field in this region both marginally magnetizes the ions and reduces the drift speed. The analysis of this flow profile requires the extremely high-precision Fabry-Pérot spectrometer with an absolute velocity calibration.

Empirically faster peak flow speeds are observed as the applied magnetic field, and in turn the injected current, is increased. At a certain threshold linked to the plasma β, strong, low-frequency ($f_{ci} \ll f \ll f_{ce}$) fluctuations are observed on all electrostatic and magnetic probes. Toroidally spaced probe measurements as well as high-speed video indicate that these fluctuations are linked to a predominantly $m = 1$ mode rotating in the direction of the magnetized electron drifts. Fabry-Pérot measurements of the ion distribution function averaged over many periods of these fluctuations shows strong ion heating (factor of 4) and an extended high-energy tail likely associated with a Landau damping process. The ion flow is also much larger during these unstable cases, reaching a peak velocity of nearly 1 km/s.

An electromagnetic extension of the gradient drift instability (GDI) is derived to predict a simple linear dispersion relation for these observations. By including finite β, a new regime in the instability phase space is opened, allowing for the particular alignment of the magnetic field and density gradients found on PCX ($\kappa_B < 0$ and $\kappa_n > 0$). For parameters found in PCX, positive growth of this instability is found in the region $2 < \beta_e < 4$, which matches very well with the measured β for unstable cases. At higher β, there is no instability growth, reflecting the observation of a critical magnetic field above which fluctuations are observed.

Chapter 6

Conclusions

In my 8 year graduate career, I have seen MPDX grow from an ugly, gray, magnetless shell into a big red national user facility. I have contributed a lot to this effort, from installing magnets to making vacuum interlock controls to developing state-of-the art diagnostics. Some of my major contributions which I would like to highlight include: the initial development of the mm-wave interferometer system, the design and installation of the vacuum interlock system, the flashy and promotional high-speed magnet smash video[1] and early iterations of the Fabry-Pérot spectrometer.

In addition to being part of the thrilling growth of the BRB, I was very lucky to be the main graduate student on PCX where I conducted a massive upgrade of the lab and the magnetic confinement system. Throughout the long and sometimes arduous magnet upgrade, I worked with John Wallace and Mike Clark to create a new version of PCX that is capable of matching BRB plasma parameters (for details see Appendix A). The magnet upgrade was a continual learning and problem-solving endeavor, starting by learning Solidworks and eventually into the never-ending leak checking and sealing of the magnet cooling system. PCX was already an incredible experiment when I arrived, and I have improved on nearly all aspects of lab: from the data acquisition and storage system, the addition of vacuum pumps for better neutral pumping during a discharge, and the installation of fish-eye webcams for observing discharges from the control room. I believe that

[1] Publicly available at this link: https://www.youtube.com/watch?v=iJyAQwrMR8E

these improvements serve PCX well, not only in terms of creating more interesting plasmas to study, but also in terms of adaptability and usage necessary for testing techniques and diagnostics which are being developed for the BRB.

I have highlighted these hardware contributions because they are often dismissed as superfluous or taken for granted. On the contrary, I believe that my contributions, and those by other graduate students, scientists and engineers, have made WiPPL into the plasma laboratory it is today. This work would not have been possible without the energy and labor I've devoted to these areas, and I'm thankful to have had the time and space to work on, develop and design these incredible experiments.

6.1 Summary

This work has shown the development of two methods of driving high-β, Keplerian-like flows with the goal of exciting the magnetorotational instability. Through the process of improving flow drive schemes, we have seen large Hall effects on the magnetic equilibrium. In one configuration of volumetric flow drive, we have observed a new electromagnetic instability that is associated with strong electron drifts present in the Hall regime. While this work set out to search for ion flow instabilities, a new and exciting field of research focused on these Hall effects and the resulting dynamics has opened up.

In the introduction, I motivated this work by describing the dynamo and magnetorotational instabilities. Most of the experimental focus on these flow-driven MHD instabilities has been in liquid metals, where dissipation is fixed. In plasmas, however, the viscosity and resistivity can be tuned by adjusting the plasma temperatures and densities. Most important to this work, I also outlined the importance of the Hall term in generalized Ohm's law and described how the magnetic field is frozen-in to the electron fluid in the Hall term.

Chapter 2 focuses on the specifics of plasma creation and flow drive as well as the diagnostics used in this work. A unique feature of the multi-cusp confinement scheme used on the BRB and PCX is the ability to create magnetic field free, uniform plasmas that can then be electromagnetically stirred at the boundaries. This makes for an ideal experimental environment for studying both the dynamo and the MRI in the lab. Notably, I outline the features of the magnetic confinement system of PCX which I spent considerable time and energy upgrading. This chapter ends with a detailed description of the design and analysis of electrostatic probes, magnetic Hall probe arrays, the mm-wave interferometer and the Fabry-Pérot spectrometer all of which I had a hand in creating and improving.

The next chapter begins with a model of edge-driven Taylor-Couette flow, where viscous momentum coupling is responsible for spinning the unmagnetized central volume of plasma. This momentum coupling is hindered by charge-exchange collisions with neutrals, which both decrease the magnitude of bulk flow and introduce more shear near the drive regions. A global stability analysis that uses the PCX geometry and neutral-modified Taylor-Couette flow shows that the MRI growth is affected by both the Hall term and the neutral collisions. I present a map of n-P_0 phase space for the MRI that highlights regions of stability, regions of solely MRI growth and regions where interchange-like hydrodynamic instabilities would occur, obscuring the MRI. The region of this phase space that is accessible to PCX partly overlaps with the positive MRI growth, however additional factors such as parasitic boundary layers bring to question how well the global stability model matches the experiment. Additionally, the flows used for the analysis have yet to be achieved on PCX, particularly at the inner boundary, where small cathodes are difficult to drive and maintain.

Motivated by the analysis of the previous chapter, Chapter 4 begins by introducing a new flow drive scheme, volumetric flow drive (VFD), that addresses both the difficulty of stirring at the inner boundary to produce peaked flow as well as the increased shear (and hydrodynamic instabilities) brought on by neutral charge-exchange collisions. This drive scheme drives strong radial currents across a weak background field that is applied over the entire plasma volume. This way a body force is imparted across the entire plasma and, due to geometry, the driving radial current is strongest near the axis, which leads to centrally peaked flow profiles. A run campaign on the BRB is described next, where centrally peaked flows are produced by VFD, but a striking magnetic field amplification is observed accompanied by a hollow density profile. NIMROD simulations indicate that this massive magnetic field amplification is connected to the Hall term in ideal Ohm's law and is dependent on the direction of injected current. In cases where the radial current is directed outwards, like on the BRB, the field is amplified. When the opposite current is applied, the field is expelled from the plasma. I close this chapter with a simple model of this Hall mechanism, which is similar to the classic homopolar disk dynamo. Radial injected current is deflected into the toroidal direction via the Hall term, driving large toroidal currents that either reinforce or oppose the applied magnetic field. The accompanying density gradient is also included in this simple model by considering the small electric field required to balance the ion pressure gradient. I show that the standard MHD equilibrium still applies to this system and that it explains the observed density profiles.

The last chapter explores the reversed current case of volumetric flow drive on PCX. As predicted by the NIMROD simulations and the simple model from the previous chapter, flux is expelled from PCX when driven with a radially inward current. In some cases, enough current is applied to entirely remove the magnetic field from the central region of the plasma. The ion flow is extremely weak and solid-body like, which indicates that the field removal is forcing the flow drive to the outer edge of PCX. This weak flow ($<$ 180 m/s) is only measurable due to the extremely high precision Fabry-Pérot spectrometer. Empirically, faster peak flow speeds can be reached with larger applied magnetic field, which is accompanied by larger injected currents. Above a threshold magnetic field strength, strong coherent fluctuations are observed with frequencies between the ion and electron gyrofrequency. Toroidally spaced probes and high-speed video show that these fluctuations are the result of a rapidly rotating, predominately $m = 1$ flute-like mode. Additionally, strong ion heating is observed, accompanied by a high energy tail of the measured ion distribution function, suggesting that the mode is heating the ions through a Landau damping process. This chapter ends with a linear analysis of the electromagnetic gradient drift instability, which is a high-β extension of an electrostatic mode observed in Hall thrusters. This instability is driven by the gradients in the magnetic field and plasma density that induce strong electron drifts. The instability criteria of this linear mode matches the onset conditions of the fluctuations observed on PCX.

While the initial goal of this work was to observe the magnetorotational instability in a laboratory plasma, the rich Hall physics encountered along the way has been extremely interesting. I have outlined clear conditions where the MRI should be excited with edge-driven flow in PCX as well as volumetric flow drive in the BRB. Additionally, I have identified an interesting feature of the VFD equilibrium in the Hall regime that has strong implications for both the flow profile and the magnetic field. Finally, I have presented observations of a new electromagnetic instability in a plasma Couette flow that is driven by strong electron Hall currents, rather than ion flow. Both of the equilibrium and instability features of VFD in the Hall regime are of great importance to future experiments focused on driving fast, unmagnetized plasma flows.

6.2 Future Work

I will end this dissertation with a few suggestions for work that can expand on what I have presented here. These suggestions are not guaranteed to produce interesting results, but might provoke thought along lines that I have left unexplored.

The most straightforward suggestion is to optimize the flow drive and plasma conditions for volumetric flow drive in order to excite the MRI. For the current direction in the BRB experiments, Fig. 4.15 shows unstable regions of n-P_0 phase space that are tantalizingly close to the achieved experimental parameters. By slightly increasing the ionization fraction, the MRI could be excited by VFD in this configuration. The simplest way to do this would be to increase the injected power by adding more cathodes.

In hand with going after the MRI in the VFD configuration on BRB, it would be extremely beneficial to adjust the NIMROD simulations to correctly predict the peaked flow profile, which would likely allow simulations to drive the MRI. It would be an enormous advantage to simulate the saturated state of the MRI in this geometry to match experimental measurements. I suspect that the main culprit in this mismatch is the flow and magnetic field boundary conditions in NIMROD, which can be adjusted fairly easily.

Another fairly straightforward suggestion is to improve the sensitivity of magnetic field measurements. It is highly beneficial to understand the current paths in the VFD, but at present the Hall probe array is not sensitive enough to measure the gradient in toroidal field required to infer the radial current profile. Having a measurement of both the radial and toroidal currents in VFD equilibria would confirm the simple Hall mechanism I have outlined here and allow for refinement and deeper understanding of the cross-field current drive.

If PCX is to survive, I would also suggest that a new centerstack is designed and implemented to continue the boundary flow drive work. While VFD has shown a clear way to drive centrally peaked flows, it comes at the cost of a more complicated magnetic field and density equilibrium. Edge-driven Taylor-Couette flow is still a viable configuration for the MRI and has not been given a full effort after the magnetic confinement upgrade. It will important for a future centerstack to address the maintenance and reliability issues associated with the first iteration. Additionally, PCX is due for an in depth repair of the magnet water cooling system. I would suggest a reconfiguration of the water cooling lines that run to and from the magnet rings. Continual sealing works as a short term fix, but eventually clogs the water channel such that cooling is nearly impossible.

Finally, I believe that the reversed current VFD configuration on PCX should be applied to the BRB. Work has already begun on high-density cathode arrays that can be mounted at the poles of the BRB. The larger volume and significantly higher power injection could lead to a turbulent state if the electromagnetic gradient drift instability is driven hard enough. This turbulent, Hall dominated state would be extremely interesting to study with the full suite of diagnostics available on the BRB.

References

[1] H. Alfvén, Nature **150**, 405 (1942).

[2] E. P. Velikhov, Soviet Physics JETP **36**, 995 (1959).

[3] S. Chandrasekhar, Proceedings of the National Academy of Sciences of the United States of America **46**, 253 (1960).

[4] S. A. Balbus and J. F. Hawley, The Astrophysical Journal **376**, 214 (1991).

[5] N. I. Shakura and R. A. Sunyaev, Astronomy and Astrophysics **24**, 337 (1973).

[6] H. K. Moffatt, Nature **341**, 285 (1989).

[7] J. Larmor, Report of the 87th Meeting of the British Association for the Advancement of Science , 159 (1919).

[8] T. G. Cowling, Monthly Notices of the Royal Astronomical Society **94**, 39 (1933).

[9] E. Bullard and H. Gellman, Philosophical Transactions of the Royal Society A. **247**, 213 (1954).

[10] M. L. Dudley and R. W. James, Proceedings of the Royal Society A. **425**, 407 (1989).

[11] E. N. Parker, The Astrophysical Journal **122** (1955).

[12] A. Gailitis, O. Lielausis, S. Dementév, E. Platacis, A. Cifersons, G. Gerbeth, T. Gundrum, F. Stefani, M. Christen, H. Hänel, and G. Will, Physical Review Letters **84**, 4365 (2000).

[13] R. Stieglitz and U. Müller, Physics of Fluids **13**, 561 (2001).

[14] D. R. Sisan, N. Mujica, W. A. Tillotson, Y. M. Huang, W. Dorland, A. B. Hassam, T. M. Antonsen, and D. P. Lathrop, Physical Review Letters **93**, 8 (2004).

[15] A. H. Roach, E. J. Spence, C. Gissinger, E. M. Edlund, P. Sloboda, J. Goodman, and H. Ji, Physical Review Letters **108**, 1 (2012).

[16] F. Stefani, T. Gundrum, G. Gerbeth, G. Rüdiger, M. Schultz, J. Szklarski, and R. Hollerbach, Physical Review Letters **97**, 184502 (2006).

[17] W. Liu, J. Goodman, I. Herron, and H. Ji, Physical Review E **74**, 056302 (2006).

[18] M. D. Nornberg, E. J. Spence, R. D. Kendrick, C. M. Jacobson, and C. B. Forest, Physical Review Letters **97**, 74 (2006).

[19] R. Monchaux, M. Berhanu, S. Aumaître, A. Chiffaudel, F. Daviaud, B. Dubrulle, F. Ravelet, S. Fauve, N. Mordant, F. Pétrélis, M. Bourgoin, P. Odier, J. Pinton, N. Plihon, and R. Volk, Physics of Fluids **21** (2009), 10.1063/1.3085724.

[20] N. Z. Taylor, *Optimizing the flow in a liquid sodium dynamo experiment*, Ph.D. thesis, University of Wisconsin-Madison (2014).

[21] S. I. Braginskii, Reviews of Plasma Physics (1965).

[22] C. B. Forest, K. Flanagan, M. Brookhart, M. Clark, C. M. Cooper, V. Désangles, J. Egedal, D. Endrizzi, I. V. Khalzov, H. Li, and et al., Journal of Plasma Physics **81**, 345810501 (2015).

[23] C. Collins, N. Katz, J. Wallace, J. Jara-Almonte, I. Reese, E. Zweibel, and C. B. Forest, Physical Review Letters **108**, 115001 (2012).

[24] C. Collins, M. Clark, C. M. Cooper, K. Flanagan, I. V. Khalzov, M. D. Nornberg, B. Seidlitz, J. Wallace, and C. B. Forest, Physics of Plasmas **21**, 042117 (2014).

[25] N. Katz, C. Collins, J. Wallace, M. Clark, D. Weisberg, J. Jara-Almonte, I. Reese, C. Wahl, and C. B. Forest, Review of Scientific Instruments **83**, 063502 (2012).

[26] K. Flanagan, M. Clark, C. Collins, C. M. Cooper, I. V. Khalzov, J. Wallace, and C. B. Forest, Journal of Plasma Physics **81**, 345810401 (2015).

[27] C. Collins, *Spinning an unmagnetized plasma for magnetorotational instability studies in the Plasma Couette Experiment*, Ph.D. thesis, University of Wisconsin-Madison (2013).

[28] J. C. Simpson, J. E. Lane, C. D. Immer, and R. C. Youngquist, *Simple analytic expressions for the magnetic field of a circular current loop*, Tech. Rep. (NASA Kennedy Space Center, 2001).

[29] C. M. Cooper, J. Wallace, M. Brookhart, M. Clark, C. Collins, W. X. Ding, K. Flanagan, I. Khalzov, Y. Li, J. Milhone, M. Nornberg, P. Nonn, D. Weisberg, D. G. Whyte, E. Zweibel, and C. B. Forest, Physics of Plasmas **21**, 013505 (2014).

[30] D. B. Weisberg, E. Peterson, J. Milhone, D. Endrizzi, C. Cooper, V. Désangles, I. Khalzov, R. Siller, and C. B. Forest, Physics of Plasmas **24**, 056502 (2017).

[31] D. B. Weisberg, *Pursuing the plasma dynamo and MRI in the laboratory: Hydrodynamic studies of unmagnetized plasmas at large magnetic Reynolds number*, Ph.D. thesis, University of Wisconsin-Madison (2016).

[32] V. Désangles, J. Milhone, C. M. Cooper, D. B. Weisberg, M. D. Nornberg, and C. B. Forest, Journal of Plasma Physics **84**, 905840312 (2018).

[33] X. M. Zhu and Y. K. Pu, Journal of Physics D: Applied Physics **43**, 403001 (2010).

[34] J. B. Boffard, R. O. Jung, C. C. Lin, and A. E. Wendt, Plasma Sources Science and Technology **19**, 065001 (2010).

[35] N. Hershkowitz, in *Plasma Diagnostics*, edited by O. Auciello and D. L. Flamm (Academic Press, 1989) pp. 113 – 183.

[36] F. F. Chen (IEEE-ICOPS meeting, Jeju, Korea, 2003) mini-Course on Plasma Diagnostics.

[37] R. L. Merlino, American Journal of Physics **75**, 1078 (2007).

[38] S. L. Chen and T. Sekiguchi, Journal of Applied Physics **36**, 2363 (1965).

[39] C. Theiler, I. Furno, A. Kuenlin, P. Marmillod, and A. Fasoli, Review of Scientific Instruments **82**, 013504 (2011).

[40] E. E. Peterson, *A Laboratory Model for Magnetized Stellar Winds*, Ph.D. thesis, University of Wisconsin-Madison (2019).

[41] M. Hudis and L. M. Lidsky, Journal of Applied Physics **41**, 5011 (1970).

[42] I. H. Hutchinson, Physics of Plasmas **9**, 1832 (2002).

[43] K. S. Chung, Plasma Sources Science and Technology **21**, 063001 (2012).

[44] I. H. Hutchinson, Plasma Physics and Controlled Fusion **44**, 1953 (2002).

[45] E. Ko and N. Hershkowitz, Plasma Physics and Controlled Fusion **48**, 621 (2006).

[46] I. H. Hutchinson, Plasma Physics and Controlled Fusion **45**, 1477 (2003).

[47] J. J. Gosselin, S. C. Thakur, S. H. Sears, J. S. McKee, E. E. Scime, and G. R. Tynan, Physics of Plasmas **23**, 073519 (2016).

[48] D. L. Brower, Y. Jiang, W. X. Ding, S. D. Terry, N. E. Lanier, J. K. Anderson, C. B. Forest, and D. Holly, Review of Scientific Instruments **72**, 1077 (2001).

[49] B. H. Deng, D. L. Brower, W. X. Ding, M. D. Wyman, B. E. Chapman, and J. S. Sarff, Review of Scientific Instruments **77**, 10F108 (2006).

[50] I. H. Hutchinson, "Principles of plasma diagnostics," (Cambridge University Press, 2002) Chap. 4, pp. 95–114, 2nd ed.

[51] J. Birch, Infrared Physics **30**, 195 (1990).

[52] N. E. Lanier, J. K. Anderson, C. B. Forest, D. Holly, Y. Jiang, and D. L. Brower, Review of Scientific Instruments **70**, 718 (1999).

[53] F. Roesler, in *Astrophysics*, Methods in Experimental Physics, Vol. 12, edited by N. Carleton (Academic Press, 1974) pp. 531 – 569.

[54] M. M. Coakley and F. L. Roesler, in *Optical Spectroscopic Techniques and Instrumentation for Atmospheric and Space Research*, Vol. 2266, edited by J. Wang and P. B. Hays, International Society for Optics and Photonics (SPIE, 1994) pp. 122 – 132.

[55] M. M. Coakley, F. L. Roesler, R. J. Reynolds, and S. Nossal, Applied Optics **35**, 6479 (1996).

[56] J. Milhone, K. Flanagan, M. D. Nornberg, M. Tabbutt, and C. B. Forest, Review of Scientific Instruments **90**, 063502 (2019).

[57] F. Feroz and M. P. Hobson, Monthly Notices of the Royal Astronomical Society **384**, 449 (2008).

[58] J. Milhone, *Instability, Ion Heating, and Flow Drive in High-β Hall Plasmas*, Ph.D. thesis, University of Wisconsin-Madison (2020).

[59] R. J. Donnelly, Physics Today **44**, 32 (1991).

[60] A. Mallock, Proceedings of the Royal Society of London **45**, 126 (1889).

[61] M. Couette, Journal of Physics: Theories and Applications **9**, 414 (1890).

[62] G. I. Taylor, Philosophical Transactions of the Royal Society of London. Series A, Containing Papers of a Mathematical or Physical Character **223**, 289 (1923).

[63] S. Boldyrev, D. Huynh, and V. Pariev, Physics Review E **80**, 066310 (2009).

[64] M. D. Graham, Journal of Fluid Mechanics **360**, 341–374 (1998).

[65] R. Hegerberg, M. T. Elford, and H. R. Skullerud, Journal of Physics B: Atomic and Molecular Physics **15**, 797 (1982).

[66] H. Helm, Journal of Physics B: Atomic and Molecular Physics **10**, 3683 (1977).

[67] F. Ebrahimi, B. Lefebvre, C. B. Forest, and A. Bhattacharjee, Physics of Plasmas **18**, 062904 (2011).

[68] I. Khalzov and A. Smolyakov, Technical Physics **51**, 26 (2006).

[69] L. Rayleigh, Proceedings of the London Mathematical Society **s1-11**, 57 (1879).

[70] M. Wardle and C. Ng, Monthly Notices of the Royal Astronomical Society **303**, 239 (1999).

[71] S. Balbus and C. Terquem, The Astrophysical Journal **552**, 235 (2001).

[72] O. Blaes and S. Balbus, The Astrophysical Journal **421**, 163 (1994).

[73] E. Velikhov, A. Ivanov, S. Zakharov, V. Zakharov, A. Livadny, and K. Serebrennikov, Physics Letters A **358**, 216 (2006).

[74] I. V. Khalzov, A. I. Smolyakov, and V. I. Ilgisonis, Journal of Fluid Mechanics **644**, 257–280 (2010).

[75] N. Plihon, G. Bousselin, F. Palermo, J. Morales, W. J. T. Bos, F. Godeferd, M. Bourgoin, J.-F. Pinton, M. Moulin, and A. Aanesland, Journal of Plasma Physics **81** (2014), 10.1017/s002237781400083x.

[76] H. Ji, J. Goodman, and A. Kageyama, Monthly Notices of the Royal Astronomical Society **325**, L1 (2001).

[77] C. Sovinec, A. Glasser, T. Gianakon, D. Barnes, R. Nebel, S. Kruger, S. Plimpton, A. Tarditi, M. Chu, and the NIMROD Team, Journal of Computational Physics **195**, 355 (2004).

[78] E. Bullard, Mathematical Proceedings of the Cambridge Philosophical Society **51**, 744–760 (1955).

[79] W. Frias, A. I. Smolyakov, I. D. Kaganovich, and Y. Raitses, Physics of Plasmas **19**, 072112 (2012).

[80] C. S. Corr and R. W. Boswell, Physics of Plasmas **14**, 122503 (2007).

[81] S. Shinohara, D. Kuwahara, K. Yano, and A. Fruchtman, Physics of Plasmas **23**, 122108 (2016).

[82] A. Simon, The Physics of Fluids **6**, 382 (1963).

[83] F. C. Hoh, The Physics of Fluids **6**, 1184 (1963).

[84] Q. Frias, A. I. Smolyakov, I. D. Kaganovich, and Y. Raitses, Physics of Plasmas **20**, 052108 (2013).

[85] I. V. Khalzov, B. P. Brown, C. M. Cooper, D. B. Weisberg, and C. B. Forest, Physics of Plasmas **19**, 112106 (2012).

[86] I. V. Khalzov, C. M. Cooper, and C. B. Forest, Physical Review Letters **111**, 125001 (2013).

Appendix A:
Details of PCX Confinement Upgrade

The PCX upgrade (PCX-U) took place from Fall 2014 to Fall 2015, providing a massive upgrade to the magnetic confinement system of the device on the limited budget afforded by the end of a grant period. The result of this year of work has been an experiment capable of producing densities and temperatures in unmagnetized plasmas on par with the BRB. This allows for PCX to be a flexible testbed for larger scale BRB experiments and advanced diagnostic equipment, without the need to adapt for different plasma conditions. Throughout the design and construction, several novel approaches were made that are worth documenting for future work on PCX. This upgrade marked a major step in my graduate work and I feel it is important to emphasize some of the details that went into this project.

A.1 Design Process

The design process for this upgrade was very iterative and based a great deal on the wealth of knowledge and support given by John Wallace and Mike Clark. Several key design points were set as optimization goals for the final design: magnet material, maximum cooling, and modular construction.

First, the magnets themselves were totally replaced. On the original PCX, ceramic magnets with a relatively low field strength and heat tolerance were used. These magnets served their purpose quite well, but a stronger cusp field was desired with a higher temperature tolerance. The stronger field reduces the loss width of the cusp, improving the

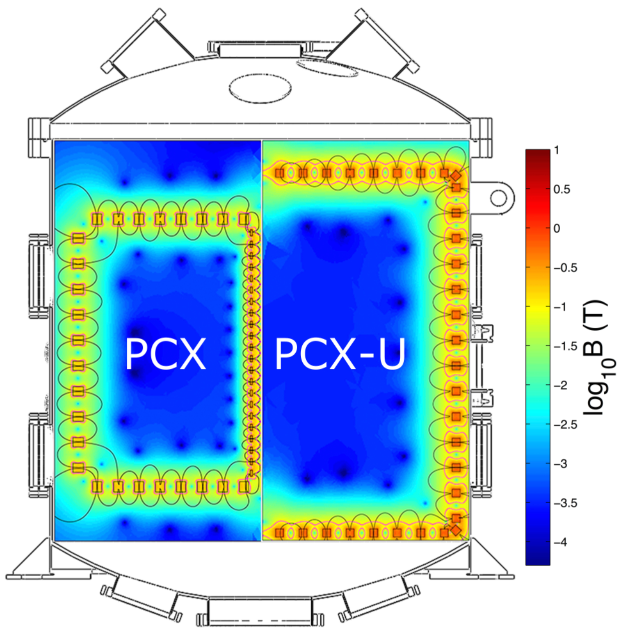

Figure A.1: Side-by-side comparison of the magnetic field strengths and plasma volume in the original version of PCX (left) and the upgrade (right). The upgraded PCX both has stronger magnets and a larger plasma volume, both acting to boost the confinement time of the system.

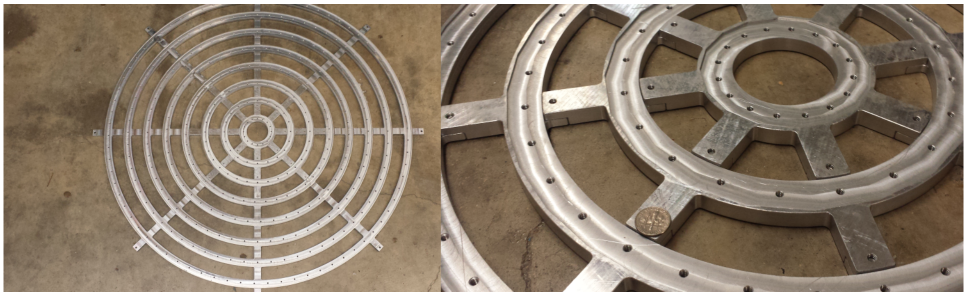

Figure A.2: Images of the 8 concentric magnet rings used as endcaps on PCX-U. The innermost three rings are separably removable, allowing fixtures up to 16” in diameter to be inserted on axis into the chamber.

confinement time of the device. This is a key feature in reaching higher densities and temperatures. In the upgrade, a set of custom made samarium cobalt (SmCo) magnets were used with an approximate surface strength of 3 kG and a maximum operating temperature of 300° C (see Ch. 2 for more details). The magnets mount via a single screw through hole, rather than epoxy as used with the older ceramic magnets. Also, their cross-sections require a faceted ring to mount them inside the diameter of the PCX vessel.

Like the previous magnetic confinement system, the magnets are water-cooled in PCX-U. This feature leads a steep increase in complexity of the design due to the restrictions of water fittings that are vacuum compatible. In order to increase the cooling via strong thermal conduction, the aluminum rings that hold the magnets in place double as cooling pipes, with two internal water channels. These channels are then connected to a pair of pipes via a welded tube and Swagelok fittings (see Fig. A.7). Instead of having connecting the cooling in series inside of the vacuum, each ring has it’s own dedicated send and return water line. These lines are fed through a top flange that doubles as the support for the entire system. In order to reduce costs, simple through hole bolts, shown in Fig. A.7, serve as o-ring seals for these water lines. By separating the rings water cooling, the cooling capacity is greatly increased, but at the cost of more vacuum feedthroughs and more in-vacuum water fittings.

The last major design point was the desire to have a modular design. This ideally allows for both easy maintenance as well as flexibility for various configurations. The entire magnet assembly is supported by a top flange that doubles as the location of the water cooling feedthroughs. In theory this allows for easy installation and removal of the system from the chamber. In addition to the rings along the sides of the vessel, a set of 8 concentric rings are placed at the top and bottom to serve as endcaps, seen in Fig. A.2. The three innermost of these rings can be removed to accommodate fixtures as large as 16" in diameter to be inserted on axis in PCX-U. A primary consideration behind this was the possibility of a more-robust and larger diameter center-stack for inner boundary stirring.

Once the design was set, the various custom components were ordered. The magnets were supplied by Risheng Magnet International Co., which had provided the custom SmCo magnets used in the BRB as well. The alumina tiles used to insulate the magnets were likewise purchased from a previous BRB vendor, Pingxiang Zhongying Packing Co. The extruded aluminum rings were manufactured and bent by ShenZhen XieLeFeng Metal & Plastic Products Co. The custom milled top flange was machined by Squires Machine Service based in Clinton, WI. Finally, the set of concentric end cap rings were manufactured by the UW Physics Department Instrument Shop. A large number of these components were manufactured in China due to the willingness to produce small-batch custom pieces and the expertise in rare earth magnets. This proved to be an excellent choice for cost-effectiveness and rapid production, but some post-production alternations were necessary.

A.2 Construction

The key component of this system, the magnets, were produced with a specified range of allowable strengths. While this range was quite narrow, an easy way to improve the symmetry of the magnet rings is to bin them by strength. Led by Yufan Xu, a group of dedicated undergraduate researchers used a 3-axis Hall sensor to measure and group every one of the nearly 3000 magnets used in this assembly. As a result, each individual ring's set of magnets have been chosen to maximize uniformity, ensuring great symmetry of the magnetic field.

The next major component of the system, the extruded aluminum rings, proved to be rather tedious to manipulate into their final designed form. The rings were extruded to a given length and then bent into a specified diameter by the manufacturer, with the rest of the machining to be left to the Physics Instrument Shop. Unfortunately the rings were warped out of plane by the bending process by an amount that would be unacceptable for both the machining process and for the final product. The solution was to take advantage of the relatively low deflection temperature of aluminum to force the rings into a single plane. This defect and the process of flattening is shown in Fig. A.3. Each ring was wrapped with resistive heat tape and compressed with more than 2 tons of weights. This process effectively flattened the rings, but removed the temper of the aluminum, making it much more difficult to machine.

In conjunction with Doug Dummer and Bill Foster in the Instrument Shop, John Wallace designed a custom fixture plate (see Fig A.4) for the rings that would hold them in a flat plane at a known reference for the CNC machining process that created the facets required for holding the magnets. It was necessary to very carefully index this fixture because the distance between the internal water cooling channels and the final machined facet was quite small. After the CNC machining, both the water cooling tubes and a small bridge over the necessary gap had to be welded to the aluminum. Again, this was difficult due to the tight tolerances of the water channels as well as the lack of temper in the aluminum after the flattening process.

The final machining of the rings was the very careful drilling and taping of the individual mounting holes for each magnet. This arduous process was facilitated by yet another custom fixture designed to hold the rings in a drill press and drill to a very exact depth (again to avoid the internal water cooling channels). The tapping process was also difficult due to the "gumminess" of the aluminum after the flattening process. Again, a

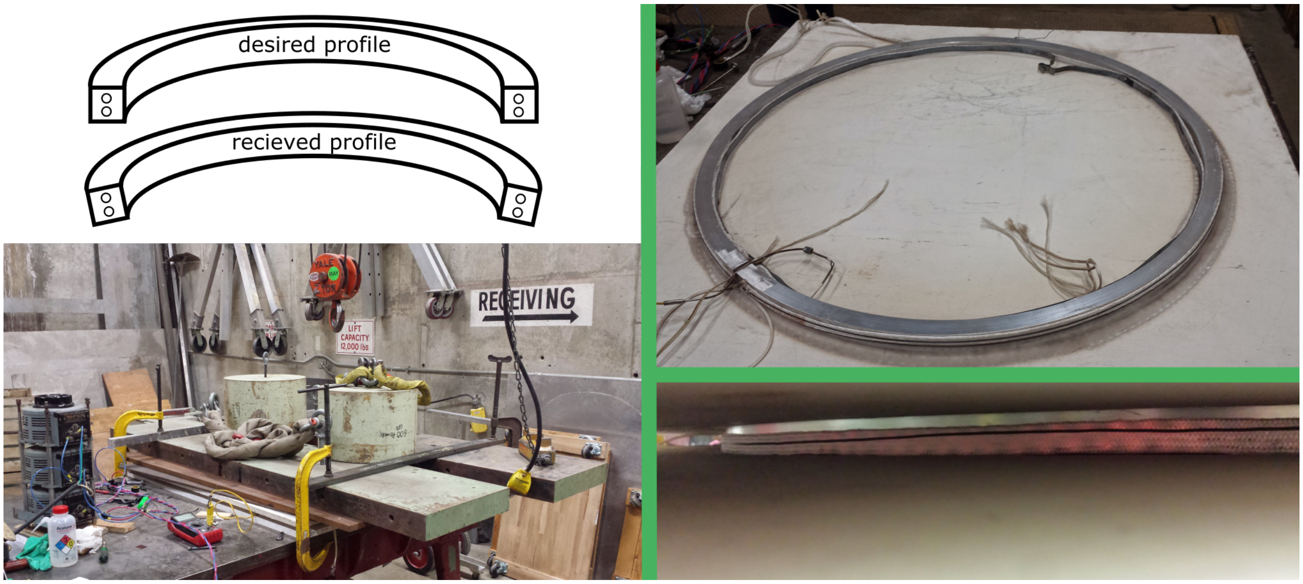

Figure A.3: Top Let: a cartoon of the desired profile of the rings and the received profile showing the out-of-plane warping that was a result of the bending. Top Right the ring wrapped with ~ 1 kW of heat tape. Bottom right: the rings were heated to roughly 200° F. Bottom left: The 2+ tons of weights used to flatten the heated rings.

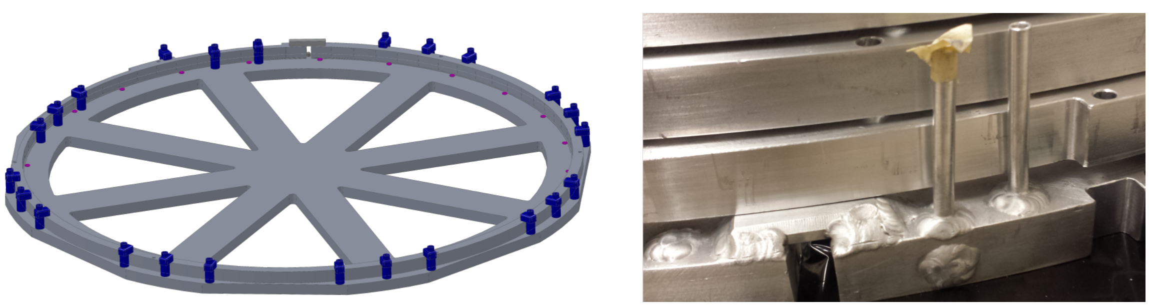

Figure A.4: Left: a CAD drawing of the fixture plate used for machining the rings using a CNC mill. Right: a closeup of the welds used to make water connections and mechanically hold the small gap in the rings.

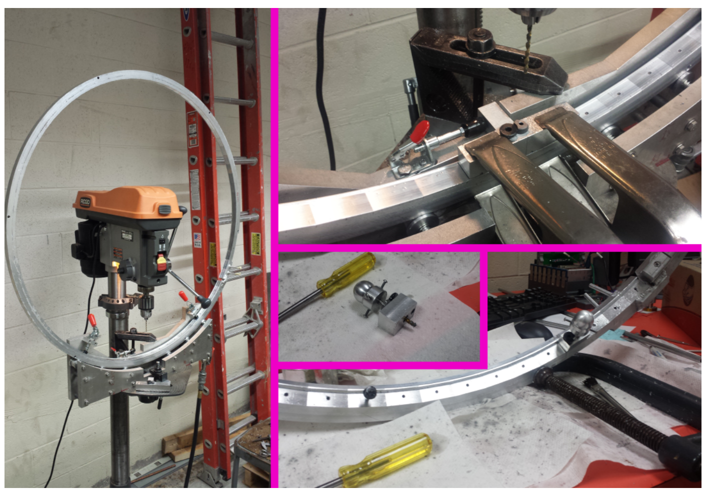

Figure A.5: Left: Drill press and custom made cradle for holding the rings. Top Right: closeup of drill guide used to set exact hole depth. Bottom Right: Hand tapping process using a simple tap tool with guide made to center on magnet flat (center).

dedicated group of undergraduate researchers greatly expedited this process as well as a large supply of taps.

After all the constitute pieces were assembled and, in the case of the magnets, sorted. It was necessary to clean them to avoid unnecessary complications when they were brought under vacuum. The normal procedure for high-vacuum environments is to use ultrasonic baths to clean components. This was possible for the magnets and smaller hardware, however the rings and large top flange required a custom setup. A small plastic pool was filled with 20+ gallons of ethanol and then a series of ultrasonic tranducers were submerged and arranged at fixed locations throughout the bath. The ring to be cleaned was then supported by an axis driven by a geared motor to slowly spin in the ethanol solution. This spinning allowed the fixed location ultrasonic transducers to cover the entire ring over the course of many rotations. While fairly slow, this process was absolutely necessary given the many different manufacturing steps that these rings had been through.

The system was assembled on a stand outside of the chamber and, when complete, an attempt was made to lower into the vessel via the lab's hoist (see Fig. A.6). Due to the extremely tight tolerance of the ring diameter relative to the vessel, the system required force to fully insert into the chamber. Near the end of this process, it was discovered that a large weld bead on the inside of the chamber was preventing the final ring from reaching it's designated position. The assembly was removed and a spacer ring between the top support flange and the chamber was quickly produced to raise the magnet assembly by one ring spacing. This allowed the magnets to be held above the weld bead inside the chamber and proved to a simple fix to this final hurdle.

A.3 Water Sealing

While the PCX upgrade has been a resounding success that allows for improved confinement and plasma performance, the water cooling system has proven to be a constant source of problems. Here I will outline the main issues, the steps we have taken to address them and possible long term solutions.

Figure A.6: The PCX magnet assembly being directed via the lab hoist over the chamber. Left to right: Ken Flanagan and Mike Clark

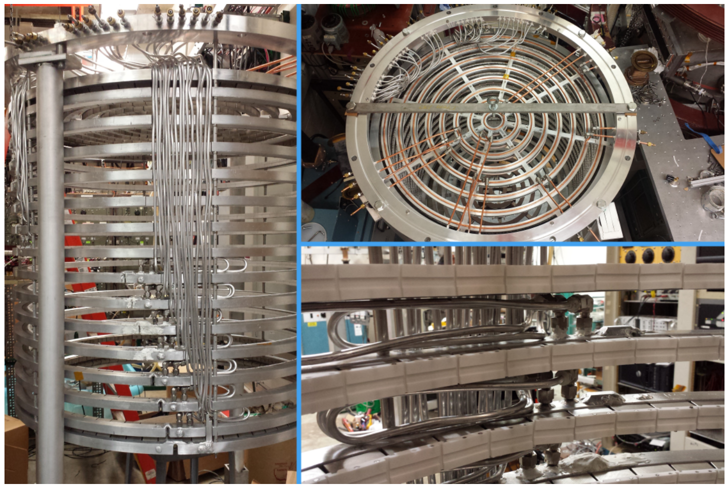

Figure A.7: Left: the outside of the magnet cage showing the routing of the water cooling tubes to each ring. Top Right: A top down view of the endcap water cooling and the water connections made through the top support flange. Bottom Right: close up of the Swagelok fittings used to connect the water tubes to each ring.

After welding the small tubes to the ring water cooling channels and drilling and tapping all of the magnet mounting holes, each ring needed to be vacuum tested to ensure no leaks had been created. A helium leak checking system revealed that many of the rings had small leaks near the welded tubes and the small gap that was bridged with a weld. Rather than attempt to repair these welds and risk further leaking, a vacuum epoxy, Torr-Seal, was used to seal any leaks. Each ring was then checked, sealed where necessary and rechecked to ensure a good seal.

A major part of the system assembly outside of the chamber was the routing of the many water cooling tubes from each ring up to the top support flange with feedthroughs (see Fig. A.7). An extremely flexible semi-rigid aluminum tubing was used along with simple Swagelok fittings. The small spacing between the rings required tighter-than-suggested bends in the tube and difficult-to-reach locations for the fittings. As expected (and feared), leak testing at this stage also revealed small leaks, either in the fittings or the already sealed rings. In the case of previous seals, the vacuum epoxy is known the very brittle when fully dried, so any mechanical stress could have introduced small leaks. These leaks were carefully identified and sealed.

As noted above, the installation process was rather difficult and required quite a bit of force, therefore it was mostly expected to find leaks in the water cooling yet again. Sealing these leaks required a different approach because access to the leaky locations was very restricted once the system was installed in the chamber. With the help of Mike Clark, a internal sealing solution was found that seals leaks from the inside of the water cooling channel. This solution, 95-1000AA from Godfrey & Wing, requires a thermal curing process to fully set, but is very inviscid, so it is capable of filling tiny leaks that can cause problems at ultra-high vacuum pressures.

Water leaks are fairly easy to identify using the RGA to monitor partial vacuum pressures. Characteristically, these leaks will reduce slightly when the water cooling pump is shut off. To identify a specific ring, each circuit is compressed with nitrogen and the RGA is consulted. Once a specific ring is identified, it is usually pre-heated with hot air and then filled with sealant, pressured, cleared and heated again. This process takes anywhere from 30 minutes to 2 hours depending on the number of iterations required for each leaky ring. Usually, the RGA will clearly indicate that the ring has been sealed and it can be refilled with water. Once sealed, rings can continue to operate for many months without further problems. However, the sealant does seem to erode somewhat and certain rings are frequent suspects whenever a leak is identified. As such, the ring sealing process has become a regular maintenance task of PCX-U to ensure the excellent base pressure of roughly 10^{-7} torr.

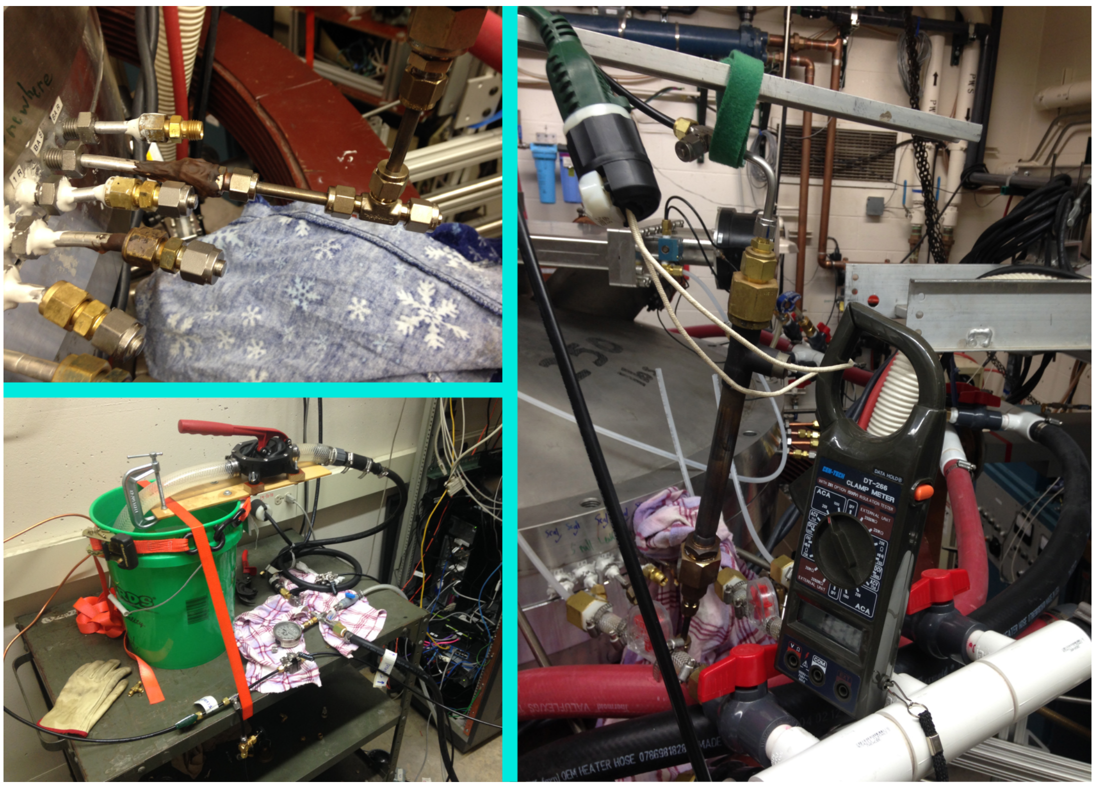

Figure A.8: Top Left: The water connections just outside of the top flange shown with extra vacuum epoxy. Bottom Left: the apparatus used to pump the thermal sealant into the rings. Right: the heater used for preheating and then curing.

Appendix B:
von Kármán NIMROD Simulations

This appendix explores the NIMROD simulation results for a configuration similar to volumetric flow drive described throughout this work that leads to a dynamo like instability. The flow driven in this configuration is similar to von Kármán, with counter-rotating hemispheres. The resulting dynamo action does not include a feedback mechanism in the simulation, but does match with models of slow dynamos driven by t2s2 flow described by Dudley & James [10]. An experimental attempt was made to drive this flow on the BRB, but did not result in any flowing equilibria.

B.1 Description of Setup

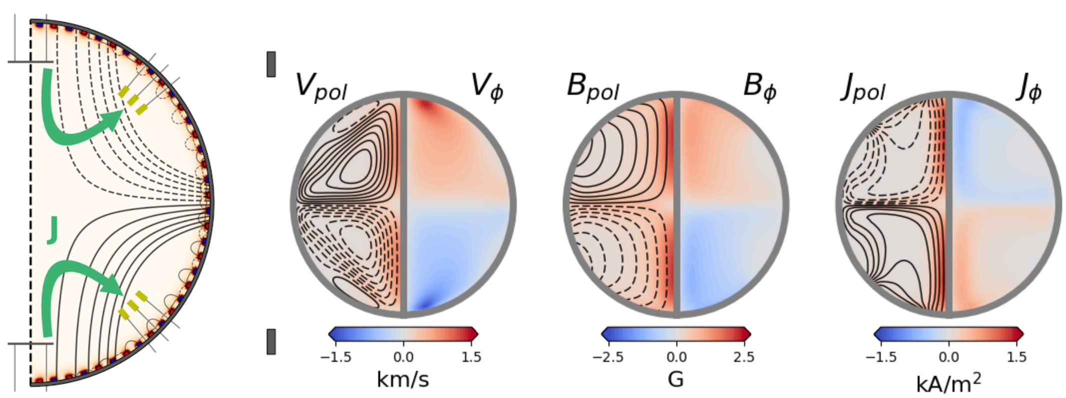

Figure B.1: Left: Simple schematic of the von Kármán configuration of volumetric flow drive. A weak quadrupole field is applied with a Helmholtz coil set and currents are driven from polar anodes to cathodes at mid-latitudes. Right: NIMROD velocity, magnetic field and current for the $m = 0$ stable equilibrium for 600 A total injected current.

Similar to VFD, the configuration used here relies on cross-field currents to drive toroidal flow. Instead of a uniform applied field, a quadrupole field driven by the external Helmholtz coils is used. The cathodes are also re-positioned from the equatorial region to mid-latitudes so as to drive opposite flows in the different hemispheres. A simple diagram of this setup is shown in Fig. B.1.

The mesh and current injection mechanism used in these NIMROD simulations are identical to those presented in Chapter 4. The only differences are the initial field which is no longer specified as a uniform value, but calculated from currents driven in the Helmholtz coils, and the location of the current injection regions.

For simulation runs that include many toroidal mode numbers, the High Performance Computing (HPC) cluster at the Center for High Throughput Computing (CHTC) at UW-Madison was used. The HPC cluster allows for users to claim hundreds of processor cores for queued jobs. For this analysis most energy seemed to be concentrated in $0 \leq m \leq 5$ azimuthal harmonics, so most simulations used between 50 and 200 cores. While this exploration was not exhaustive, a good survey was achieved by comparing the MHD and Hall Ohm's law cases as well as checking for good convergence by using a higher density mesh.

B.2 Possible Dynamo Action

For cases with only the resistive MHD Ohm's law used, a steady-state $m = 1$ magnetic field feature is observed when a critical R_m is reached. This feature, shown in Fig B.2, is consistent with the transverse dipole predicted by the simple laminar dynamo produced by t2s2 flow, similar to what has been predicted for edge-driven flow dynamos on the BRB [85].

When the two-fluid terms are included in Ohm's law, a similar magnetic field feature arises that oscillates at roughly the ion gyrofrequency for the initial field. The onset of this mode occurs at a much lower R_m as well, which has been achieved with edge driven flows

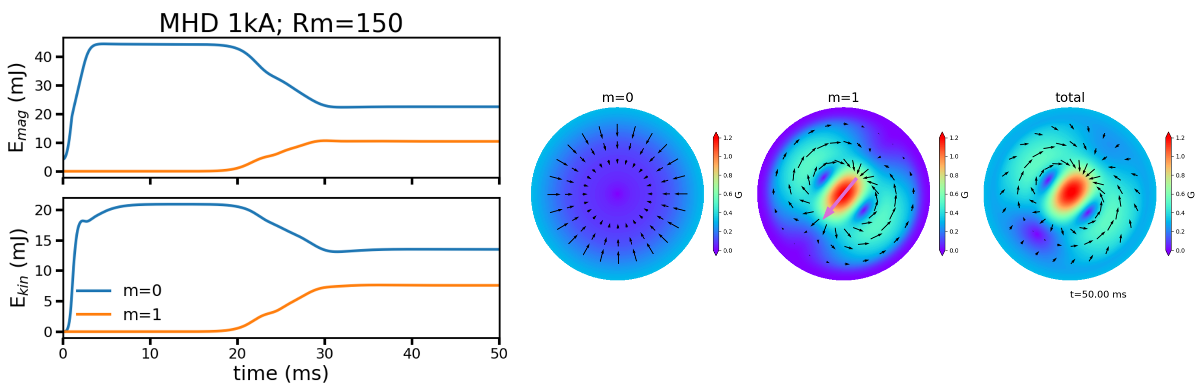

Figure B.2: Left: Magnetic (top) and Kinetic (bottom) energy of the $m = 0$ and $m = 1$ modes as a function of time for this simulation. Right: an equatorial cut of the $r - \phi$ plane showing the mode structure of the magnetic field.

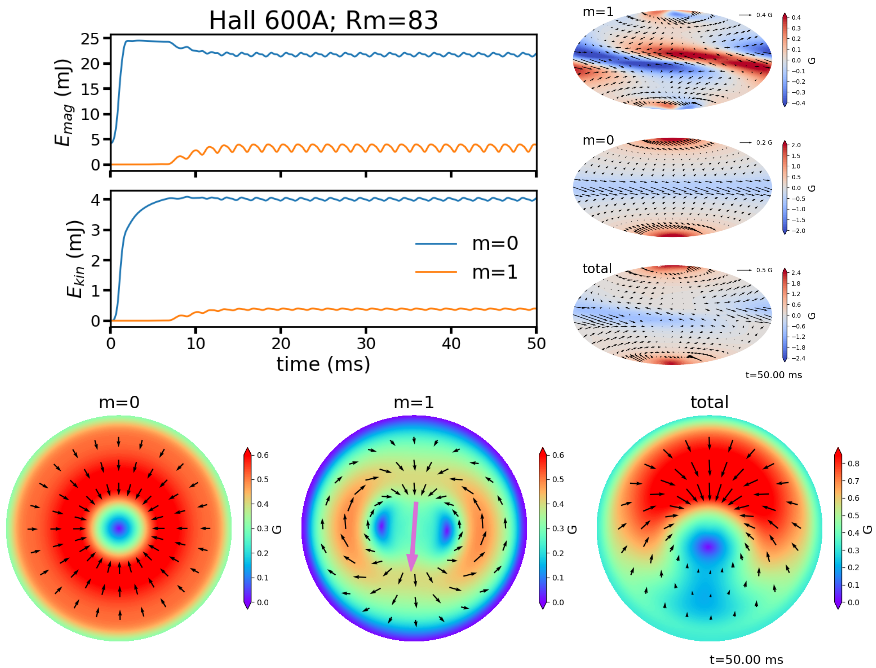

Figure B.3: Top Left: Magnetic and Kinetic energy versus time showing a 600 Hz oscillation which roughly corresponds to the ion gyrofrequency of the initial field strength. Top Right: Mode structure of the magnetic field taken at the $R = 1$ spherical surface. Bottom: Mode structure of the magnetic field in the $r - \phi$ plane at the equator.

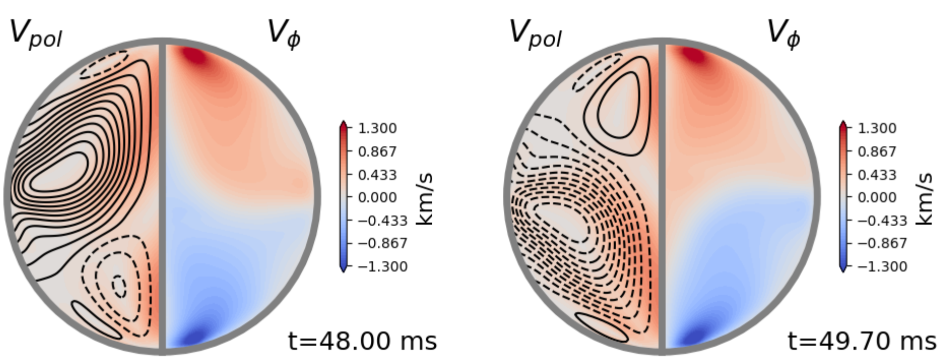

Figure B.4: Snapshots of flow in a poloidal plane perpendicular to the transverse dipole from the Hall dynamo simulation. The poloidal cells oscillate away from equilibrium with the magnetic mode oscillations.

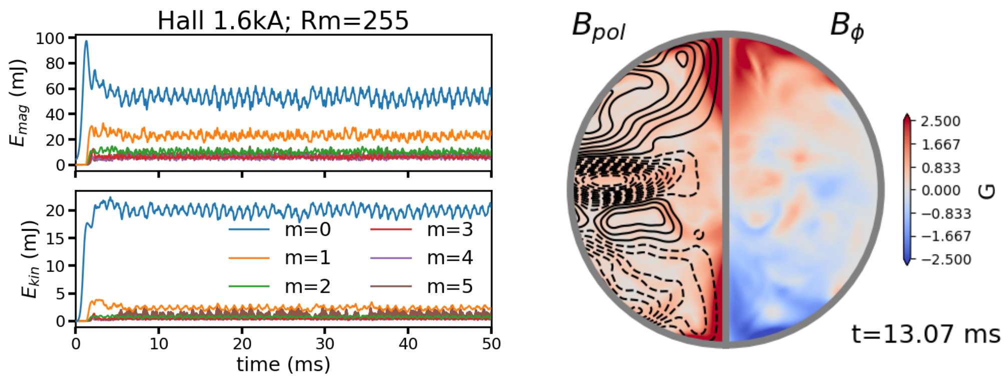

Figure B.5: Left: time evolution of the magnetic and kinetic energies show energy primarily in the $m = 0$ and $m = 1$ toroidal modes. Right: Snapshot of the magnetic field shows turbulent behavior.

in the BRB. The AC dynamo action is also accompanied by a 'sloshing' of the poloidal flow cells, shown in Fig. B.4.

Interestingly, this 'sloshing' motion is similar to flows that have been considered to drive the fast dynamo in the BRB [86]. Increasing the injected current (therefore the R_m) pushes the steady AC dynamo action into a turbulent regime where many modes are excited and the fluctuations are less regular (shown in Fig. B.5). In order to drive this turbulent action nearly 1.6 kA of injected current is required.

In all of these cases, NIMROD was run with a conducting wall boundary condition, which necessarily conserves magnetic flux. By definition, this does not allow a true dynamo action to occur because the magnetic field cannot grow, similar to the field amplification seen in the VFD simulations from Chapter 4. Additionally, this dynamo-like action is indirectly driven by the injected current, which, in the real experiment, can inject toroidal flux.

B.3 Future Directions

Despite the low critical R_m value for the oscillating dynamo behavior observed in the Hall simulations, attempts to experimentally create this scenario have failed. A scan of applied field strengths and current injection voltage bias led to no combinations that drove flow. The most likely cause is a current path that avoided crossing the applied field. For the weak fields used, the Hall probe array is not sensitive enough to easily map their structure. This means that the axial symmetry of the quadrupole field is reliant on the symmetry of the Helmholtz coil set, which is not perfect, and can lead to currents crossing the central null.

The dynamo behavior seen in NIMROD is nonetheless very interesting and occurs at reasonable experimental parameters. Future experimental efforts should be equipped with high-sensitivity magnetic diagnostics to map the current paths and adjust the applied field to ensure $\mathbf{J} \times \mathbf{B}$ flow drive. Additionally, experiments could be very beneficial for exploring the inconsistency's seen in the predicted flow in NIMROD and those experimentally achieved in the VFD configuration.